In vitro and in vivo investigation of dendronized streptavidin and fluorescent nanodiamonds, two flexible nanosystems efficiently crossing the blood-brain barrier to improve nanotheranostics in neurological disease treatment

Dissertation

Zur Erlangung des Grades

Doktor der Naturwissenschaften

am Fachbereich Biologie

Der Johannes Gutenberg-Universität Mainz

Pierpaolo Moscariello

geb. am 22.03.1989 in Salerno, Italien

Mainz, 2018

*“**Great things** are not done by impulse, but by **a series of small things brought together**;*

*and **great things** are not something accidental, but **must certainly be willed**.”*

Vincent Van Gogh

Abstract

In treatment of central nervous system (CNS) diseases, the blood-brain barrier (BBB) is the main obstacle preventing drug molecule penetration from the bloodstream into the brain. In this thesis dendronized streptavidin (DSA) and fluorescent nanodiamonds (fNDs) encapsulated by a human serum albumin (HSA)-based biopolymer (dcHSA-fNDs) are presented as promising platforms for treatment of neurological disorders via crossing an intact BBB. DSA provides a flexible bio-click system composed of an adapter of tetrameric streptavidin linked to biotinylated PAMAM dendrimers, holding the potential to apply synergistically intrinsic therapeutic function of PAMAM dendrimers combined with any biotinylated drug activity on one platform. dcHSA-fNDs represent a very peculiar nanotheranostics tool characterized by the unique optical and magnetic properties of fNDs. Moreover, the HSA-based coating provides colloidal stability and improved functionalization capability. Thus, dcHSA-fNDs exhibit the potential of real time monitoring of drug delivery.

In this thesis it is successfully demonstrated that both nanocompounds (1) are able to penetrate neurovascular unit (NVU) cells as shown by confocal imaging, immunocytochemical and biochemical analysis; (2) are transported from one side to the other of in vitro BBB models employing porcine and murine mono-cultures or murine triple co-cultures and, (3) the transport occurs via intracellular trafficking without induction of autophagy demonstrated by confocal analysis of colocalization with specific intracellular markers; (4) do not affect NVU cells viability and BBB integrity according to transendothelial electrical resistance monitoring, (5) are able to reach the brain and target NVU cells in vivo after intravenous injection as observable from screening of brain slices combined with immunohistochemistry. Specifically, DSA undergo lysosomal escape preserving cargo-carrier intracellular integrity and do not induce BBB disruption also in vivo validated by Evans Blue assay; dcHSA-fNDs show direct cell-cell migration in NVU cells moving along tunneling nanotubes; the mechanism occurs also among different cell types as observable combining live cell imaging and immunocytochemical analysis. For fNDs, this doctoral thesis provides for the first time reliable data on in vivo brain delivery and mechanisms of transport across the BBB.

In summary, in this thesis two nanoplatforms targeting the brain using highly biocompatible non-invasive strategies to develop various therapeutic approaches are investigated in detail.

Abbreviations

AD	Alzheimer disease
BAF	Bafilomycin A1
BBB	Blood-Brain Barrier
bEnd.3	Murine brain endothelial cell lines
cAMP	Cyclic adenosine monophosphate
CcL	Capacitance of the cell layer
CD105	Endoglin
CED	Convection enhanced diffusion
CNS	Central nervous system
CS	Coverslips
CTR	Control
CTX	Subunit B of cholera toxin
DALYs	Disability-adjusted life years
DAPI	4',6-diamidino-2-phenylindole
dcHSA-fNDs	Fluorescent nanodiamonds encapsulated by human serum albumin-based biopolymer
DIV	Day in vitro
DMEM	Dulbecco´s modified Eagle medium
DSA	Dendronized streptavidin
EB	Evans blue
EBM-2	Endothelial growth basal medium
ECIS	Electrical cell impedance sensing
EDTA	Ethylenediaminetetraacetic acid
EE	Early endosomes
EEA	Early endosome antigen
FCS	Fetal calf serum
FD4	FITC-Dextran 4
fNDs	Fluorescent nanodiamonds
FUS	Focused ultrasound
GFAP	Glial fibrillary acidic protein
HBSS	Hank´s balanced salt solution
HD	Huntington disease
HEPES	4-(2-hydroxyethyl)-1-piperazineethanesulfonic Acid
HS	Horse serum
HSA	Human serum albumin
ICV	Intracerebroventricular infusion
LAMP-1	Lysosomal-associated membrane protein 1
LC3	Microtubule-associated protein 1A/1B-light chain 3

LE	Late endosomes
MEM	Minimum essential medium
NDs	Nanodiamonds
NeuN	Neuronal nuclear antigen
NPs	Nanoparticles
NV	Nitrogen vacancy
NVU	Neurovascular unit
PAMAM	Poly-amidoamine
Papp	Apparent permeability
PBECs	Porcine brain endothelial cells
PBS	Phosphate buffered saline
pCPT-cAMP	8-(4-Chlorophenylthio)adenosine 3′,5′-cyclic monophosphate sodium salt
PD	Parkinson´s disease
PVDF	Polyvinylidene fluoride
SA	Streptavidin
SDS	Sodium dodecyl sulfate
TBI	Traumatic brain injury
TEER	Transendothelial electrical resistance
TF	Transferrin
TfR	Transferrin-receptor
TJs	Tight junctions
TNTs	Tunneling nanotubes
TUNEL	Terminal deoxynucleotidyl transferase (TdT)-mediated dUTP nick end labeling
VAMP3	Vesicle-associated membrane protein 3
v-SNARE	Vesicle soluble N-ethylmaleimide-sensitive-factor attachment receptor
WHO	World health organization
ZO1	Zona occludens 1

Table of contents

1. Introduction

1.1 Neurological diseases: a challenge for public health.

In the 2006 the World Health Organization (WHO) signed a document presenting in deep details the Global Burden of Disease for neurological disorders from the projected estimates for 2005, 2015 and 2030 (WHO 2006). The emerging scenario showed a dramatic situation with a final clear message: "unless immediate action is taken globally, the neurological burden is expected to become an even more serious and unmanageable threat to public health". Neurological disorders are estimated to affect as many as a billion people worldwide, no population group is immune, and the annual economic cost amounted to € 139 billion in 2004, only partially including direct non-medical costs, indirect costs and omitted intangible costs. In addition, the stigma often associated to neurological disorders is reflected in a strong self-destructive behavior to refuse treatments, hoping to avoid the negative social consequences of diagnosis and leading to social exclusion and discrimination. As shown in Figure 1, neurological disorders constituted 6.3 % of the global burden of disease (expressed in disability-adjusted life years (DALYs) as measurement of the total number of years lost because of death or disabilities), that, if compared to the data for HIV/AIDS and malignant neoplasm (slightly over 5% each), highlight their high impact on public health. Therefore, due to the social and economic relevance of neurological diseases, the WHO´s report evidences the need of immediate and effective therapeutic treatments.

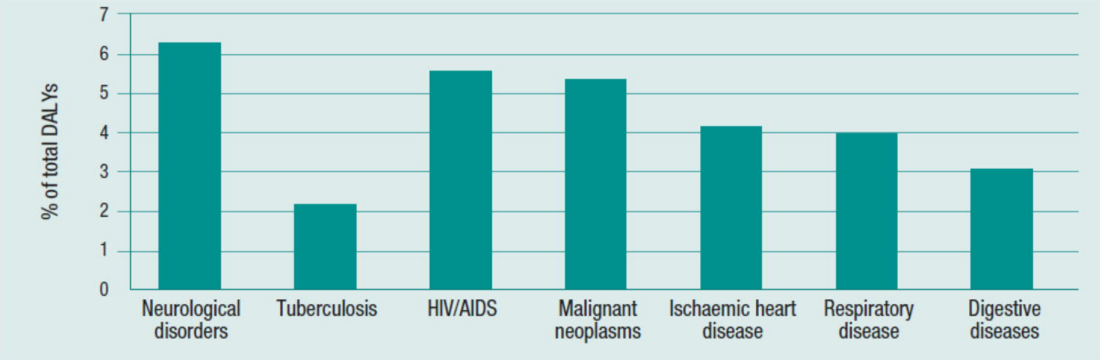

Figure 1. Percentage of total DALYs (total number of healthy-life years lost because of death or disabilities) for selected diseases and neurological disorders. The data in the graph represent the DALYs as measurement of the gap between current health status and an ideal health situation where the entire population lives to an advanced age, free of disease and disability. (modified from WHO, 2006)

On the basis of this described global situation, the work of many researchers has been focused on the identification of the underlying mechanisms of central nervous system (CNS) pathophysiology. Therefore, during the past years, the scientific community has made big progresses to improve the knowledge on neurological disorders.

Among the many findings, some of the most important ones are as follows:

- Protein misfolding and following self-association and deposition of aggregated proteins is observable in brain tissues of patients with neurodegenerative disorders. For example, the aggregation of protein tau (a microtubule-associated protein), of a 42-amino-acid form of β-amyloid or of α-synuclein leads to the formation of neurofibrillary tangles or Lewie´s bodies that characterize Alzheimer´s disease (AD), Huntington´s disease (HD), Parkinson´s disease (PD) and other neurological disorders (LaFerla, Green and Oddo 2007, Reiman 2016, Goedert 2001, Peelaerts and Baekelandt 2016).
- Immune activation and neuroinflammation represent a common link between neurological diseases. Such activation can trigger neurotoxic responses leading to progressive degeneration contributing to tissue damage. However, these mechanisms also play important role in resolving inflammation and mediating neuroprotection and repair (Amor et al. 2010, Fakhoury 2015).
- Mitochondrial dysfunction and oxidative stress are also important contributors to the pathophysiology associated to most of the neurological disorders. In fact, neuronal tissue is extremely sensitive to reactive oxygen species. Imbalance in pro-oxidant versus anti-oxidant homeostasis in CNS shows a strong toxicity, as found in AD, PD, HD and amyotrophic lateral sclerosis (Burté et al. 2015, Cherra and Chu 2008).
- Genetic mutations also trigger the onset of neurological diseases. For example, protein aggregation associated to several neurodegenerative disorders is often related to mutations in the gene encoding for that protein. Additionally, in the last years, some studies showed that de novo mutations in genes regulating autophagy cause static encephalopathy of childhood with neurodegeneration in adulthood. Some other findings also suggest that somatic, perhaps brain-only, mosaic

mutations may be important for other neurodevelopmental diseases (Poduri et al. 2013, Simonato et al. 2013).

The just described mechanisms are some of the much knowledge achieved in neurological disease research. Thus, all these scientific achievements are constantly providing possible therapeutic targets (Giacomelli, Daniele and Martini 2017, Colangelo, Alberghina and Papa 2014, Simonato et al. 2013, Harris and Rubinsztein 2011). Unfortunately, adequate treatments for neurological disorders are still an unmet medical need, not only because of lack of possible drugs, but also because systemically administered therapeutics are often ineffective due to a well know biological obstacle: the blood-brain barrier (BBB).

1.2 The BBB: a challenge for neurological disease treatments

According to the actual knowledge, the BBB exists primarily as a selective diffusion barrier at the level of the cerebral microvascular endothelium, characterized by the presence of tight cell-cell junctions and a lack of fenestrations. The first interface from bloodstream is the cell monolayer of brain capillary endothelial cells, which are in direct contact with pericytes and a conjoint basal lamina. Astrocyte endfeets cover the capillary surface and represent the connection to neurons (Daneman and Prat 2015, Ballabh, Braun and Nedergaard 2004). In summary the BBB consists of brain capillary endothelial cells, pericytes, astrocytes and neurons all referred to as the neurovascular unit (NVU) (Hawkins and Davis 2005) (Figure 2).

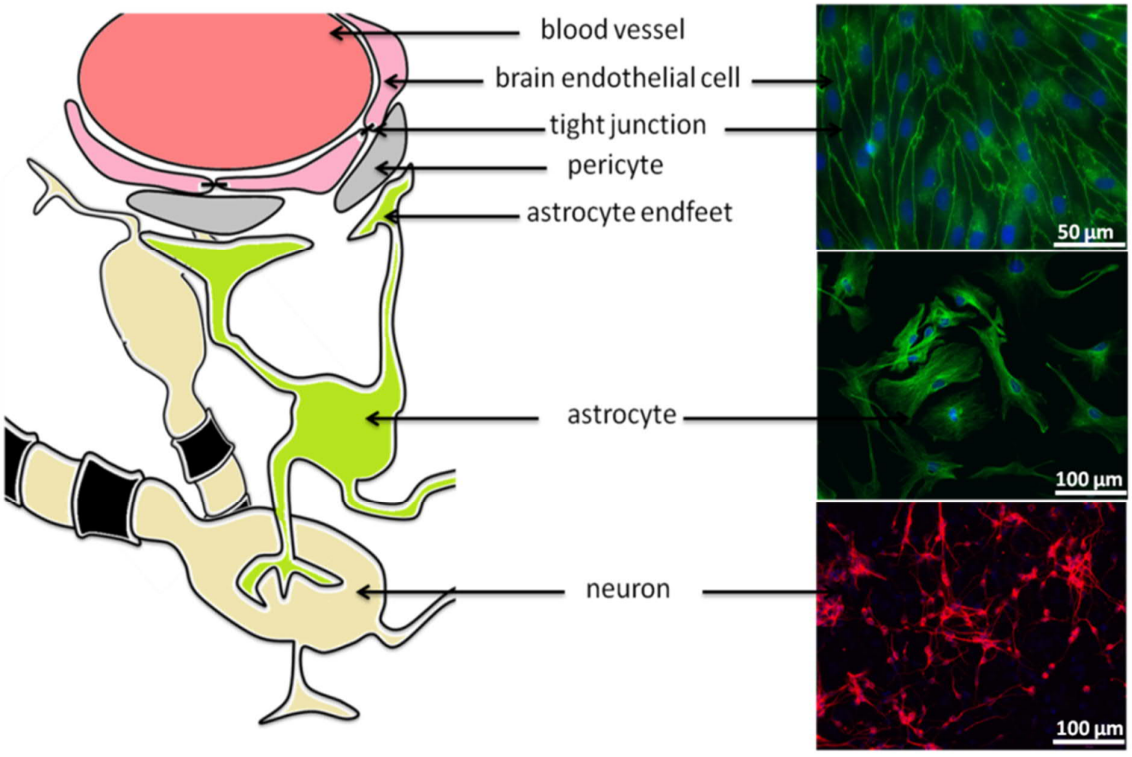

Figure 2. Components of the blood-brain barrier. Schematic representation of BBB with immunocytochemistry staining of the main cell types involved (brain endothelial cells stained with zona occludens-1, astrocytes stained with glial fibrillary acidic protein and neurons stained with β-III-tubulin).

Anatomically, the difference between endothelial cells of the BBB and those in the periphery lies in increased mitochondrial content, lack of fenestrations, minimal pinocytotic activity, and presence of tight junctions (TJ). It is the presence of TJ that confers low paracellular permeability and high electrical resistance. TJ functions as a "zipper" that affects separation of the apical and basolateral cell membranes, enabling asymmetric distribution of membrane constituents (Engelhardt, Patkar and Ogunshola 2014).

About pericytes at the actual state of art their contribution at BBB site is less characterized compared to astrocytes. However, they are involved in the regulation of the blood flow and to stabilize the formation of capillary-like structures as observed in co-culture experiments (Ballabh et al. 2004, Engelhardt et al. 2014). Indeed, in some pathological conditions such as traumatic brain injury (TBI), they migrate away from the capillary (Dore-Duffy et al. 2000). This observation shows a possible relation between lost of pericytes at the BBB site and increase of BBB permeability, typical benchmark of a pathological condition.

Astrocytes are a critical cell type in the development and maintenance of BBB secreting important molecules involved in the regulation of interactions between BBB components, production of antioxidative agents, growth factors and neurotrophins important for brain cell survival during neurodegenerative processes. Additionally, they represent the important intermediates between blood and neurons regulating the neuronal trophic support (Abbott 2014, Engelhardt et al. 2014, Ballabh et al. 2004).

Whether neurons are critical in the development of BBB function has not yet been clearly demonstrated, but it is apparent that, as feedback response, they can regulate some aspect of BBB function. For example, it has been observed in AD a significant loss of cholinergic innervation of cortical microvessels, which may lead to impaired cerebrovascular function (Hawkins and Davis 2005).

All these cell types participate together to the proper function of the BBB. Indeed, the BBB is a multicellular interface separating bloodstream and brain parenchyma, fulfilling the important task of maintaining the sensitive homeostasis of the neuronal network. For optimal activity, the CNS needs a perfectly regulated environment with characteristics far different from those in the rest of the organism. The BBB isolates the brain and the spinal cord from fluctuations in nutrients, hormones, metabolites and other blood constituents. It also protects this tissue from the influence of endo- and exogenous compounds circulating in the blood. Neuronal transmission is secured from the highly precise control of the microenvironment regulated by the BBB. Additionally, the BBB participates to the protection from abrupt changes in blood biochemistry after meals, physical exercises or pathological conditions. It is also responsible of the constitutions of two well divided neurotransmitters pools: the one of the central system and the one of the peripheral system (Bernacki et al. 2008).

Taken together, all these information provide an overview of the fundamental and remarkable role of the BBB. Unfortunately, the BBB remains also a great challenge to struggle with for scientists who work on neurological disease treatments. It represents, in fact, a “guardian” that regulates access of drugs to the CNS under both physiological and pathological circumstances.

After intravenous injection, only some lipophilic molecules can reach the brain parenchyma in concentrations that are high enough to induce a therapeutic effect, and 98 % of neuroactive

drugs, like all the products of biotechnology (e.g., monoclonal antibodies, recombinant proteins or gene therapeutics) cannot cross the BBB (Pardridge 2007). Many of the neurological disorders could be treated with drugs, enzymes or genes already discovered. However, these molecules cannot enter into brain drug development because no BBB solutions have been found by industry (Pardridge 2005).

1.2.1 Current state of research: strategies to cross the BBB and their limits

Currently, therapeutics can be delivered to the CNS via several ways. Either the drug can circumvent the BBB after systemic administration or it has to be applied by invasive methods. Possible approaches are, for example:

- Transcranial brain drug delivery using three neurosurgical-based delivery ways: intracerebral implantation, intracerebroventricular infusion (ICV), convection enhanced diffusion (CED). The limiting step for intracerebral and ICV relies on the diffusion of a drug from the application site into brain tissue. Thus, we have to consider that the concentration of a small molecule is decreased by 90 % at a distance of only 0.5 mm from the intracerebral implantation site in rat brain. This explains the inefficacy of these methods. Instead, CED consists of fluid convection within the brain, established by maintaining a pressure gradient during interstitial infusion. However, it is important to sign out that the brain is not designed for a significant intraparenchymal volume flow (Pardridge 2005).
- Opening of the tight junctions via osmotic BBB disruption or ultrasound. The osmotic disruption is also considered a surgical approach since it envisages the use of anesthesia and a catheter. Furthermore, it is carried out in surgery room. These approaches are based on the concept of tight junctions physical disruption by shrinkage of CNS endothelial cells. Thus, hyperosmolar solutions can be used to transiently breach the BBB. Instead, focused ultrasound (FUS) provides the advantage of a selective and regional permeability increase resulting in enhanced local delivery within the brain. Additionally, incorporation of intravenously administered lipid-encapsed perfluorocarbon gas microbubbles lowers the frequency threshold for BBB disruption, thereby allowing for much

lower and safer frequencies to be used (Bellavance, Blanchette and Fortin 2008, Etame et al. 2012).

Current techniques described above present all an unassailable limiting step: they are invasive and involve a high risk of severe side effects. Indeed, the strategies involving BBB disruption for brain drug delivery includes the risk of treatment-induced seizures , temporary altered level of consciounsness and brain herniation that are even related to some mortality events (Kamphorst, de Boer and Gaillard 2002). CED leads to diffuse white matter astrogliosis observable in autopsy of primate brains as highlighted in a study of Ai and colleagues (Ai et al. 2003). On the other hand, ultrasound-based approaches need further investigation to prove their safety since there is a possible risk of tissue damage due to ultrasonic exposure (Meairs and Alonso 2007). The just described considerations reporting a consistent number of evidences for the lack of complete safety related to the actual therapies raise obvious concerns about their long-term effects in humans. Additionally, the limiting factor of the need of paramedical personnel and surgery rooms for the above described treatments should not be underestimated. The possibility of having a drug which could be systemically administered would provide the optimal therapeutic condition, which, is still missing.

The only situations that do not only relay on the opening of the BBB for therapy are the rare cases where, the pathological mechanisms by themselves, affecting BBB integrity, might offer the possibility to access the brain. This is for example the case for TBI (Kwon et al. 2016) or cancer (Caraglia et al. 2012) due to creation of pathological fenestration in the brain microvessels. Still, also in these cases, an enhanced delivery would be beneficial.

The goal of this doctoral study has been grounded to the need of finding a new therapeutic approach for the unsolved problem of BBB drug crossing and therapeutic molecule brain penetration. Therefore, my PhD research was based on the following robust scientific statements. In humans, approximately 400 miles of capillaries perfuse the brain, and the surface area of the brain microvascular endothelium is around 20 m^2. The density of the microvasculature in the brain is so intricate that no neuron or glial cell is more than 20 µm away from its own

microvessel (Urayama and Banks 2005). Furthermore, the trophic support of the whole brain is guaranteed by the fact that every neuron has virtually its own connection to a microvessel (Begley and Brightman 2003). Consequently, based on these statements, the idea of delivering drugs via the NVU interface is one of the most promising strategies to target the whole brain efficiently (Banks 2016).

1.3 Nanotechnology: a promising approach for development of new therapeutic strategies

Nowadays, the increasing number of reports on designing compounds in the nanometer scale may lead to the development of novel strategies for non-invasive therapy of neurological diseases. Nanoparticles (NPs) are defined as particulate dispersions or solid particles with a size usually in the range of 10-1000 nm. A possible drug can be dissolved, entrapped, encapsulated or attached to a NP matrix (Singh and Lillard 2009). The potential of NPs as delivery system is grounded to the following characteristics:

- The possibility of easy manipulation of particle size and surface to achieve both passive (bearing no affinity ligands; directly related to inherent NPs biophysicochemical properties) and active (incorporation of affinity ligands with specificity for diseased tissues and cells) drug targeting after systemic administration (Kamaly et al. 2012).
- The ability to potentially control and sustain release of the drug during the transport and at the site of localization and subsequent clearance of the drug so as to achieve increase in drug therapeutic efficacy and reduction in side effects (Bamrungsap et al. 2012).
- Optimal modification of the surface to improve and increase the drug loading possibility leading also to the opportunity of targeting ligands attachment for site-specific delivery (Kamaly et al. 2012).
- The advantage of being used for various routes of administration including oral, nasal, parenteral, intraocular etc. (Rai and dos Santos 2017)

In the past few years many NP types were developed to deliver different drugs to specific target tissues also leading to a broader understanding of the mechanism of their uptake in the brain and intracellular trafficking. Despite all this described theoretical potentials of

nanosystems, a generation of nanotrasporters with broad possibilities of drug functionalization, high delivery efficiency and high biocompatibility is not available yet.

1.4 From protein-based nanomaterials to dendronized streptavidin bioconjugates

Among the many types of NPs developed over time, natural biomolecules-based nanosystems for therapeutic applications have gained an increasing interest in the scientific community due to their biocompatibility, biodegradability and various possibilities for surface modifications including the covalent attachment of targeting ligands and drugs (Wang and Uludag 2008). Indeed, nature can be considered as an extraordinary library rich in chemical compounds selected by evolution to match a great variety of biological functions. In biology, the molecular self-assembly is a fundamental process governing the most important functions necessary for life in all the organisms (Sgarbossa 2012). While thinking about the formation of cell membranes or multi-protein complexes (eg. ribosomes, RNA polymerase) as well as the folding of nucleic acids or proteins from polypeptide chains, it becomes clearer and clearer the fascinating potential of biomolecules. Proteins represent the most abundant molecules in biological systems. There are twenty different aminoacids that can get combined forming a large diversity of proteins playing a broad set of biological functions. Thus, biomedical strategies using the inner biological properties of proteins started to be the focus of the work of many researchers.

In the context of protein therapeutics at the present, more than 130 different proteins or peptides are approved for clinical use by the US Food and Drug Administration (FDA), and many more are in development. Protein therapeutics have several advantages over small-molecule drugs. First, proteins often serve a highly specific and complex set of functions that cannot be mimicked by simple chemical compounds. Second, there is often less potential for protein therapeutics to interfere with normal biological processes and cause adverse effects. Third, these agents are usually well-tolerated from the body since they are naturally produced; indeed, they are less likely to elicit immune responses. Fourth, the clinical development and FDA approval time of protein therapeutics may be faster than that of small-molecule drugs. Thus, proteins becomes extremely attractive also from a financial perspective compared with other small-molecule drugs, which it is a point not to be underestimated in designing new compounds for clinical applications (Lagassé et al. 2017).

The inordinately complex arrangement of aminoacid repeating unit chemistry, perfectly sorted with 3-dimensional order in a confined nanometer volume and the peculiar structure-function relation of proteins became new leading principles in nanotechnology pushing the polymer chemistry to explore more efficiently the field of biomedical applications of synthetic polymers (Cole et al. 2017, Duncan 2006).

Today, the term “polymer therapeutics” describes polymeric drugs, polymer-drug conjugates, polymer-protein conjugates and multicomponent poliplexes. Such bio-nanotechnologies are raising the hope that it will help realize the full therapeutic potential of the post-genomic era. An advantage for polymer therapeutics compared to other nanosystems is the versatility of synthetic chemistry, which allows tailoring of molecular weight, addition of biomimetic features to the backbone construct and the opportunity of including bioresponsive elements. The last decades have seen research at the interface of polymer chemistry and biomedical sciences giving birth to the first nano-sized polymer-based pharmaceuticals (Duncan, Ringsdorf and Satchi-Fainaro 2006). In this field, the advent of dendrimer chemistry has brought many potential new prospects. Dendrimers are highly symmetric, spherical, hyperbranched molecules with well-defined, homogeneous and monodisperse structure carachterized by a typically symmetric core, an inner shell and an outer shell (Abbasi et al. 2014). They allow control over size, liquid solubility, a multitude of functionalization possibilities, as well as the advantage of loading with different types of drug cargo. Their chemical homogeneity, the possibility of increasing their size by repeated addition of chemical moieties and a high density of surface groups that are suitable for ligand-attachment make them an exceptional candidate for various biomedical applications (Gothwal et al. 2015). Additionally, over time, the increasing number of studies revealed new inherent therapeutic potential of denrimers (antiprion, antitoxin, and antiamyloidogenic effects (McCarthy et al. 2013, Lim et al. 2010, Förstner et al. 2014, Klementieva et al. 2013)). These achievements became of great interest also for neuroscientists exploring dendrimers biomedical applications for treatment of neurological disorders. Many dendrimer-drug-conjugates have been introduced to the scientific community in the last years bringing new advances for example in treatment of glioblastoma (G3-succinamic acid dendrimer- curcumin (Gamage et al. 2016)), hypoxia (HIF-1α siRNA/2G-NN16 carbosilane dendrimer (Posadas et al. 2009)), Parkinson´s disease (dendrigraft poly-L-lysine- PEG-Angiopep (Huang et al. 2013)). Furthermore, several studies highlighted the positive effects of PAMAM dendrimers

treatments on neuroinflammation in mouse either canine models of cerebral pulsy as well as Rett syndrome although letal outcomes could not be avoided (Dai et al. 2010, Zhang et al. 2017). However, some cases drew attention to the need of very careful evaluation on the biocompatibility of dendrimers. Indeed a representative case for this controversy is the work of Klementieva and colleagues providing poly(propyleneimine) (PPI) glycodendrimers which exhibits good antiamyloidogenic effects but at the same time cause cognitive decline in WT mice (Klementieva et al. 2013).Thus, despite the investigated and described dendrimer systems for CNS applications, dendrimers with high biocompatibility as well as new linker strategies and possibilities to transport biologicals (e.g. therapeutic proteins) for optimized CNS diseases application are still an unmet need as highlighted in the review articles by Leiro et al. and Mignani et al. (Leiro et al. , Mignani et al. 2017).

In this doctoral work, the ability to cross the BBB of multifunctional dendrimer-protein which mimics endogenous proteins with a size of 5 nm and a patched surface using a streptavidin adapter coated by poly-amidoamine (PAMAM) dendrimers (DSA, dendronized streptavidin) was evaluated (Figure 3). DSA were designed, synthesized and kindly provided by Dr. David Ng working in the group of Pr. Dr. Tanja Weil at the Max Planck Institute for polymer research.

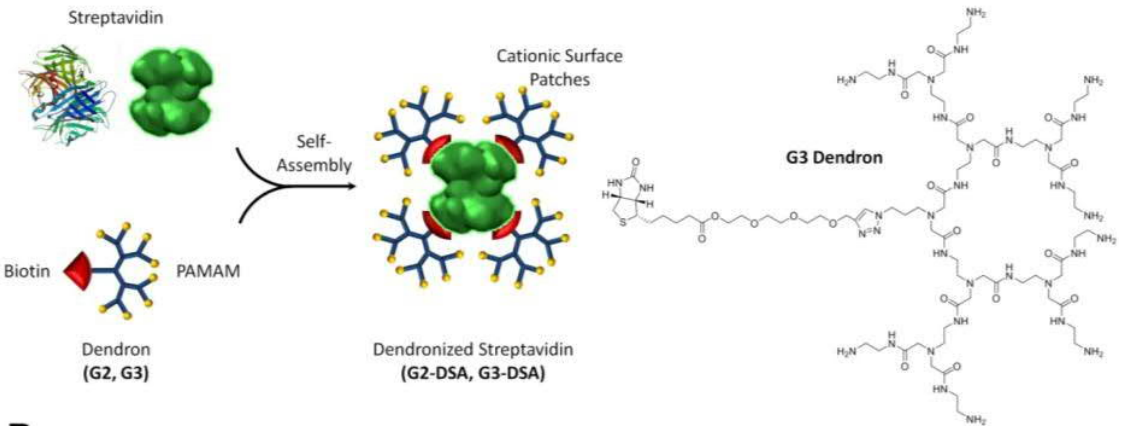

Figure 3. Scheme of dendronized streptavidin assembly. The detailed G3 dendron structure is given (modified from Moscariello et al., 2018).

1.4.1 Streptavidin: a flexible scaffold for biomaterials assembly

Streptavidin (SA) is a 56 KDa homotetramer from the bacterium Streptomyces avidinii that binds up to four biotin molecules with an extraordinary high affinity (K_d ~ 10^{-14} M). The protein is unusually stable against heat, denaturants, extremes of pH and to activity of proteolytic enzymes. These properties have rendered streptavidin an outstanding tool for the different bioscientific fields. The tenacious protein-protein interaction between SA and biotin opened the door to the development of many applications. Thus, most SA-based applications require biotinylation of target molecules. In recent years, many improvements have been reached in biotinylation techniques, both chemical and enzymatic, which have played an important role in advancing the SA-biotin technology in new areas (Jain and Cheng 2017).

Since the core of a dendrimer is generally inconsequential towards targeting and recognition, substituting it with a protein core provides an elegant approach towards both synthesis and biocompatibility without compromising the monodispersed nature of both species. The system presented here achieves the possibility to modulate the positive charge on the surface, which is important for membrane-protein interaction and cellular uptake.

To our knowledge, the presented simple and elegant dendrimer system would allow for the first time to employ both the inherent therapeutic functions of PAMAM dendrimers described above (Lim et al. 2010, Förstner et al. 2014, Leiro et al. 2015) and therapeutic effects of multiple drugs (including biologicals) in the same system attached to the streptavidin core by biotin-click-chemistry.

1.5 From nanotheranostics to fluorescent Nanodiamonds

The development of nanosystems for biomedical application and drug delivery as well as the discovery of intrinsic peculiar properties of many nanomaterials such as unique imaging and functionalization capability led to the emergence also of a new “branch” of nanotechnology: the nanotheranostics. The term “nanotheranostics” defines compounds on the nanometer scale potentially providing a synergistic combination of therapeutics with diagnostic agents

(Jeelani et al. 2014, Kim, Lee and Chen 2013). Taking disease diagnosis in its strictest sense, the adequacy and the actual suitability of nanotheranostics is disputable. Indeed, nanotheranostics should be interpreted more as the action of monitoring the route and the therapeutic efficacy of a given drug (real time drug distribution monitoring), or the prediction of a potential treatment response. This approach also aims to reduce side effects achieving a sufficient concentration of the therapeutic agent in the target and a maximum tolerable concentration in off-target organs and to switch from conventional to personalized medicine, also optimizing treatment costs (Jeelani et al. 2014, Lammers et al. 2010). At the moment, several different types of radionuclide-labeled antibodies, liposomes, polymers and micelles have been subjected to biodistributional analysis over the years, both in animal models and in patients, and it has become clear that such studies substantially assist in improving our understanding of the drug delivery process, as well as in predicting the therapeutic potential of mostly tumor-targeted nanomedicines (Kievit and Zhang 2011, Lammers et al. 2010). Many nanomaterials have been shown to be extremely useful for theranostics applications. For example the unique physical properties, chemical versatility, and cargo loading capacity of carbonaceous nanoparticles were particularly discussed in their use as potent cancer therapeutics. For instance, most of these carbonaceous nanomaterials possess strong absorption in the infrared or near infrared regions, which is useful for photothermal therapy of cancer and drug response monitoring. Some of these inorganic nanomaterials (e.g., carbon nanotubes or nanodots, nanodiamonds) can also produce fluorescence in the visible and infrared regions for fluorescence imaging. In addition, carbonaceous nanomaterials are able to transform the energy from a laser into acoustic signals, which makes them promising agents for photoacoustic imaging. Finally, intrinsic Raman vibration signals from carbonaceous materials can further provide a reliable method to monitor their distribution and metabolism in vivo (Chen et al. 2015, Kim et al. 2013).

1.5.1 Nanodiamonds as suitable nanotheranostics agents

Nanodiamonds (NDs) are a new very promising class of carbon nanocompounds for nanotheranostics, which I would like to introduce in more details. NDs are characterized by peculiar optical and magnetic properties, biocompatibility, high thermal conductivity and electrical resistivity, chemical stability and resistance to harsh environment.

Nanoscale diamond particles were first produced by detonation in the USSR in the 1960s, but they remained essentially unknown to the rest of the world until the end of the 1980s. Researchers started to use fluorescent NDs (fNDs) as a non-toxic alternative to semiconductor quantum dots for biomedical imaging. Then, nanoscale magnetic sensors based on NDs were designed. New environmentally benign purification techniques were developed and these allowed high purity NDs powders with controlled surface chemistry to be produced in large volumes at a low cost. The implementation of elemental defects (e.g. nitrogen vacancy) in the internal structure leads to a stable and size-independent fluorescence (Balasubramanian et al. 2008, Mochalin et al. 2011). Nitrogen vacancy (NV), a nitrogen atom next to a vacancy, can be created by irradiating NDs with high-energy particles (electrons, protons, helium ions), followed by vacuum annealing at 600-800 °C. Irradiation forms vacancies in the diamond structure, and during annealing these vacancies migrate and get trapped by the nitrogen atoms that are always present in diamond. Recently, NDs have been shown to improve the sensitivity of MRI thanks to their dynamic nuclear spin polarization and the presence of NV centers (Wu et al. 2016).

Finally, NDs were found to be less toxic than other carbonaceous nanomaterials and do not have noticeable side effects in vivo as in vitro thus are currently being considered for applications in biomedical imaging, drug delivery, and other areas of medicine (Zhu et al. 2012). In the field of neuroscience NDs have gained increasing interest because of their structural similarity to memantine, a well known neuroprotective drug commercially available for treatment of AD. Alawdi and colleagues have clearly demonstrated in a rat model that NDs strongly mitigate the pathological aberrations AD-related suggesting a NDs-dependent modulation of N-methyl-D-aspartate (NMDA) receptors (Alawdi et al. 2017). Unfortunately the high potential of NDs in biomedicine is strongly limited by their tendency to aggregate. Currently typical commercial suspensions of NDs contain larger aggregates hindering their biological applicability (Mochalin et al. 2011).

In the second part of this doctoral thesis the ability of fNDs encapsulated by a cationized human serum albumin-based biopolymer (dcHSA-fNDS) to cross the BBB and reach the brain in vitro and in vivo was evaluated (Figure 4). dcHSA-fNDs were

designed by Dr. Yuzhou Wu (Wu et al. 2015), synthesized and kindly provided by Weina Liu and Marco Raabe from the group of Prof. Dr. Tanja Weil at the Max Planck Institute for Polymer Research, Mainz.

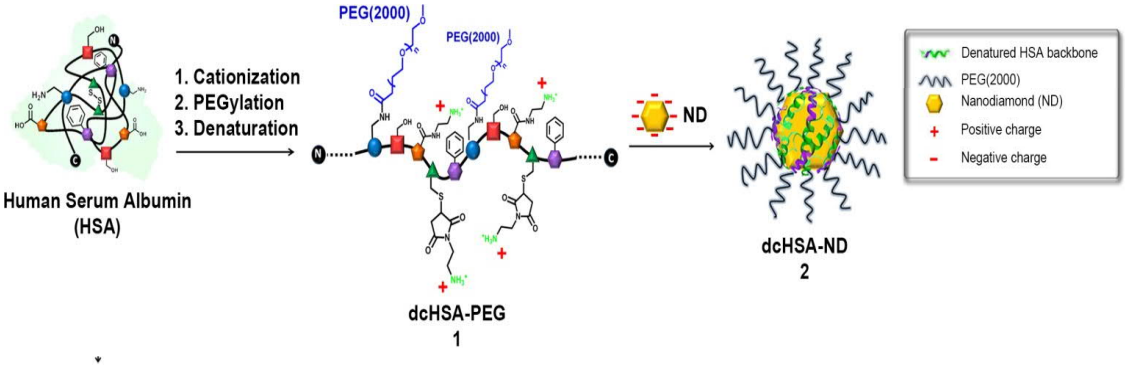

Figure 4. dcHSA-fNDs synthesis. Scheme of dcHSA-fNDs encapsulation by HSA-based polymer (modified from (Wu et al. 2015)).

1.5.2 Albumin, a carrier system

Albumin-based nanoparticle carrier systems represent an attractive strategy, since a significant amount of drug can be incorporated into the particle matrix because of the different drug binding sites present in the albumin molecule. Due to the defined albumin primary structure and high content of charged aminoacids, albumin-based nanoparticles could allow the electrostatic adsorption of positively or negatively charged molecules. Additionally, albumin NPs can be easily prepared under soft conditions by coacervation, controlled desolvatation or emulsion formation. Commercially, what makes albumin a more charming molecule is that it can be obtained in high quantities from egg white, bovine serum and human serum and it is also available from soybeans, milk and grains (Khanadeev et al. 2017, Elblbesy 2016). Due to its high concentration in plasma, human serum albumin (HSA) is not associated to significant extents with safety or immunogenicity concerns. In addition, HSA is not a standard protein since it is extremely robust towards pH (stable in pH range of 4-9), temperature (can be heated at 60 °C for up to 10 h) and organic solvents. These properties as well as its preferential uptake for example in tumor or inflamed tissues, its ready availability, biodegradability and lack of toxicity make it an ideal candidate for drug delivery (Karimi et al. 2016). In nanotechnology,

coating of NPs with HSA can be used for effective incorporation of various drugs due to its extraordinary ligand binding capacity, providing a scaffold for a wide variety of compounds for transport in the body and release at the cell surface (Vismara et al. 2017). Furthermore, albumin-based NPs are expected to be well tolerated, which is supported by previously published clinical studies with registered HSA-based formulations such as Albunex™ and Abraxane™ (Geny et al. 1993, Ibrahim et al. 2002).

Although theranostics is giving much improvement in several scientific fields, such as cancer therapy as just discussed above, the development of neurological diseases nanotheranostics approaches represents still a great unsolved challenge. The ability to deliver imaging agents and therapeutics across the BBB using NPs has the potential to transform the field of neurological disease, and may be the key to cure some diseases that currently have inadequate treatment options.

2. Aim of the study

Neurological disorders have a high social impact due to severe morbidity and mortality. The blood-brain barrier (BBB) represents the biggest hurdle to overcome in the drug development process for neurological disorders. Of particular need are biocompatible platforms, which can be loaded with multiple drugs to reach the target site: the brain. The aim of this study is to evaluate two nanosystems in their ability to overcome the BBB in order to deliver therapeutics or diagnostic tracers to the brain. The first system, DSA, is composed of an adapter of tetrameric streptavidin linked to biotinylated PAMAM dendrimers suggesting high flexibility and high drug loading possibilities via biotinylation of cargo-molecules. The second system, dcHSA-fNDs, is composed of a fluorescent nanodiamond core coated with a human serum albumin-based biopolymer, giving rise to a potential nanotheranostics platform due to the inner optical and magnetic properties of fNDs and the high functionalization capability of serum albumin.

In this thesis the following scientific questions were addressed: (1) Are DSA and dcHSA-fNDs taken up by NVU cells and transported in an in vitro BBB model from luminal to abluminal? (2) Which are the underlying mechanisms of the transport? (3) Do DSA and dcHSA-fNDs affect vitality of NVU cells and BBB integrity? (4) Are DSA and dcHSA-fNDs able to cross the BBB and how are they biodistributed in vivo?

These questions needed to be addressed to finally evaluate the investigated nanosystems for possible biomedical applications in treatment of neurological disorders, still presenting a lack of efficient therapies.

3. Materials and Methods

3.1 In vitro assays for evaluation of BBB crossing capability of DSA and dcHSA-fNDs

As described by Wilhelm and Krizbai in their exhaustive review article about BBB models, the best way to study the BBB is unquestionably in vivo. Given that in vivo experiments are becoming more and more expensive and less suitable for medium or hightroughput screening, the development of advanced BBB in vitro models provided a simple and efficient way to study BBB functions and drug discovery. Indeed, in vitro models fulfil the most important criteria required by pharmaceutical industry. Obviously, the development of these simplified models needs the acceptance of several compromises in terms of costs, capacity, time and predictive value. The parameters that a good BBB model has to respect are mostly reproducibility, low paracellular permeability and expression of functional transporters. Transendothelial electrical resistance (TEER) measurement and apparent permeability (Papp) of marker molecules represent the two most important criteria to be evaluated and taken into account. Over time, many BBB models employing many different cell types have been investigated in order to improve the in vitro modelling. The simplest models are mono-cultures of cerebral endothelial cells on microporous membranes. The pores of the membrane allow exchanges of solutes between the luminal and the abluminal compartments. The major disadvantage of mono-cultures is represented by the absence of stimulating factors derived from other cellular components of the NVU. This is the reason why co-culture models have been developed to mimic the in vivo anatomy of the NVU inducing and maintaining barrier properties. In fact, really important is the contribute of astrocytes during adulthood on the interendothelial junctions, which determines permeability, and also on the modulation of transporter expression. Astrocytes can be co-cultured with endothelial cells on the bottom side of the microporous membrane allowing a direct contact between the two cell types via astrocytes protrusion across the porous. However, due to the relatively low density of the pores, the coverage of the endothelial surface is only a fraction of what can be observed in vivo. A second option can be the seeding of astrocytes at the bottom of the well on the abluminal side of the transwell system. This model configuration enables soluble factors to exert their effect. An alternative approach is to use astrocyte-conditioned medium although in this case the influence of endothelial cells on the release of different factors by astrocytes is excluded.

Finally, a triple co-culture model is even more efficient in mimicking the in vivo BBB physiology. In this model, pericytes, neurons or neuronal progenitor cells can be introduced. A novel triple cell neurovascular unit model employing brain endothelial cells, astrocytes and neurons was recently established and provided the inspiration for the model used in this doctoral thesis. TEER values for this triple co-culture system increased with 35.9 % compared with corresponding endothelial mono-culture. High expression of p-glycoprotein and decrease in permeability were also observed.

About the endothelial cells involved in BBB in vitro models the choice can fall among many different cell types. Primary cultures are the first choice for drug permeability studies. With respect to the tightness of the barrier, primary porcine brain endothelial cells seem to be the best. Unfortunately isolation of primary cells is often complicated and costly and the cells might differ from batch to batch. Therefore, the use of reliable brain endothelial cell lines is broadly accepted. One of the major problems of cell lines is the poor barrier property. Among the many cell lines used in BBB models, bEnd.3 cells were shown to have relatively low permeability and high expression of ZO1 as indicator of high expression of tight junctions, compared for example to MBEC4 and bEnd.5 also commonly used in BBB in vitro models.

In order to obtain a model suitable for drug delivery studies, optimization of culture conditions seem to be of crucial importance. Indeed, components of the culture medium might also contribute to the formation of a tight barrier. In this respect, elevated intraendothelial cAMP levels have been shown to be important. Hydrocortisone in physiological concentration is also often used to improve barrier properties.

At the end of this introduction to BBB in vitro models, a clear statement seems to emerge: there is no ideal model. Each one has its own advantages and disadvantages. Therefore, a suitable and appropriate model has to be selected based on the specific study (Wilhelm and Krizbai 2014).

3.1.1 Culturing of bEnd.3 cells

The murine line, bEnd.3, from brain endothelioma (American Type Culture Collection, Manassas, VA, USA) was cultured as recommended by the manufacturer (Montesano et al. 1990). Cells were cultivated at a humidified atmosphere with 37°C and 5 % CO_2 in DMEM (Glutamax, gibco by life technology, Darmstadt, Germany) supplemented with 10 % fetal calf serum (Biochrom, S0115) and 2 % penicillin/streptomycin (Pen/Strep) (Invitrogen GmbH, Karlsruhe, Germany). Cells were seeded with 80.000 cells per insert (0.3 cm^2) or 100.000 cells per coverslip (80.000 cells per coverslips for experiment on the identification of tunnelling nanotubes).

3.1.2 Isolation of Porcine Brain Endothelial Cells (PBECs)

Porcine brains were obtained from butcher Färber in Alzey, Germany and incubated on ice during the transport in temporary buffer (10 % HEPES, 1 % Pen/strep, 1 % Ciprobay 200 Bayer, 1 % Fungizone). Primary brain microvascular endothelial cell isolation was established during this doctoral thesis with modifications to the previously described protocol by Freese et al (Freese et al. 2014). Brain hemispheres were incubated 1 h on ice in incubation buffer (10 % HEPES, 1 % Pen/Strep, 1 % Ciprofloxacin Kabi 400 mg/200 mg, 1 % Fungizone). Brain emispheres were placed in petri dishes with PBS on ice. Meninges were removed; emispheres were washed with PBS and the gray matter isolated and maintained in PBS, minced by scalpel, collected in a 50 mL tube filled with PBS and centrifuged at 1400 rpm for 10 min at 4°C. PBS was removed and tissue slices were maintained for 30 min at 37°C in digestion mix composed by 1 mL of DMEM, 20 mg of Collagenase IV (2ml) (Worthington; LS004210) and 20 µg of DNase I (20 µL). During the incubation time the pellet was resuspended by pipetting up and down 10 times every 10 min. PBS was added to a final volume of 50 mL and the disaggregated tissue was centrifuged (1400 rpm, 10 min, 4 °C). PBS was discarded and the pellet was resuspended in a solution of 20 % Percoll (GE Healthcare; 17-0891-01) diluted in PBS in a final volume of 50 mL and centrifuged at 2600 rpm for 1 hr at 4°C (without brake). The upper 40 mL were removed to maintain capillary fragments fraction, PBS was added up to 50 mL and centrifuged (1400 rpm, 10 min, 4°C). The supernatant was discarded and

pellet resuspended in DMEM supplemented with 2 mg of Collagenase/Dispase (Roche, 10269638061) and 20 µg of DNase I in a total volume of 2 mL collecting the pellet from two emispheres and filtered by 100 µm cell strainer. Cell suspension was maintained 10 min at 37 °C. PBS was added up to 50 mL and cell suspension centrifuged (1400 rpm, 10 min, 4 °C). The small red pellet was resuspended in 2 mL of PBS. 1 mL of the cell suspension was moved on a Percoll gradient previously prepared (24 mL Percoll + 13 mL PBS + 2 mL 10x PBS centrifuged at 10000 x g for 2 hr at room temperature) and centrifuged (2600 rpm, 15 min, 10 °C, without brake). The brain endothelial cell fraction floating in the ring on the top of the gradient was moved in a new 50 mL tube. PBS was added up to 50 mL and the tube centrifuged (1400 rpm, 10 min, 4 °C). The pellet was resuspended in EBM-2 medium (Lonza; CC-3156) containing supplements (rhFGF-B, rhEGF, GA-100, Ascorbic Acid, R^3-ICF-1, Heparin, Hydrocortisone; Lonza; CC-4114A), 15 % FCS and Glutamine (0.863 mg mL^{-1}). The all obtained cells from 2 emispheres were seeded in 10 transwell inserts and 2 coverslips precoated with fibronectin (F1141, 5 µg mL^{-1}). Finally, the brain endothelial cells were selected by puromycin (Enzo; BML-GR312-0050) treatment. At DIV 0 cells were treated with higher concentration of puromycin which was decreased in the 2 following days (4 µg mL^{-1} at DIV 0, 3 µg mL^{-1} at DIV 1 and 2 µg mL^{-1} at DIV 2). At DIV 4 puromycin treatment was removed and medium exchange (without puromycin treatment) carried out every two days.

For characterization of porcine cell growth the cell monolayer has been monitored during time and confluent cells were stained with zona occludens 1 (ZO1) as marker for the tight junctions in order to visualize one main feature of tight brain endothelial monolayers (Figure 5). Cells were growing in clusters at first (Figure 5, white arrows). After 7 days in vitro they reached confluence forming a highly connected monolayer of cells with high expression of tight junctions.

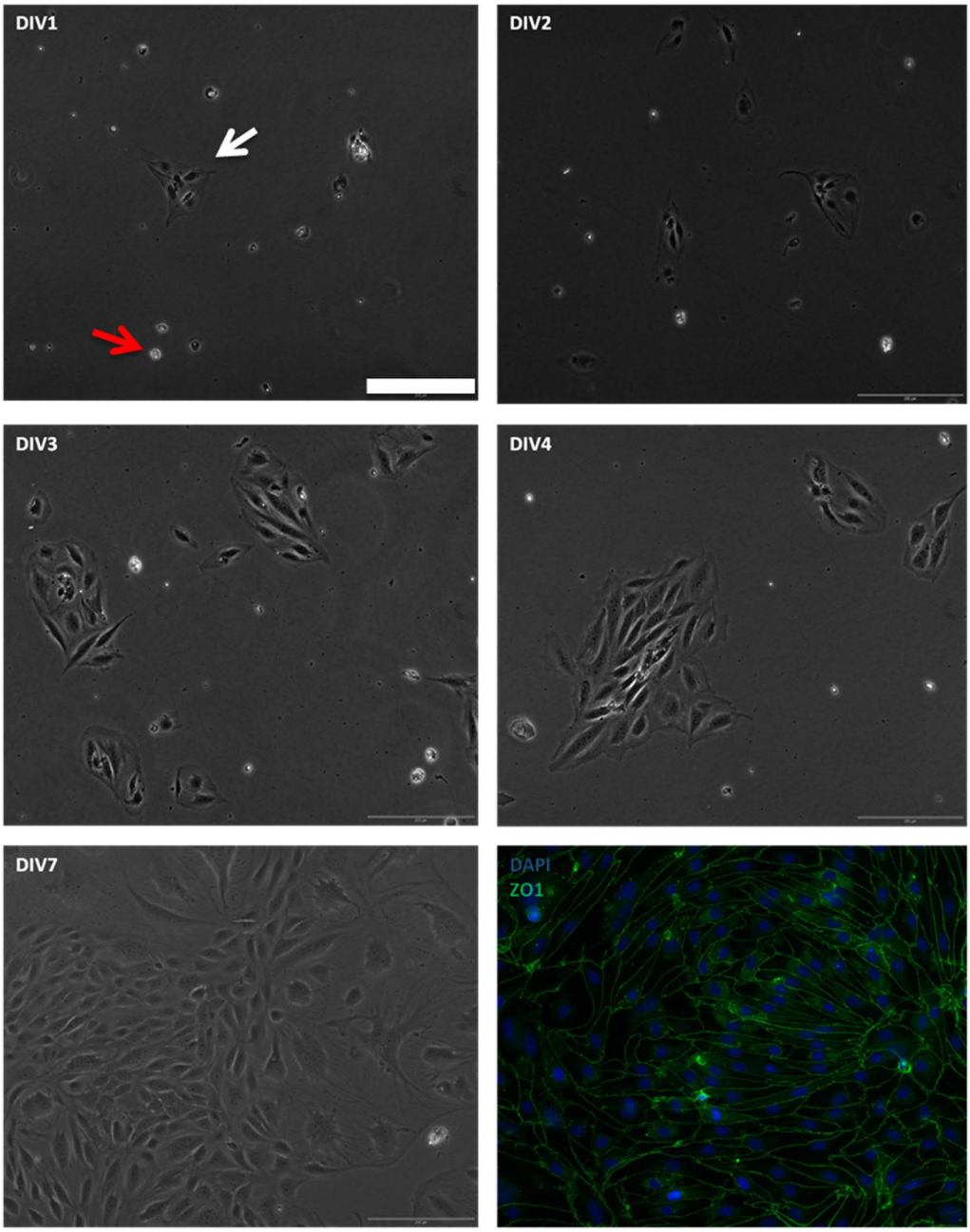

Figure 5. Culture of isolated PBECs. PBECs growth within seven days in vitro. Cells were treated with Puromycin the first three days after isolation to purify culture from pericytes. White arrows point PBECs clusters, red arrows point brighter signals generated by dead cells. ZO-1 stained tight junctions at DIV 7; scale bar: 200 µm.

3.1.3 Isolation of primary murine astrocytes

Primary astrocyte cultures were obtained from six mice (P3). Brains were isolated and placed in a petri dish with HBSS on ice. Meninges were peeled off and the cortex isolated in HBSS with the help of a dissecting microscope. The tissue was incubated with 0.05 % trypsin/EDTA for 20 min. During the incubation time tissue was resuspended by pipetting up and down 10 times every 10 min. The reaction was blocked with 10 % horse serum (HS; S9135, Biochrom) in HBSS -/- (gibco by life technology, Darmstadt, Germany) in a final volume of 10 ml. Tissue was resuspunded , filtered by a 40 µm cell strainer and centrifuged (1000 rpm, 5 min, 4°C). Supernatant was discarded and the pellet resuspended in 10 mL of culture medium (MEM supplemented with 10 % horse serum and 5 µg mL^{-1} gentamycin). Cells were seeded on poly-ornithine (P4538) coated T75-flasks. After reaching confluence, cells were split 1:3. Astrocytes were seeded with 100.000 cells/coverslip, 52.000 cells/well in IBIDI-8-Well-Chamber, 25.000 cell/insert (0.3 cm^2).

3.1.4 Isolation of primary murine neurons

Primary neuronal dissociated cell culture from mice were obtained following the protocol introduced by Kaech and Banker (Kaech and Banker 2006) and optimized by Beaudoin and colleagues (Beaudoin et al. 2012). Forebrains were collected from three mice pups (P0-1) and meninges were removed. Tissue was washed three times with maintaining solution (HBSS -/- supplemented with 5 mL Pen/Strep, 3.5 mL HEPES 1M pH 7.25, 1.5 mL Glucose 0.6 %, 5 mL sodium-pyruvate 100 mM) using Pasteur pipette and incubated for 20 min in a 5 mL aliquot of a digestion mix composed by 100 mL of 0.05 % Trypsin/EDTA (gibco by life technology, Darmstadt, Germany), 1 mL Pen/Strep, 1 mL HEPES 1 M pH 7.25. During the incubation time the tubes were carefully shaken every 5 min. DNase I (Roche, 11284932001) (2000 U in 5 ml) (500 µL) was added subsequently for 5 min at room temperature. After three washing steps with maintaining solution, tissue was disrupted in 6 mL of Neuronal Plating Medium (MEM, 10 % horse serum, 0.6 % glucose; 2ml/mouse). Tissue was dissociated using Pasteur pipette (20 times up and down; the orifice was made smaller via a fire-flame). The cell suspension was filtered by 40 µm cell-strainer and

cells stained with trypan blue (T8154) were counted. Primary neurons were seeded with cell numbers of 60.000 cells/well in 96-well-plates, 200.000 cells/coverslip (SDS treated and poly-ornithine coated) or 100.000 cells/coverslips (for experiment on the identification of tunnelling nanotubes (TNTs)) in plating medium. After 30 min medium was replaced with Neuronal Maintenance Medium [Neurobasal Medium (gibco by life technology, Darmstadt, Germany) with 2 x 10^{-3} M Glutamine (gibco by life technology, 25030024) supplemented with B27 Supplement (gibco, 17504044)]. Medium exchange has been carried out every 7 days by replacing one-third of the medium with fresh Neuronal Maintenance Medium.

3.1.5 Preparation of triple co-culture BBB model

Triple co-culture were composed by endothelial cells seeded on the luminal side of the transwell inserts (BD Fluoroblok TM Inserts, 0.3 cm^2, pore size 3 µm, Corning Incorporated, Corning, USA), astrocytes seeded on the abluminal side of the transwell inserts and neurons seeded at the bottom of the abluminal compartment as shown in Figure 6.

For the in vitro triple co-culture model P1 primary astrocytes were detached from the T75 flask by trypsinization (3 mL Trypsin 0.05 %, 37 °C, 5 min). After adding 10 mL of astrocytes medium, cell suspension from 3 flasks was collected in a 50 mL tube and centrifuged (1000 g, 10 min, 4 °C). Supernatant was discarded and the pellet resuspended in 5 mL of astrocytes medium. Cells were counted and seeded on day 0 with a cell number of 25.000 cells/insert on the abluminal side of the permeable transwell membrane by inverting the inserts on a big petri dish and dropping 100 µL on the abluminal side of the semipermeable membrane. The inserts were incubated inverted for 1 h at 37 °C. Then, inserts were placed in the appropriate 24-well plate (Corning, 353504) adding 200 µL of astrocytes medium in the luminal compartment. Additionally 25000 cells/coverslip were seeded and coverslips placed at the bottom of the abluminal compartment in 900 µL of astrocytes medium. The neurons were grown separately on CS. On day 2-3 bEnd.3 cells (passage 10-30) were seeded with 80.000 cells/insert in the luminal side of the semipermeable membrane of transwell inserts. Co-cultures of astrocytes and bEnd.

3 cells were grown in EBM-2-Basal-Medium (Lonza, Walkersville, USA) supplemented with + 15 % FCS, Glutamine (0.863 mg mL^{-1}) and EBM-2 Single Quot Kit without VEGF growth factor. TEER was measured by Evom/Endhom chamber. TEER of at least 27.5 Ωcm^2 on day 9-11 was the quality benchmark for further usage in vitro transport assay. On day 9-11 of co-culture and DIV 7-9 of neuronal culture, inserts were combined with neurons on coverslips in abluminal compartment. For transport assay TEER was monitored 24 h before and after DSA treatment.

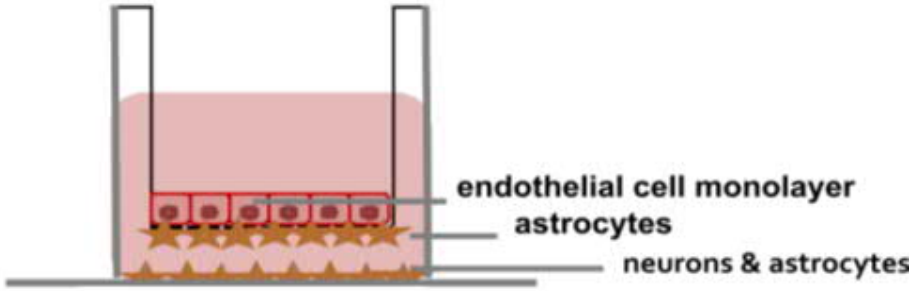

Figure 6. Scheme of triple co-culture BBB in vitro model. Endothelial cells were seeded on the luminal side of the transwell inserts, astrocytes seeded on the abluminal side of the transwell inserts and neurons seeded at the bottom of the abluminal compartment.

3.1.6 Evaluation of NPs transport across BBB

Transport of DSA or dcHSA-fNDs was investigated in transwell assay in vitro. For relative transport evaluation of DSA a mono-culture of PBECs or a triple co-culture system were used as described above; for determination of transport rates for dcHSA-fNDs a simplified model employing a bEnd.3 mono-culture was adopted by seeding cells on BD Fluoroblok TM Inserts (0.3 cm^2, pore size 3 µm, Corning Incorporated, Corning, USA) in phenol red free cell culture medium for bEnd.3 cells and placed in CellZscope device for costant TEER monitoring (380 µL in luminal compartment; 900 µL in abluminal compartment). NPs were luminal applied (45 µg $mL^{-1}$for DSAs; 30 µg $mL^{-1}$for dcHSA-fNDs) when TEER values were at least 40 Ωcm^2 for bEnd.3 monolayer and triple co-culture and 50 Ωcm^2 for PBECs. Crossing rate was quantified by rhodamine labelling of NPs. After 24 h treatment, luminal (100

µL) and abluminal (3 x 100 µL) medium were transferred in a 96 well-plate and fluorescence was measured with Infinite F1000 TECAN plate reader and the percentage of crossing was calculated. Fluorescence intensity in medium collected from the abluminal compartment of transwell system without cells was set to 100 %. Additionally, for DSA, due to differences in transport rates between PBECs monolayer and triple-co-culture, luminal was taken into account in order to calculate the estimated fraction of DSA incorporated in cells. The estimated DSA cellular fraction was obtained as follows: estimated cellular fraction = DSA initial fluorescence (abluminal + luminal fluorescence Inserts without cells) - DSA abluminal fluorescence - DSA luminal fluorescence.

Apparent permeability (Papp) was also analyzed using FITC-Dextran 4 (FD4) (46944) applied at a concentration of 100 µg mL^{-1} to the luminal side of the transwell system. After 24 h the abluminal medium (3 x 100 µL) was collected for FD4 fluorescence measurement. FD4 concentration was determined respectively to a calibration curve obtained by the fluorescence measurement of serial dilutions values. Thus, the apparent BBB permeability coefficient was obtained according to Artursson et al. 1990,(Artursson 1990) by the following equation:

$Papp = dQ/dt * 1/A*C_0$ [cm/s].

dQ/dt is the amount of transported FITC-dextran per seconds (µg/sec.), A is the surface area of the filter (0.3 cm^2), C_0 is the initial FITC-dextran concentration (100 µg mL^{-1}).

3.1.7 Measurement of transendothelial electrical resistance

TEER in the in vitro triple co-culture system was determined by EVOM voltometer with an Endohm chamber for 6 mm culture cups (World Precision Instruments, Berlin). The final TEER value (Ω x cm^2) was determined from measured ohm (Ω) subtracted by the Ω values of insert without cells, multiplied by insert surface area of 0.3 cm^2. TEER and capacitance of the cell layer (Ccl) of mono-culture systems (PBECs for DSAs; bEnd.3 for dcHSA-fNDs) on transwell insert (BD Fluoroblock TM Inserts; luminal: 380 µL, abluminal: 900 µL) was automatically determined using CellZscope device (NanoAnalytics, Münster, Germany). For PBECs, after one week

when the TEER was in exponential phase, the culture medium was replaced by EBM-2 containing supplements (rhFGF-B, rhEGF, GA-100, Ascorbic Acid, R^3-ICF-1, Heparin), 550 nM hydrocortisone, 250 µM pCPT-cAMP (C3912) and 17.5 µM RO 20-1724 (Calbiochem; 557502) to induce TEER values (Figure 7) (Patabendige, Skinner and Abbott 2013a, Rubin et al. 1991). DSA-NPs treatment have been carried out after 3 h from pCPT/RO application in order to avoid TEER values drop before the end of the 24 h NPs incubation.

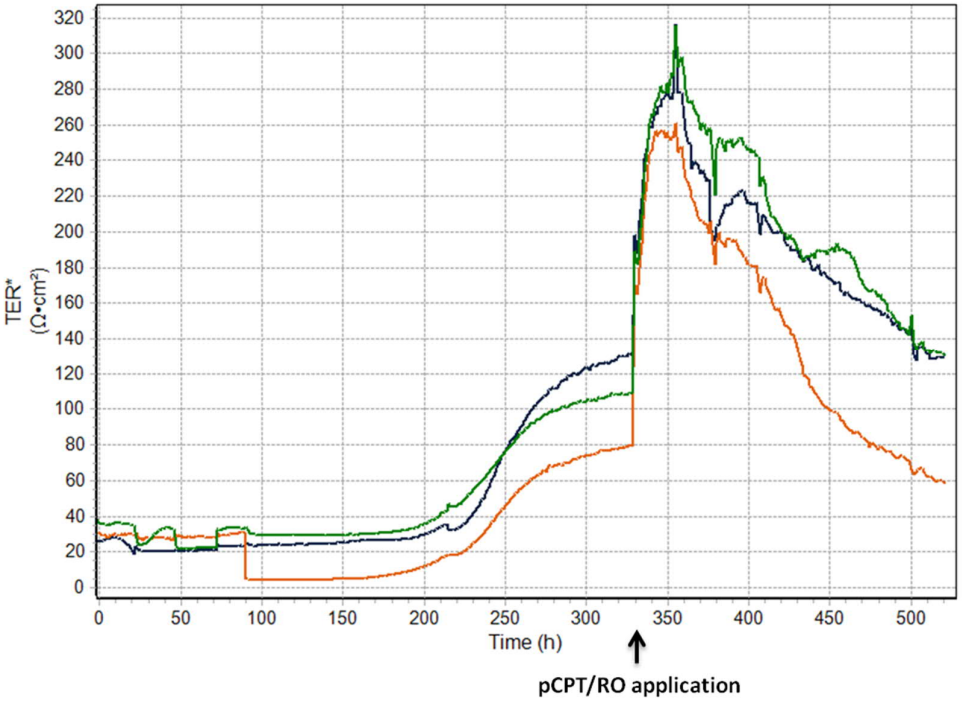

Figure 7. TEER induction via cAMP analogue application. TEER measurement of PBECs seeded on transwell inserts. TEER was induced via application of pCPT/RO (indicated by arrow) during the exponential phase of TEER increase. In the graph, three representative TEER measurements of PBECs manolayer are shown.

TEER of a surface attached bEnd.3 monolayer was determined using an Electrical Cell Impedance Sensing array (ibidi in cooperation with Applied BioPhysics, Martinsried, Germany). Cells were seeded in an 8-well chamber (ECIS culture ware 8W10E, ibidi in cooperation with Applied BioPhysics, Martinsried, Germany) and were challenged with DSA for 24 h, when cells reached maximal plateau impedance values. For all the just described methods, TEER values at time point 0 h were set to 1 and data were expressed as relative values. The experiments on effects of DSA on

BBB integrity were performed in close collaboration with Dr. Jana Hedrich and Malin Jansen (during her internship to obtain the title of Master of Science).

3.1.8 Analysis of NPs cell uptake

DSA or dcHSA-fNDs were applied to cell culture medium (45 µg mL^{-1} for DSA; 30 µg mL^{-1} for dcHSA-fNDs) for 24 h when bEnd.3 cells monolayer or astrocytes were confluent and neurons reached a stable stage of cellular specification (DIV 8-9). For co-uptake studies DSA were applied in combination to 120 µg mL^{-1} transferrin-Alexa Fluor 488 (T13342, Invitrogen) or 15 µg mL^{-1} cholera toxin B subunit-FITC (C1655). After 24 h cells were fixed with PFA 4%. Astrocytes and neurons were additionally stained respectively for glial fibrillary acidic protein (GFAP) and ß-III-tubulin or neuronal nuclear antigen (NeuN).

3.1.9 Evaluation of cell vitality

Cytotoxity was investigated using the Alamar Blue cell viability assay or TUNEL assay. Cells were DSA-treated for 24 h after reaching confluence for bEnd.3 cells, 80 % of confluence for astrocytes and at DIV 9 for neurons. For viability quantification by Alamar Blue, cells were washed with HBSS-/- three times and Resazurin (R7017, 16.66 µg mL^{-1}) diluted 1:60 in HBSS+++ (HBSS-/-, 10 mM glucose, 2 mM $CaCl_2$, 1mM $MgCl_2$) (500 µL/well for a 24-well plate; 100 µL/well for a 96-well plate) was added to each well. Two empty wells and two wells with cells treated with staurosporine (1 µM) were used respectively for blank and positive control. After 1 h incubation (37 °C, 5 % CO_2), Alamar Blue fluorescence was measured spectrophotometrically using Tecan Infinite F1000 plate reader (Tecan, Salzburg, Austria). Fluorescence values were corrected to fluorescence of the blank represented by resazurin solution without cells. Cell Viability (%) was related to untreated control cells (100 %).

Cytotoxicity was analyzed also by TUNEL assay (ROCHE, DNA Fragmentation Imaging Kit, 06432344001, Mannheim, Germany), which allows simultaneous quantification

of cell numbers and apoptotic cells. At the end of NPs treatment, the relative amount of total and apoptotic cells was quantified using the DNA Fragmentation Imaging Kit according to the user manual. The relative fluorometric TUNEL values were measured with Infinite F1000 TECAN plate reader and relative values for cell numbers and ratio of all groups were normalized to untreated control cells. Cells treated with staurosporine (1 µM) were used for positive control. All experiments were run at least 3 times in triplicates.

The experiments on effects of DSA on cell vitality (Alamar Blue and TUNEL assays) were performed in close collaboration with Dr. Jana Hedrich and Malin Jansen (during her internship to obtain the title of Master of Science)

3.1.10 Preparation of cell lysates

bEnd.3 cells treated after reaching confluence were collected in culture medium by cell scraper and the suspension was centrifuged for 5 min at 4°C at 200 x g. After 3 x PBS wash, the pellet was dissolved in 1 volume of lysis buffer (50 x 10^{-3} M Tris; 150 x 10^{-3} M NaCl; 1 x 10^{-3} M EDTA; 1 % Triton-X-100) supplemented with protease inhibitor (Roche, 1 tablet of PhosSTOP EASYpack and 1 tablet of cOmplete Tablets, Mini EDTA-free, EASYpack in 10 mL of lysis buffer) and incubated 45 min on rotation wheel at 4°C. After centrifugation for 5 min at 4°C at 13000 x g the supernatant was collected. The pellet was also dissolved in 1 volume of lysis buffer to obtain the cell pellet probe. Cell lysate and cell pellet probes were stored at -20°C.

3.1.11 Concentration of proteins in medium samples

Culture medium (100 µL) after transport assay from abluminal compartment was centrifuged at 14000 x g using Amicon Ultra 10K centrifugal filter devices (UFC501024; Millipore) (1 centrifugation of 20 min, 1 centrifugation of 10 min, 1 centrifugation of 15 min) to concentrate the protein in a volume of 20 µL according to the provided protocol.

3.1.12 Protein detection by Western Blot

Samples were separated by electrophoresis (2000 mA, 175 V, 1h) on a SDS-Polyacrylamide gel (12 % self-made or NuPAGE 4-12 % Bis-Tris Gel) and transferred (3000 mA, 30 V, overnight) onto a polyvinylidene difluoride membrane (Roth, T830.1; pore size: 0.45 µm). The membrane was blocked 30 min with 4 % non-fat milk in TBST (500 x 10^{-3} M Tris base; 1.5 M NaCl; pH 7.2; 0.1 % Tween 20). Antibodies against streptavidin (ab10020; 1:500; Abcam), LC3 (mab LC3-2G6; 1:200; Nanotools) or GAPDH (A300-641A, 1:5000, Bethyl Laboratories) diluted in 4 % non-fat milk in TBST were applied and incubated 5 h at room temperature. Finally, the protein of interest was detected after 30 min incubation with HRP-conjugated anti-mouse antibody (115-035-003; 1:5000; Dianova) or HRP-conjugated anti-rabbit antibody (111-035-144; 1:10000; Dianova) and visualized on ChemiDoc XRS+ (BioRad) by ECL Western Blotting substrate (Merck Millipore) according to the provided protocol. Proteins were quantified by densitometric analysis. The bands of the protein of interest were normalized respectively to the GAPDH band intensity of the same sample/column by using the appropriate densitometric quantification tool of Image Lab software (BioRad). Fold increase of protein of interest was expressed in relative values compared to the CTR.

3.1.13 Analysis of autophagy induction

bEnd.3 cells were treated for 24 h with DSA (45 µg mL^{-1}) or dcHSA-fNDs (30 µg mL^{-1}) in a 24 well/plate. During the last 4 h of the 24 h treatment period, cells were challenged with bafilomycin A1 (BAF; 400 x 10^{-9} M) to inhibit autophagosome/lysosome fusion. Cell lysates were then used for WB detection of endogenous LC3-II.

3.1.14 Analysis of DSA short-term lysosomal degradation

bEnd.3 cells in 24 well/plate were treated after reaching confluence with DSA (45 µg mL^{-1}) for 24 h. BAF co-treatment (400 x 10^{-9} M) was applied simultaneously or only in the last 4 h of the DSA treatment to inhibit lysosomal entrapment and degradation of DSA. DSA-streptavidin core was detected by WB on cell lysates.

3.1.15 Characterization of dcHSA-fNDs transport along TNTs

bEnd.3 cells (80000 cells/CS) or immature neurons/glia co-cultures (DIV 2) were treated with dcHSA-fNDs (30 µg mL^{-1}) for 24 h. Cells were washed with PBS and fresh medium was replaced to start the live cell imaging. For neurons/glia co-cultures, after washing step, the medium was replaced with medium from a CTR CS due to high sensitivity of primary neuronal culture to deprivation of growth factor produced during culturing. 45 minutes live cell imaging was carried out by IX81 microscope and a monochrome fluorescence CCD camera XM10 using the cellˆF Software (Olympus). Movie speed was changed using Windows Live Movie Maker to clearly visualize intracellular movements over time. Cells were further stained with rhodamine-Phalloidin (Invitrogen, R415, 1:40) to visualize TNTs by actin fibers staining. In case of neurons/glia co-cultures, in addition to rhodamine-phalloidin astrocytes and neurons were stained respectively with GFAP and NeuN by immunohistochemistry.

3.2 In vivo assays for evaluation of BBB crossing capability and biodistributional studies of DSA and dcHSA-fNDs

All experimental procedures were approved by the ethical committee of the "Landesuntersuchungsamt Rheinland-Pfalz" and the authority "Landesuntersuchungsamt Rheinland-Pfalz"; protocol number: "Aktenzeichen 23 177-07/A_2010_05_07" and "23 177-07/G 16-1-024". Principles of laboratory animal care (European, national and international laws) were followed.

3.2.1 Intravenous injection of NPs in mice

Fluorescent NPs were injected via the tail vein at a concentration of 450 µg mL^{-1} blood (900 µg mL^{-1} blood for NP-positive cells determination) for DSA and 500 µg mL^{-1} by two serial injections at a time distance of 1 h for dcHSa-fNDs in P21 (DSA)

or P29 (dcHSA-fNDs) mice. PBS-injected mice were used as CTR. As for in vitro studies, the duration of the treatment has been kept with 24 h treatment.

3.2.2 Tissue harvesting for NPs uptake analysis by confocal imaging

After the 24 h treatment, mice were deeply anesthetized (120 mg Ketamin/kg and 16 mg Xylazin/kg) and perfused with PBS supplemented with 5000 E.I. heparin-natrium (Ratiopharm) in a total volume of 500 mL and subsequently with PFA 4 %. Brain was collected as well as liver, kidney, spleen, lung and heart. Organs were incubated overnight in PFA 4 % for post-fixation. Subsequently, organs were washed three times with PBS and equilibrated in 30 % sucrose (in PBS 0.1 M, pH 7.5) for 20 up to 90 h. 30 µm slices were obtained using a freezing microtome (Leica CM 1325) and used for immunohistochemistry studies.

3.2.3 Preparation of brain lysates and quantification of DSA in vivo brain uptake

After treatment and perfusion with PBS/heparin (Ratiopharm), the collected brain was smashed by TissueRuptor (Qiagen) in lysis buffer (50 x 10^{-3} M Tris; 150 x 10^{-3} M NaCl; 1 x 10^{-3} M EDTA; 1 % Triton-X-100) supplemented with protease inhibitor (Roche, 1 tablet of PhosSTOP EASYpack and 1 tablet of cOmplete Tablets, Mini EDTA-free, EASYpack in 10 mL of lysis buffer). In order to obtain the brain lysate, the homogenate was maintained on rotation wheel 3 h at 4°C and then centrifuged for 5 min at 2000 x g. Supernatant was collected and used for WB analysis. For fluorometric quantification of DSA in vivo transport, brains were additionally weighted after perfusion. After the incubation at 4 °C, samples were sonicated (7 cycles of 30 sec) and centrifuged 10 min at 4000 x g. Cy5-fluorescence for G3-DSA was measured by Tecan Infinite F1000 plate reader. % ID and µg / g of brain tissue of transported G3-DSA were calculated referring the fluorescence values to a calibration curve obtained via serial dilutions of Cy5-DSA in brain lysates (Nance et al. 2016).

3.2.4 Evaluation of BBB integrity by Evans Blue (EB) extravasation assay

EB (MW 961 Da) is an intravital dye that in blood binds to the albumin fraction (EBA) to give rise to a high-molecular complex (EBA = 68,500 Da) unable to cross an intact BBB (Kozler and Pokorný 2003).

Thus, to study in vivo BBB integrity a solution of 2 % Evans Blue (E2129) in PBS was administered i.v. for 3 h before the end of NPs treatment. Mice were perfused with PBS/heparin for biochemical EB detection or collected without further perfusion for histochemical analysis. One emisphere from the perfused brain for biochemical EB detection was weighted and incubated in 500 µL of TCA (8789, Roth) 50 % diluted in water. The brain emispheres in TCA were then smashed by TissueRuptor (Qiagen) and incubated overnight. The day after, the samples were centrifuged for 25 min at 12000 x g. Supernatant was collected and 2 x 200 µL were loaded in a 96-well-plate for EB fluorescence measurement by Infinite F1000 TECAN plate reader. EB (µg)/brain tissue (g) was calculated referring to a calibration curve in a range from 0 to 1 µg mL^{-1} of EB in TCA.

Brains without perfusion were incubated in PFA 4 % overnight and cut in 30 µm slices as previously described for NPs uptake analysis in vivo. In case of BBB disruption histochemical results would show EB permeation and uptake in brain parenchyma (Figure 8).

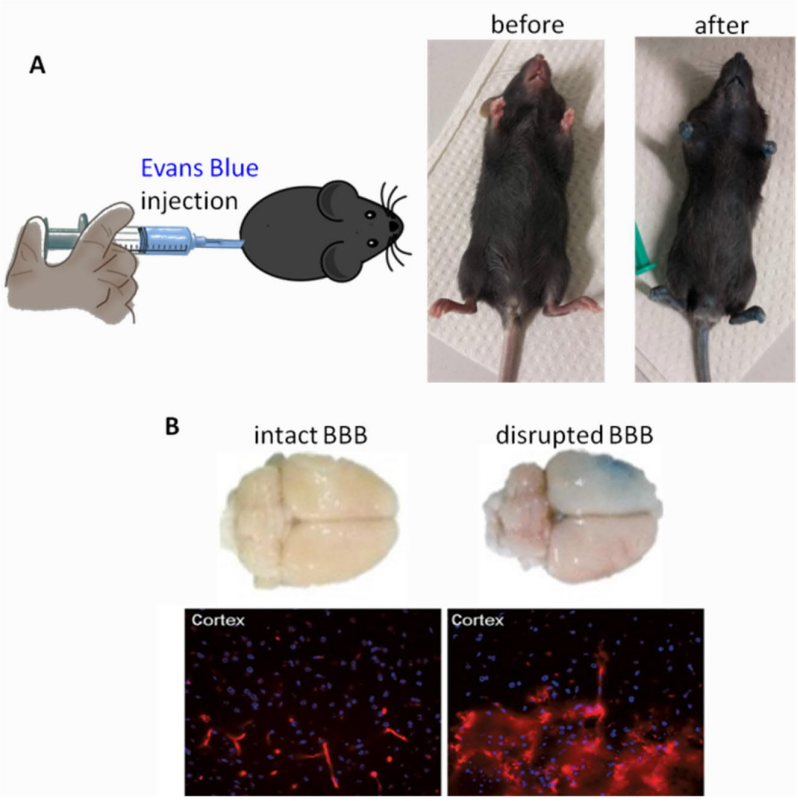

Figure 8. Evans Blue application and brain extravasation. (A) Scheme of EB application and distribution 3h after injection in mice. (B) Examples of EB extravasation in the brain. EB is observable by eyes in mice brains with disrupted BBB compared to sham animal and its extravasation is shown microscopically by EB fluorescence detection; in epifluorescence pictures EB is shown in red and cell nuclei in blue (modified from Braniste et al. 2014).

3.3 Immunocytochemical and histochemical analysis

Cells or organs were fixed with PFA 4 %. Organs were sliced in 30 µm slices. Probes were blocked and permeabilized with 7 % normal donkey serum (Dianova, Hamburg, Germany)/ 0.3 % (0.8 % for organ slices) Triton (T-8787) in PBS for 2 h at RT. If the first antibody was from mice, organ slices were at first incubated with donkey anti-mouse FAB fragment (Dianova, 715-007-003, Hamburg, Germany) in PBS 0.01 M for 2 h at RT. Primary antibody was incubated in 2 % bovine serum albumin (Dianova, 001-000-161, Hamburg, Germany) with 0.05 % azide and 0.1 % (0.3 % for organ slices) Triton/PBS overnight at RT. After three washing steps, secondary antibody and DAPI (32670) were incubated in 2 % bovine serum albumin with 0.05 % azide for 2 h at RT, followed by PBS washing. Organ slices were additionally washed with Tris-HCl 0.05 M at pH of 6.5. Cells or slices were finally embedded respectively in Fluoromount

(Biozol, Eching, Germany) or CFM-3R (Citifluor Ltd., London, UK) to reduce tissue background fluorescence.

Table1. Antibodys for immunohistochemistry

Primary antibody	Secondary antibody
ZO-1 anti-zonula occludens 1 (rabbit, Zymed via invitrogen, 61-300, 1:100)	Cy2 goat anti-rabbit IgG (Dianova, 111-25-144, 1:10)
EEA anti-early endosome antigen-1 (rabbit, Abcam, ab50313, 1:50)	Alexa Fluor 647 donkey anti-rabbit IgG (Jackson, Dianova, 711-605-152, 1:200)
LAMP1 anti-cluster of differentiation 107a (rat, BD Biosciences, 553792, 1:50)	DyLight 488 donkey anti-rat IgG (Bethyl Lab, Biomol, 1:200)
VAMP3 anti-vesicle-associated membrane protein 3 (rabbit, Synaptic System, 1:250)	Cy2 donkey anti-rabbit IgG (Jackson, Dianova, 711-225-152, 1:200)
TfR anti-transferrin receptor (mouse, Zymed via Invitrogen, 1:500)	Dylight 488 donkey anti-mouse IgG (Bethyl Lab, Biomol, A90-337D2, 1:200)
LC3 anti-microtubule-associated protein 1A/1B-light chain 3 (mouse, Nanotools, 0260S/LC3-2G6, 1:200)	Dylight 488 donkey anti-mouse IgG (Bethyl Lab, Biomol, A90-337D2, 1:200)
GFAP anti-glial fibrillary acidic protein (mouse, Synaptic Systems, 173011, 1:1000)	Dylight 488 donkey anti-mouse IgG (Bethyl Lab, Biomol, A90-337D2, 1:200)
NeuN	Dylight 488 donkey anti-rabbit IgG (Jackson, Dianova, 711-485-152, 1:200)

anti-neuronal nuclear antigen (rabbit, Merck Millipore, ABN78, 1:500)	
CD105 anti-endoglin (rat, Beckman Coulter, 732334, 1:50)	DyLight 488 donkey anti-rat IgG (Bethyl Lab, Biomol, 1:200)

3.4 Image processing and analysis

Images were taken by an IX81 microscope and a monochrome fluorescence CCD camera XM10 using the cell^F Software (Olympus) or by a TCS SP5 confocal (Leica). For quantification of intracellular colocalization, Z-stacks were deconvolved by Huygens Essential software. For uptake quantification in ImageJ, fixed thresholds were applied for DAPI and rhodamine signal and fluorescence positive particles were counted for each image. DSA positive vesicles per cell are blotted. For colocalization studies the percentage of vesicles containing nanoparticles colocalizing with the specific intracellular compartment was calculated. A threshold of 40 % of colocalization for each vesicle was set to avoid false positive values. In addition, deconvolved z-stacks were also analyzed by JacoP plugin in ImageJ to calculate Van Steensel´s crosscorrelation functions (CCFs) as proof of colocalization data.

3.5 Statistic data analysis

All data were analyzed with GraphPad Prism 5 software (Graph Pad, La Jolla, CA, USA) and were presented as mean ± SEM. Data were analyzed with the Mann-Whitney U test, ANOVA one way and ANOVA two-way with post hoc test. $P < 0.05$ was considered as statistically significant *, $P < 0.01$ **, $P < 0.001$ ***.

The in vitro experiments carried out with dcHSA-fNDs were performed in close collaboration with Sandra Bernardt and partly included in her dissertation to obtain the title of Master of Science.

4. Results

4.1 Dendronized Streptavidin for brain drug delivery via crossing an intact BBB

4.1.1 DSA are taken up by brain endothelial cells in vitro

The tightly connected layer of brain endothelial cells represents the first obstacle to the entry of molecules into the CNS. Therefore, we investigated the ability of differently charged generations of DSA (G2-DSA and G3-DSA) to be taken up by bEnd.3 cells in vitro. After 24 h of DSA treatment, DSA-rhodamine signal was detected by confocal microscopy and 3D reconstructions z-stacks were screened for DSA uptake. The results showed DSA signal in the cell of treated samples compared to control (CTR) untreated cells not as single-unit NP but as DSA-containing vesicles (Figure 9A). The quantification of the DSA-containing vesicles showed significant uptake for both generations of DSA with a significantly higher number of NP-containing-vesicles for G3-DSA than for G2-DSA (CTR: 0 ± 0 vs. GS-DSA: 0.7 ± 0.7 vesicles/cell, CTR: 0 ± 0 vs. G3 5.2 ± 0.43 vesicles/cell, G3-DSA: 5.2 ± 0.43 vs. G2-DSA: 0.7 ± 0.7 vesicles/cell, n = 28 regions of interest from 3 cultures, one-way ANOVA, $P < 0.0001$) (Figure 9B). Due to the protein core of DSA, imaging data could be confirmed by a biochemical approach. Indeed, western blot (WB) carried out on cell lysate from DSA-treated cells showed cell uptake by streptavidin core detection. NP signal was detected in cell lysate as well as in cell pellet (Figure 9C).

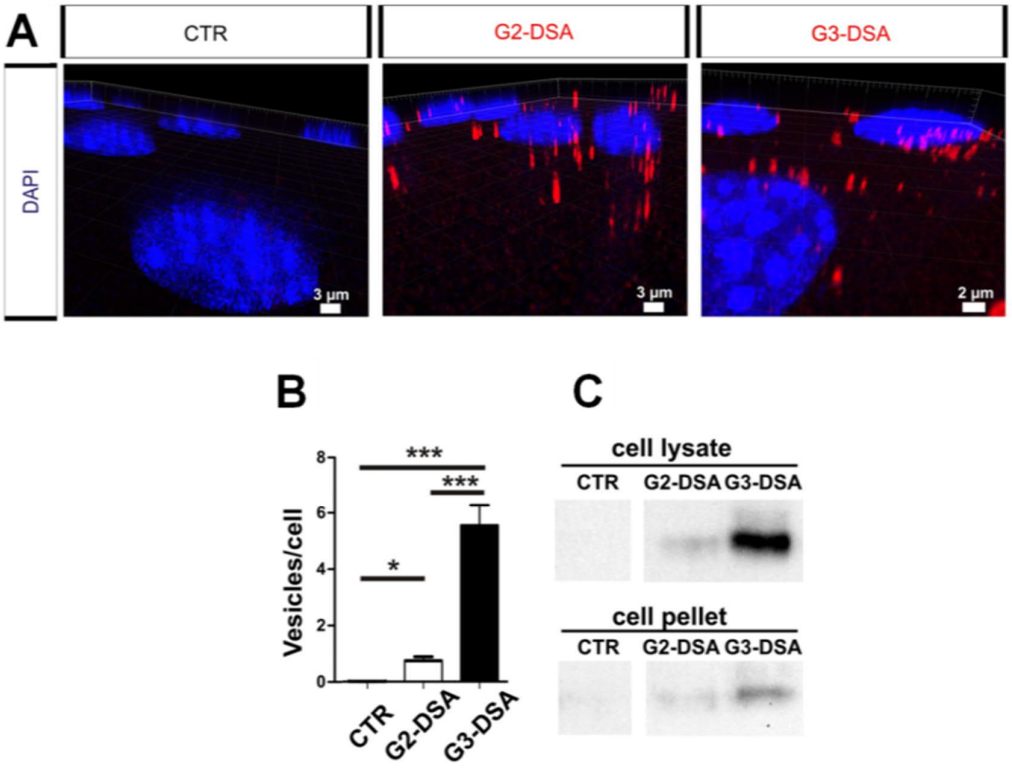

Figure 9. DSA uptake in bEnd.3 cells. (A) Confocal 3D-image of DSA (red) uptake. (B) Quantification of DSA-positive vesicles per cell. n = 28 ROIs from 3 cultures, one-way ANOVA, ***p < 0.001, *p < 0.05. (C) Streptavidin immunoblotting of cell lysate after DSA uptake.

Uptake studies proved the uptake of DSA in the first cellular barrier: the endothelial cells. Since this is the most critical part of uptake, we investigated further the co-uptake of DSA with markers for caveolae- and clathrin-mediated pathways. The two pathways were investigated, because, caveolae-mediated uptake is the most common uptake mechanism in endothelial cells (Voigt, Christensen and Shastri 2014, Hillaireau and Couvreur 2009, Frank et al. 2003) and it has been demonstrated that PAMAM dendrimers are taken up via a clathrin-mediated pathway (Albertazzi et al. 2010). bEnd.3 cells were treated for 24 h with DSA in combination with FITC-Transferrin (TF) for clathrin-mediated endocytosis and the subunit B of cholera toxin-alexa-fluor-488 (CTX) for the caveolae-mediated endocytosis in order to follow the two pathways. Confocal microscopy showed colocalization of DSA with both investigated endocytosis markers (Figure 10A). Quantitative analysis on z-stacks revealed that TF colocalizes for 7.9 ± 2.9 % of vesicles with G2-DSA and for

7.6 ± 2.12 % of vesicles with G3-DSA (n = 20 regions of interest from 3 cultures, Mann-Whitney U test, P = 0.8881) (Figure 10B). While, CTX showed a colocalization of 32.7 ± 4.9 % of vesicles with G2-DSA and 42.3 ± 4.36 % of vesicles with G3-DSA (n = 20 regions of interest from 3 cultures, Mann-Whitney U test, P = 0.2615) (Figure 10C). These data revealed uptake of DSA by both investigated mechanisms with no significant difference between G2-DSA and G3-DSA, but with a pronounced preference for the caveolae-mediated endocytosis (For G2-DSA = TF: 7.9 ± 2.9 % vs. CTX: 32.7 ± 4.9 % n = 20 regions of interest from 3 cultures, Mann-Whitney U test, P < 0.0007; for G3-DSA = TF: 7.6 ± 2.12 % vs. CTX: 42.3 ± 4.36 % colocalization with G3-DSA: n = 20 regions of interest from 3 cultures, Mann-Whitney U test, P < 0.0001).

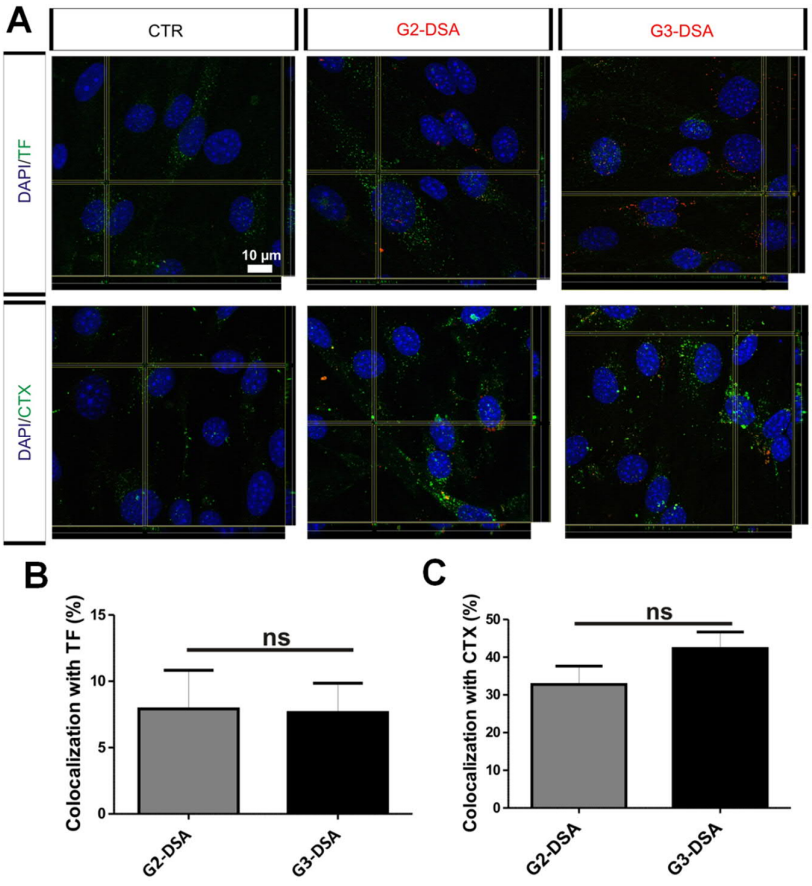

Figure 10. DSA uptake mechanism in bEnd.3 cells. (A) Confocal orthogonal view of DSA (red) co-uptake with TF or CTX (green) in bEnd.3 cells. (B, C) Percentage of colocalization of DSA with FITC-TF (B) or FITC-CTX (C). n = 20 ROIs from three independent experiments, Mann-Whitney U test, ns = not significant.

4.1.2 DSA are Efficiently Transported Across BBB In Vitro

After proving DSA uptake in bEnd.3 cells, to challenge the hypothesis of overcoming the BBB with DSA, the transport of G2-DSA and G3-DSA from the luminal to the abluminal side of two BBB transwell in vitro models was investigated. In the in vitro models employed for this experiment the luminal compartment represents the bloodstream and the abluminal compartment represents the brain. In one model porcine brain endothelial cells (PBECs) were seeded in the luminal side of transwell inserts in a monolayer system (Figure 11A). Moreover, transport of DSA was validated in a murine triple co-culture system using bEnd.3 as endothelial cell lines seeded on the luminal side of transwell inserts additionally to primary murine astrocytes in the abluminal side and primary murine neurons on the bottom of the abluminal compartment (Figure 11B). In order to investigate the ability of DSA to cross the BBB, the percentage of transport as measurement of the rhodamine fluorescence in the abluminal compartment after 24 h treatment was defined. All the values referred to the 100 % of transport represented by the passive permeation of DSA in transwell inserts without cells. In mono-culture, 15.7 ± 4.2 % of G2-DSA (n = 6 wells from 3 cultures in duplicate) compared to 100 % G2-DSA (100 % ± 4.79, n = 6 wells from 3 cultures in duplicate, one-way ANOVA, $P < 0.0001$) and 19.2 ± 1.56 % of G3-DSA (n = 8 wells from 4 cultures in duplicate) compared to 100 % G3-DSA (100 % ± 2.29, n = 8 wells from 4 cultures in duplicate, one-way ANOVA, $P < 0.0001$) were transported to the abluminal compartment (Figure 11C). Comparing the two generations of dendrimers, no significant difference in transport rates could be observed (G2-DSA: 15.7 ± 4.2 % vs. G3-DSA: 19.2 ± 1.56 %, n = 6-8 wells from 3-4 cultures in duplicate, one-way ANOVA, $P > 0.05$). Using triple-co-culture, 37.8 ± 4.01 % of G2-DSA (n = 8 wells from 4 cultures in duplicate) compared to 100 % G2-DSA (100 % ± 0.93, n = 8 wells from 4 cultures in duplicate, one-way ANOVA, $P < 0.0001$) and 21 ± 1.69 % of G3-DSA (n = 8 wells from 4 cultures in duplicate) compared to 100 % G3-DSA (100 % ± 2.3, n = 8 wells from 4 cultures in duplicate, one-way ANOVA, $P < 0.0001$) were transported to the abluminal compartment (Figure 11D) showing significant differences in transport rates for the two investigated DSA-generations apparently with a more pronounced crossing

ability for G2-DSA than for G3-DSA . The protein content of the abluminal medium was further concentrated via ultra 10K filter devices and a WB analysis was carried out (Figure 11E). Thus, bands for G2-DSA and G3-DSA on PVDF membrane confirmed the DSA transport via streptavidin core detection.

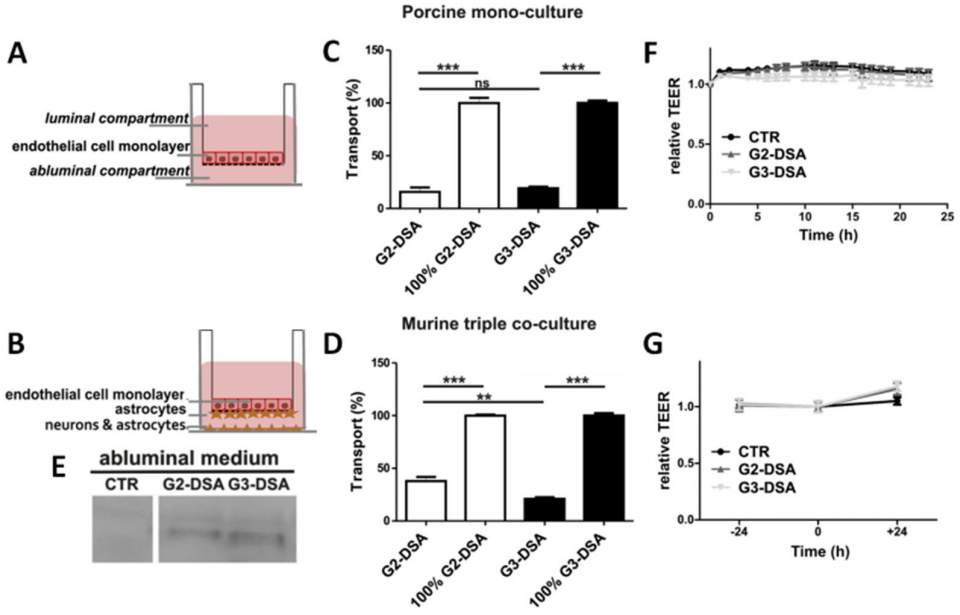

Figure 11. Transport of DSA in vitro. (A-B) Schematic illustration of transwell assay with endothelial cells seeded in mono-culture (PBECs) (A) or in triple co-culture with bEnd.3 cells and murine primary astrocytes and neurons (B). (C-D) Mean relative transport for DSA in porcine mono-culture (C) or triple co-culture (D). DSA (45 µg mL^{-1}) were applied in the luminal compartment and transport was quantified relative to transport in insert without cells (100%). One-way ANOVA, ***p < 0.001; **p < 0.01, ns = not significant. Porcine mono-culture: G2-DSA, 100% G2-DSA n = 6 wells from 3 cultures in duplicate; G3-DSA, 100% G3-DSA n = 8 wells from 4 cultures in duplicate; triple co-culture: n = 8 wells from 4 cultures in duplicate; one-way ANOVA, ***p < 0.001; **p < 0.01, ns = not significant. (E) Streptavidin immunoblotting of abluminal medium. (F,G) TEER monitoring of NPs transport assay. TEER values were determined automatically during the whole experiment by CellZscope device (F) or at -24 h, 0 h and +24 h from NP application by EVOM system (G). TEER values at t = 0 (DSA treatment) were set to 1 and each measurement expressed as relative value. Porcine mono-culture: CTR n = 6 wells from 3 cultures in duplicate, G2-DSA n = 6 wells from 3 cultures in duplicate, G3-DSA n = 8 from 4 cultures in duplicate; TEER absolute values in a range between 50 and 300 Ωcm^2. Triple co-culture: n = 8 from 4 cultures in duplicate; TEER absolute values with a mean of 45 ± 13 Ωcm^2.

In order to understand if the differences in the transport rate between the two models are attributable to preferential cellular uptake of G3-DSA, the estimated DSA fraction incorporated in cells (estimated DSA cellular fraction = DSA initial fluorescence - DSA abluminal fluorescence - DSA luminal fluorescence) was determined (Figure 12). Interestingly, for G3-DSA in the triple co-culture model a considerably higher fraction of fluorescence than mono-culture vanished from the luminal and abluminal compartments (Figure 11A), while for G2-DSA the loss of fluorescence was constant and comparable in both investigated BBB models (Figure 11B).

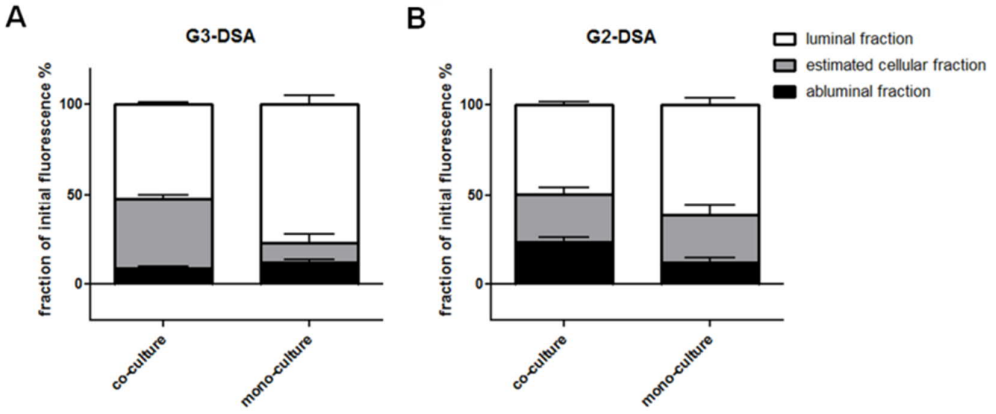

Figure 12. DSA estimated cellular fraction in BBB models in vitro. The graphs present the three different fractions obtained for transwell models after 24 h of G3-DSA (A) or G2-DSA (B) application in luminal compartment. Estimated cellular fraction = DSA initial fluorescence – DSA abluminal fluorescence - DSA luminal fluorescence. Co-culture: n = 8; mono-culture: n = 6.

To validate our in vitro transwell systems as suitable models to study the transport of DSA, transendothelial electrical resistance (TEER) was monitored continuously by CellZscope after PBECs cells seeding for monolayer model or by EVOM/Endhom chamber for the triple co-culture. The TEER measurement before and after the transport should prove the tightness of the used BBB models to be high enough to consider transport data as reliable. DSA were applied when the absolute TEER values fell in a range between 50 and 300 Ωcm^2 for porcine model or reached a mean

value of 45 ± 13 Ωcm^2 for triple co-culture. The TEER was not influenced by treatment with DSA compared with t = 0 (time point of DSA application) (Figure 11F, G). In the triple co-culture model the TEER even increased slightly during NP treatment for 24 h (Figure 11G). Hence, no paracellular leakage due to disruption of the BBB has to be expected. Since the tight junctions restrict the paracellular diffusion of hydrophilic tracers, the Papp coefficient for FITC-dextran 4 KDa (FD4) could be determined as additional validation parameter. Indeed, compounds like FD4 can be used in order to monitor paracellular diffusion (Gaillard and de Boer 2000). The average basal Papp of FD4 was 9.24 ± 3.59 x 10^{-7} cm s^{-1} in our model employing PBECs and 1.28 ± 2.21 x 10^{-6} cm s^{-1} in triple co-culture model. TEER and Papp validations proved the good quality of the used BBB in vitro models to be used for transport assessment of DSA.

4.1.3 DSA follow a transcytotic pathway without short term intracellular degradation and involvement of autophagic mechanisms

The transport of DSA from the luminal to the abluminal compartment of the transwell models implicates intracellular migration and trafficking which starts with the already discussed uptake. The focus of this study is on the understanding of the transcytotic pathway involved in the crossing of BBB. The inner life of the cells is characterized by high compartmentalization. Multiple intracellular structures and organelles with their own identity and functions can be involved in trafficking and transcytosis of nanoparticles. Hence, to clarify the molecular mechanisms how DSA cross the BBB requires a close view on this mazy “microworld”. The localization of DSA in cellular compartments was studied by using specific intracellular markers.

Co-staining with early endosome antigen (EEA) and lysosomal-associated membrane protein 1 (LAMP-1) were analyzed in order to investigate the possible localization of DSA respectively in early endosomes (EE) and late endosomes (LE). Representative orthogonal view from z-stacks revealed colocalization with both intracellular compartments in bEnd.3 cells after 24 h of DSA treatment (Figure 13A).

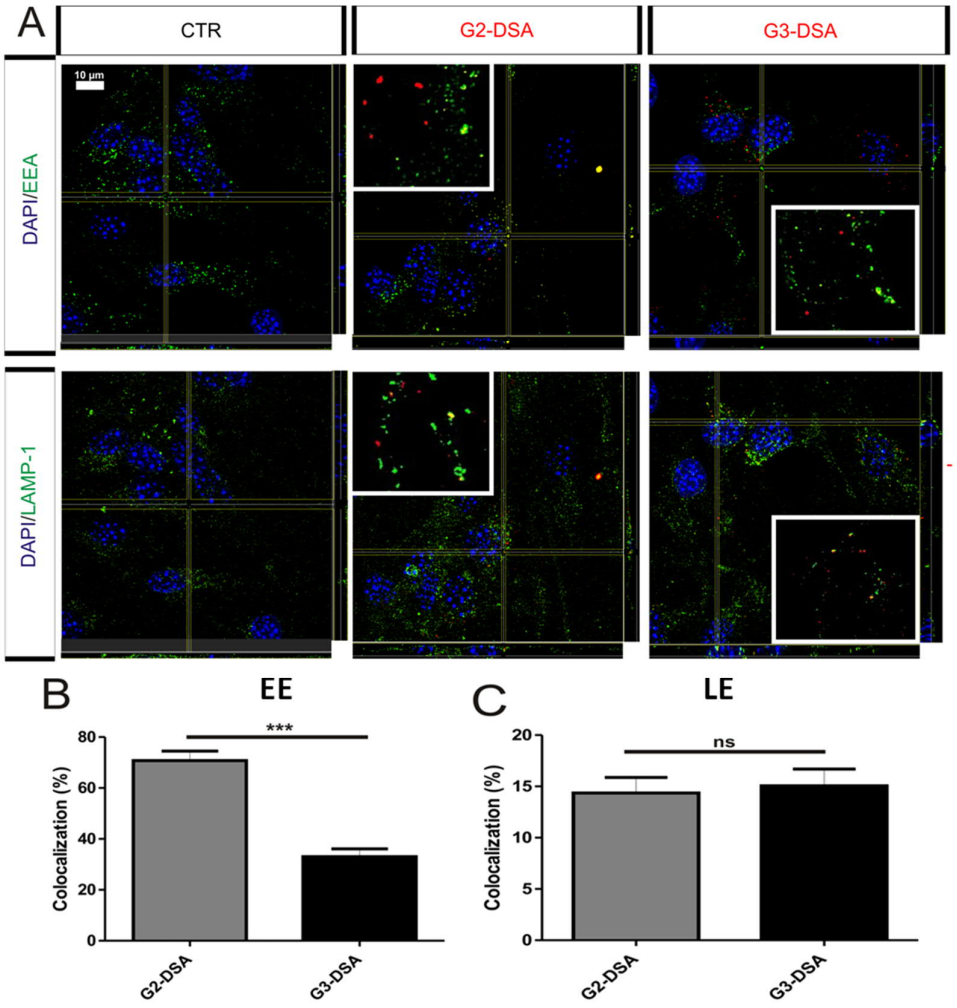

Figure 13. Endosomal trafficking of DSA in bEnd.3 cells. (A) Confocal orthogonal view for colocalization of DSA-positive vesicles (red) and early endosome antigen (EEA; green) for early endosomes, lysosomal-associated membrane protein 1 (LAMP1; green) for late endosomes. Insets: zoom of ROIs with colocalization (yellow). (B, C) Quantification of colocalization for DSA with early endosomes (B) or late endosomes (C). Data are expressed in percentage of DSA-positive-vesicles partially colocalizing for at least 40 % with endosomal vesicles. n = 24 ROIs from 3 cultures; Mann-Whitney U test, ***p < 0.001; ns = not significant.

Quantification of colocalization of DSA with EE revealed significant generation-dependent differences (G2-DSA: 70.7 ± 3.73 % vs. G3-DSA 33 ± 3.12 %, n = 24 regions of interest from 3 cultures, Mann-Whitney U test, P < 0.0001) (Figure 13B). In contrast, colocalization of DSA with LE showed a lower percentage than for EE and no difference between G2-DSA and G3-DSA (G2-DSA: 14.3 ± 1.51 % vs. G3-DSA: 15

± 1.62 %, n = 24 regions of interest from 3 cultures, Mann-Whitney U test, P = 0.7947) (Figure 13C). Nonetheless, there were still NP containing vesicles that did not colocalize with EE or LE. In order to study in which other intracellular compartments DSA localized during trafficking, several other markers of vesicular transport were tested. First, using immunocytochemistry,further experiments were focused on the possible colocalization of DSA with transferrin-receptor (TfR) and vesicle-associated membrane protein 3 (VAMP3) that has been postulated to be a vesicle soluble N-ethylmaleimide-sensitive-factor attachment receptor (v-SNARE) for early and mostly recycling endosomes, although mice with a null mutation in the encoding gene were preserving intact endocytotic pathways (Hu, Hardee and Minnear 2007, Yang et al. 2013). Tridimensional view obtained by confocal microscopy did not reveal a colocalization of DSA with Tfr- and VAMP3-positive intracellular structures (Figure 14).

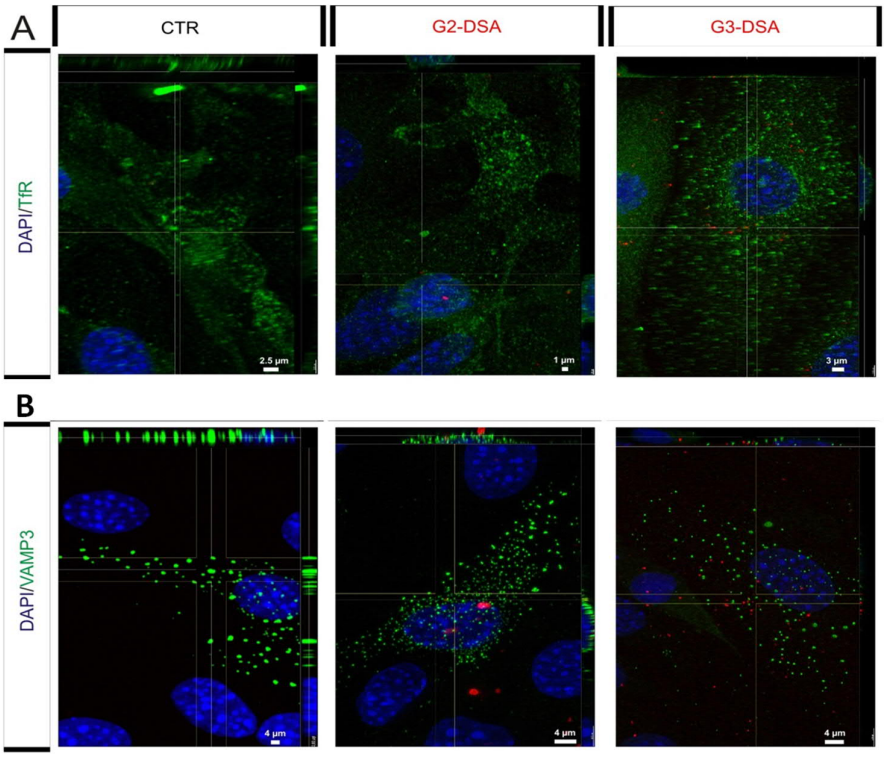

Figure 14. DSA intracellular trafficking in bEnd.3 cells. Representative confocal tridimensional orthogonal view for colocalization analysis of DSA-positive vesicles (red) and vesicle associated membrane protein 3 (VAMP3; green) (A) for recycling endosomes or transferrin receptor (TfR; green) (B).

Previous findings demonstrated that some biodegradable NP can induce autophagy and be sequestered by autophagosomes (Zhang et al. 2016). Then, the possible induction of autophagy and whether DSA localized or not in autophagosomes was further investigated. bEnd.3 cells were stained with anti-microtubule-associated protein 1A/1B-light chain 3 (LC3), which is a marker for autophagosomes. During autophagy, double membrane autophagosomes assemble in order to engulf intracellular components. A cytosolic form of LC3, LC3-I, is conjugated with phosphatidylethanolamine during the process of autophagosomal membrane formation and subsequently generates LC3-II which is recruited to autophagosomal membranes (Loos, du Toit and Hofmeyr 2014, Tanida, Ueno and Kominami 2008). Immunocytochemistry revealed that only very few NP-containing vesicles might colocalize with autophagosomes (G2-DSA: 0.8 ± 0.46 vs. G3-DSA 1.8 ± 0.86 %, n = 17-20 regions of interest from 3 cultures; Mann-Withney U test, P = 0.0244) (Figure 15A, B).

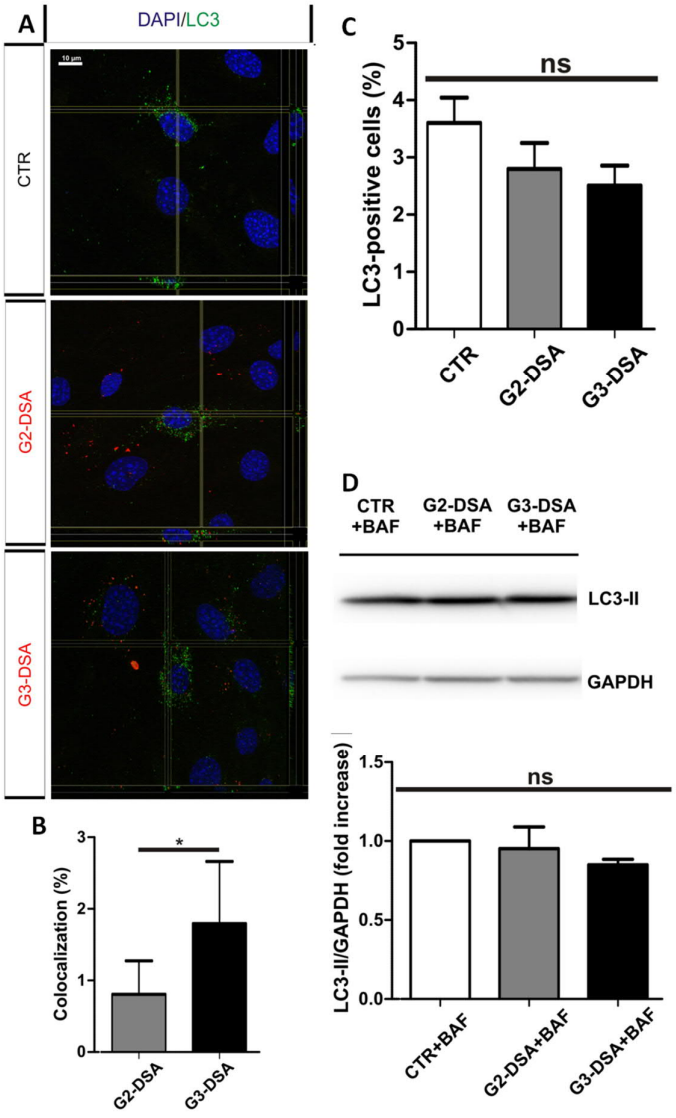

Figure 15. Effect of DSA on autophagy in bEnd.3 cells. (A) Representative confocal tridimensional orthogonal view for colocalization analysis of DSA-positive vesicles (red) and microtubule-associated protein 1A/1B-light chain 3 (LC3; green). (B) Quantification of colocalization for DSA with autophagosomes. Data are expressed in percentage of DSA-positive-vesicles partially colocalizing for at least 40 % with autophagosome-vesicles. G2-DSA n = 20 ROIs, G3-DSA n = 17 ROIs from 3 cultures; Mann-Whitney U test, *p < 0.05. (C) Percentage of LC3-positive cells in CTR or DSA treated bEnd.3 cells. Total number of cells in each analyzed ROI represents 100%. n = 30 ROIs from 3 cultures; one-way ANOVA; ns = not significant. (D, E) Western blot of lysates (D) and bands densitometric quantification (E) of LC3-II levels in CTR and DSA-treated cells. Bafilomycin (BAF) was used as inhibitor of autophagosome-lysosome fusion.n = 3 cell lysates from 3 cultures; one-way ANOVA; ns = not significant.

Autophagy can lead to contrary cellular fates because it is involved in both beneficial and harmful cellular effects (Cherra and Chu 2008, Codogno and Meijer 2005). While autophagy is activated at basal level in most of the cells in the body with a role in regulating the turnover of long-lived proteins and eliminating damaged structures, high levels of autophagy are often an indication of cellular stress. In order to address the question of whether DSA treatment might affect cellular homeostasis, induction of autophagy in bEnd.3 cells was monitored using immunocytochemical and biochemical approaches. First, comparing the ratio LC3-positive-cells/total number of cells in control culture and NP-treated samples, no DSA-mediated induction of autophagy could be demonstratedDSA (CTR: 3.6 ± 0.44 %; G2-DSA: 2.8 ± 0.45 %; G3-DSA: 2.5 ± 0.35 %, n = 30 regions of interest from 3 cultures, one-way ANOVA, P = 0.1657) (Figure 15C). Additionally, LC3-II levels can be analyzed to define activation of authopagic process, due to the fact that LC3-II correlates with autophagosome numbers (Loos et al. 2014, Tanida et al. 2008). To analyze the autophagic flux, the measurement of the LC3-II levels as a function of GAPDH (loading control) was compared by WB. Bafilomycin A1 was used to inhibit autophagosome-lysosome fusion to determine the activity of autophagic flux (Mauvezin and Neufeld 2015, Yang et al. 2013). No increase in LC3-II levels was observed in bEnd.3 treated with DSA for 24 h (CTR + BAF: 1; G2-DSA + BAF: 0.95 ± 0.14; G3-DSA + BAF: 0.85 ± 0.03, n = 3 from 3 cultures, one-way ANOVA, P = 0.4630) (Figure 15D). Taken together, these data indicate no increase of autophagy in DSA-treated cells with no incidence on the ratio of pro-survival/pro-death inputs.

The data presented so far demonstrated the transport of DSA by transcytosis. It has to be considered that material taken up from extracellular space by endocytosis often is delivered to lysosomes and there degraded by acid hydrolases. In order to study, if DSA might be temporarily delivered to lysosomes and partly degraded, I detected DSA by WB analysis in cell lysates after blocking the process of endosomes-lysosome fusion with BAF (4 h and 24 h treatment). I did not observe any change in levels of DSA uptake comparing BAF-treated samples with untreated ones (G2-DSA: 1, G2-DSA+BAF 4 h: 1.04 ± 0.18, G3-DSA: 1, G3-DSA+BAF 4 h: 0.97 ± 0.06, G3-DSA+BAF 24 h: 1.02 ± 0.01, n = 3 from 3 cultures, one-way ANOVA, P = 0.9826) (Figure 16A, B). In conclusion, the intracellular colocalization data presented herein

confirm a transcytosis transport which preserves DSA integrity and might involve lysosomal escape.

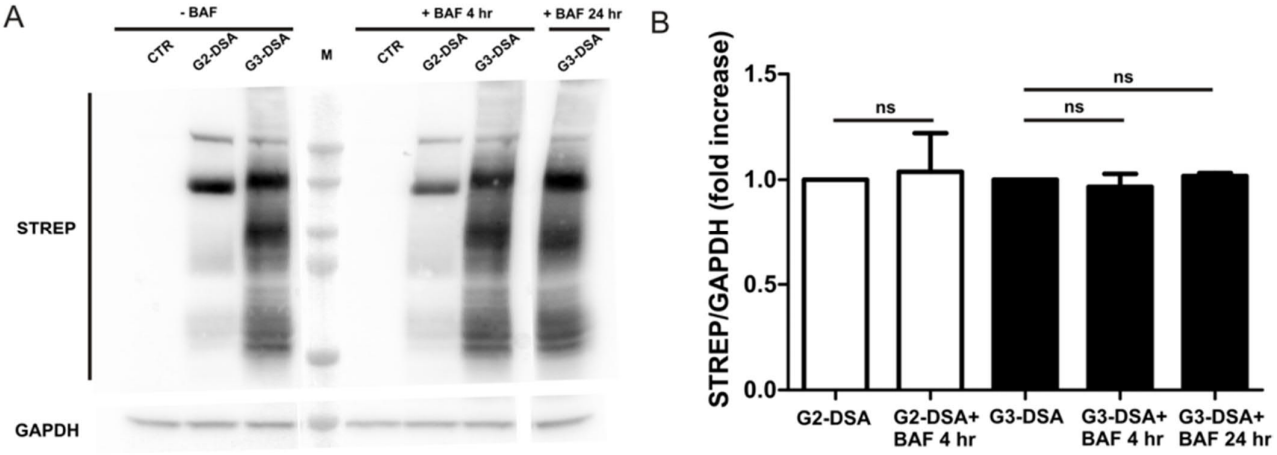

Figure 16. DSA lysosomal degradation. (A) Streptavidin (STREP) immunoblotting of lysate from CTR and DSA treated bEnd.3 cells. Bafilomycin (BAF) treatment for 4 h or 24 h was used to induce lysosomal escape of DSA. (B) Densitometric quantification of STREP levels for DSA-treated cells with or without BAF treatment. STREP levels of not BAF-treated samples were set to 1 and each correspondent BAF-treatment expressed as relative value; n = 3 cell lysates from 3 cultures; one-way ANOVA; ns = not significant.

4.1.4 DSA do not affect bEnd.3 cells vitality and BBB integrity

The ability of DSA to be taken up by endothelial cells and transported across BBB has been assessed. The biocompatibility is another parameter that has to be evaluated for NPs which are validated to be used in therapeutic approaches.

Indeed, the nanosystem presented here aims to target the brain without disruption or opening of the BBB and without affecting cell viability. Cell viability was challenged for 24 h with rising concentration of DSA (from 10 to 400 µg mL^{-1}) considering that the applied concentration for uptake and transport studies was 45 µg mL^{-1}. Cell vitality quantified by reduction of the alamar blue viability reagent showed no toxicity of the DSA for all concentrations (n > 9 wells from 4 cultures; one-way ANOVA; P > 0.05). On the contrary, CTR and serial dilutions of DSA showed high significant differences with the staurosporine probe used as toxic control (live:

99.8 ± 0.75 % vs. dead: 1.81 ± 1.37 %, n > 9 wells from 4 cultures, one-way ANOVA, P < 0.05) (Figure 17A).

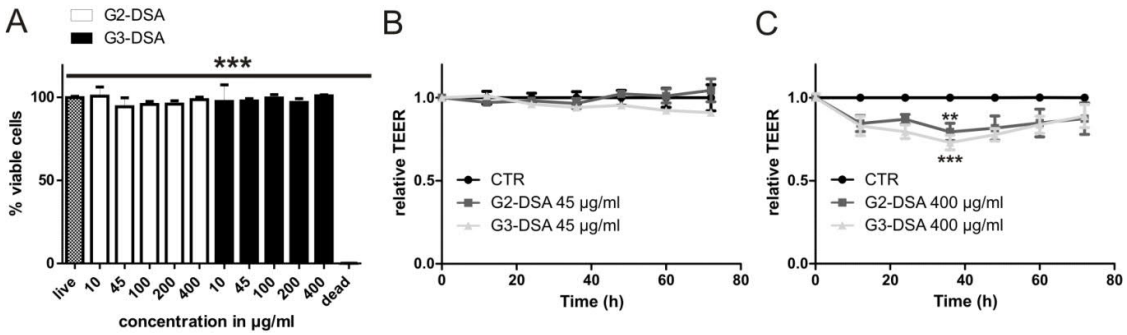

Figure 17 DSA effect on cell vitality and BBB integrity in vitro. (A) bEnd.3 cell vitality by Alamar Blue assay after DSA treatment (24 h). Positive control: cell toxin staurosporine. n > 9 wells from 4 cultures; one-way ANOVA; ***p < 0.001. (B, C) Long term impact of DSA on cell integrity investigated for 72 h by ECIS. TEER values at t = 0 (DSA treatment) and TEER from CTR measurement were set to 1 and each measurement is expressed as a relative value. n (45 µg mL^{-1}) = 5 wells from 2 cultures; n (400 µg mL^{-1}) = 7 wells from 3 cultures, two-way ANOVA, ***p < 0.001, **p < 0.01.

Next, a concentration-dependent impact of DSA on BBB integrity was probed. For this purpose, cells were seeded in an ECIS 8-Well chamber and TEER was measured continuously for up to 72 h after DSA application. The DSA concentration used in the previously discussed experiments (45 µg mL^{-1}) showed no significant impact on the barrier integrity (n = 5 wells from 2 cultures, two-way ANOVA, P > 0.05) (Figure 15B), while high concentrations of DSA (400 µg mL^{-1}) have a low reversible impact on barrier integrity (Figure 17C). TEER values dropped to 79 % for G2-DSA (n = 7 wells from 3 cultures, two-way ANOVA, P < 0.01) and 73 % for G3-DSA (n = 7 wells from 3 cultures, two-way ANOVA, P < 0.001) within the first 40 h. However, barrier integrity recovered to 87 % for G2-DSA (n = 7 wells from 3 cultures, two-way ANOVA, P > 0.05) and to 89 % for G3-DSA (n = 7 wells from 3 cultures, two-way ANOVA, P > 0.05) at 72 h during DSA application. Additionally, Zona occludens 1 (ZO1) staining as marker of tight junctions also show maintenance of intact tight monolayer in bEnd.3 cells treated for 24 h with DSA (45 µg mL^{-1}) (Figure 18). Thus, DSA represent a good biocompatible system which do not dramatically affect both cell viability and BBB integrity.

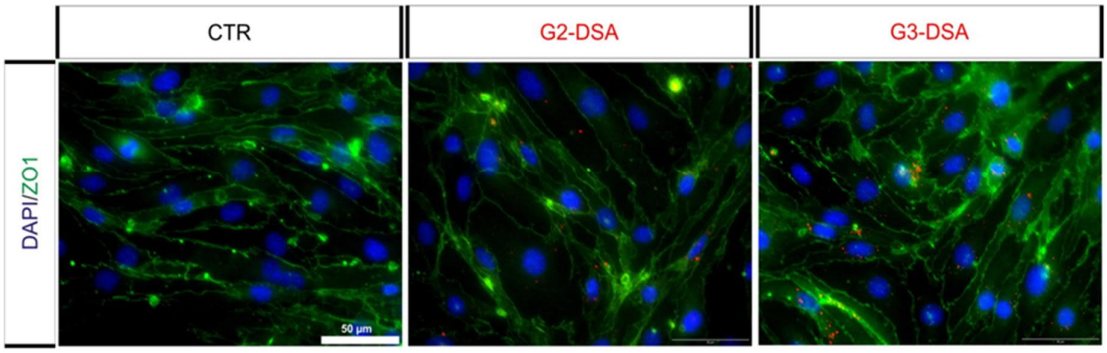

Figure 18. DSA effect on bEnd.3 monolayer. Representative epifluorescence microscopy images from bEnd.3 cells culture treated with DSA (red) showing maintenance of BBB integrity by tight junctions staining with zona occludens 1 marker (ZO1; green).

4.1.5 DSA uptake in astrocytes and neurons occurs without cytotoxic effects

The aim for a successful brain treatment is not only to overcome the BBB, but also to reach target cells. These target cells in CNS diseases might be neurons or astrocytes. To investigate the potential of DSA to target NVU cells, primary cells were treated for 24 h, fixed and co-stained with markers for astrocytes (GFAP) and neurons (ß-III-tubulin). High rate of uptake could be observed for both generations of DSA in glial cells (Figure 19A) which represent the cell type coming in close contact with the tight layer of endothelial cells in BBB. In co-culture of neurons and astrocytes, ß-III-tubulin stainings revealed uptake also in neuronal cells both in cell body and in dendrites as shown by colocalization of NP-containing vesicles (Figure 19B).

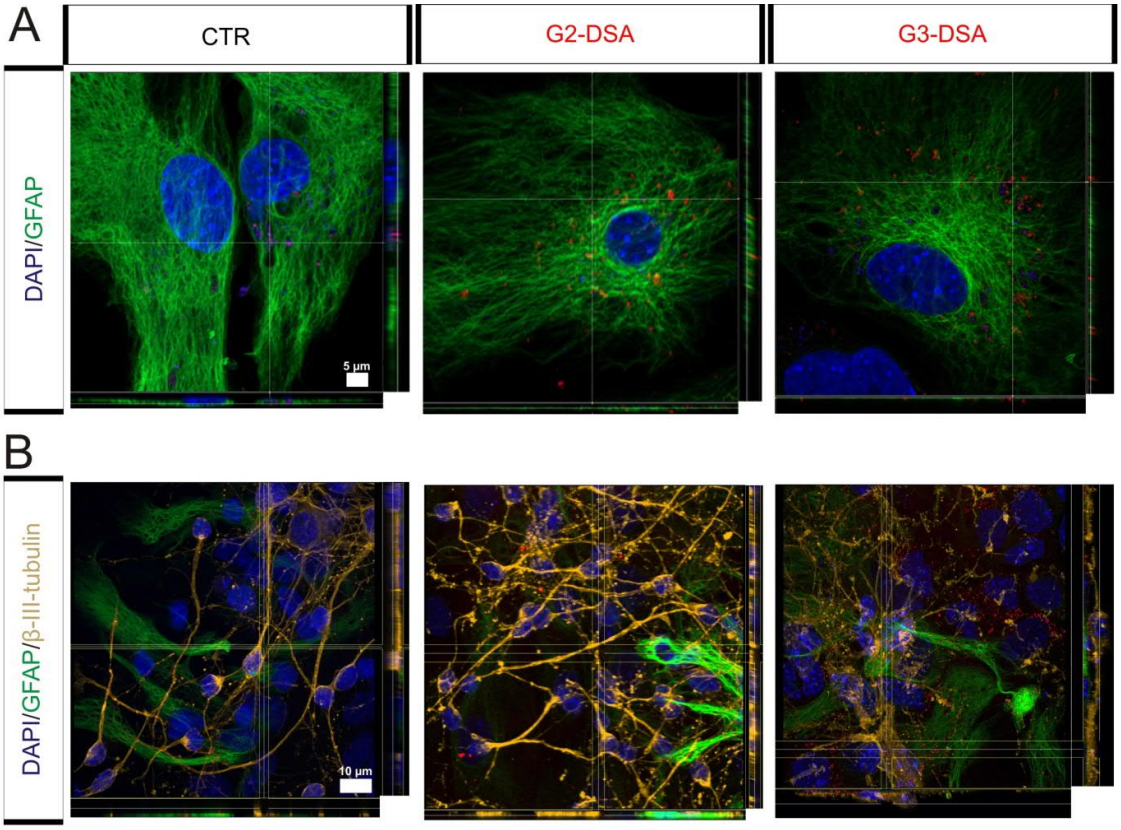

Figure 19. DSA uptake in target cells. (A, B) Representative confocal tri-dimensional orthogonal views of DSA (red) uptake in GFAP-positive primary murine astrocytes (green) (A) and β-tubulin-positive primary murine neurons (orange) (B).

As already observed for bEnd.3 cells, G3-DSA showed higher uptake properties than G2-DSA in all NVU cells. In addition, these data confirmed the previously mentioned hypothesis that lower G3-DSA transport values in triple co-culture system (Fig 11D) may result from a high uptake in target cells located in the abluminal compartment. For validation of nanoparticles for brain delivery it has to be taken into account that delivery of exogenous molecules into the brain parenchyma might cause side effects. Hence, in order to evaluate whether DSA affect cell viability of target cells, the alamar blue assay for primary murine astrocytes and the TUNEL assay for neurons were carried out, applying rising concentrations of DSA from 10 up to 400 µg mL^{-1}. After 24 h treatment, alamar blue assay showed no changes in astrocyte cell vitality for all analyzed concentrations, even for DSA concentration up to 400 µg mL^{-1} ($n > 9$ from 3 cultures, one-way ANOVA, $P > 0.05$) and significant differences were observed in comparison with a cytotoxic staurosporine treatment (live: 100.34

± 1.4 % vs. dead: 0.5 ± 0.49 %, n > 9 from 3 cultures, one-way ANOVA, P < 0.05) (Figure 20A). Comparable results were obtained for primary neuronal cultures by TUNEL assay. There was no significant increase in apoptotic rate for DSA treated neurons (n > 9 from 3 cultures, one-way ANOVA, P > 0.05) (Figure 20B), but a significant increase could be observed for the dead control treated with staurosporine (live: 1 ± 0.03 vs. dead: 2.3 ± 0.14, n > 9 from 3 cultures, one-way ANOVA, P < 0.05). These data revealed the ability of DSA to penetrate the NVU cells without induced cytotoxic effects.

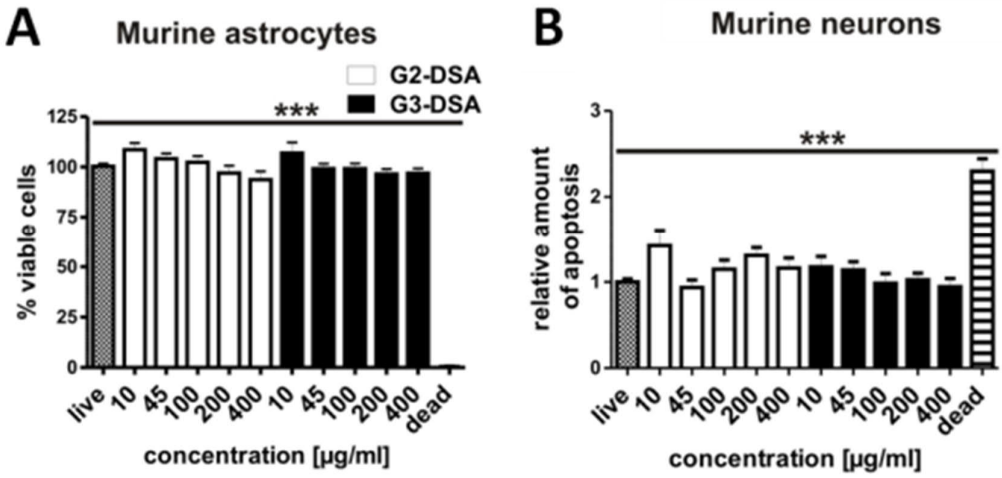

Figure 20. DSA cytotoxicity in target cells. (A, B) Cell vitality after DSA treatment (24 h) in primary murine astrocytes quantified by Alamar Blue assay (A) or in primary murine neurons by Fluorometric TUNEL assay (B). Positive control (dead): cell toxin staurosporine. primary murine astrocytes: n > 9 from 3 cultures; primary murine neurons: n > 9 wells from 3 cultures; one-way ANOVA; ***p < 0.001.

4.1.6 DSA are transported to the brain and taken up by NVU cells in vivo

Uptake and transport assays in vitro proved that G3-DSA is more promising for further applications since the higher uptake in cells suggests higher efficiency in penetrating endothelial cells, crossing the BBB and more easily reaching target cells. For this reason, in vivo studies were focused on G3-DSA to reach CNS after tail intravenous injection in mice. Coronal slices of 30 µm from brains isolated by CTR or Cy5-labeled-G3-DSA treated mice were carefully analyzed and screened for DSA specific signal.

Three main barrier layers are considered to separate the blood and the CNS: the endothelium of the brain microvessels, the epithelium of the choroid plexus, and the epithelium of the arachnoid mater (Abbott 2014). Uptake of G3-DSA was easily detectable in cells surrounding blood vessels (Figure 21A).

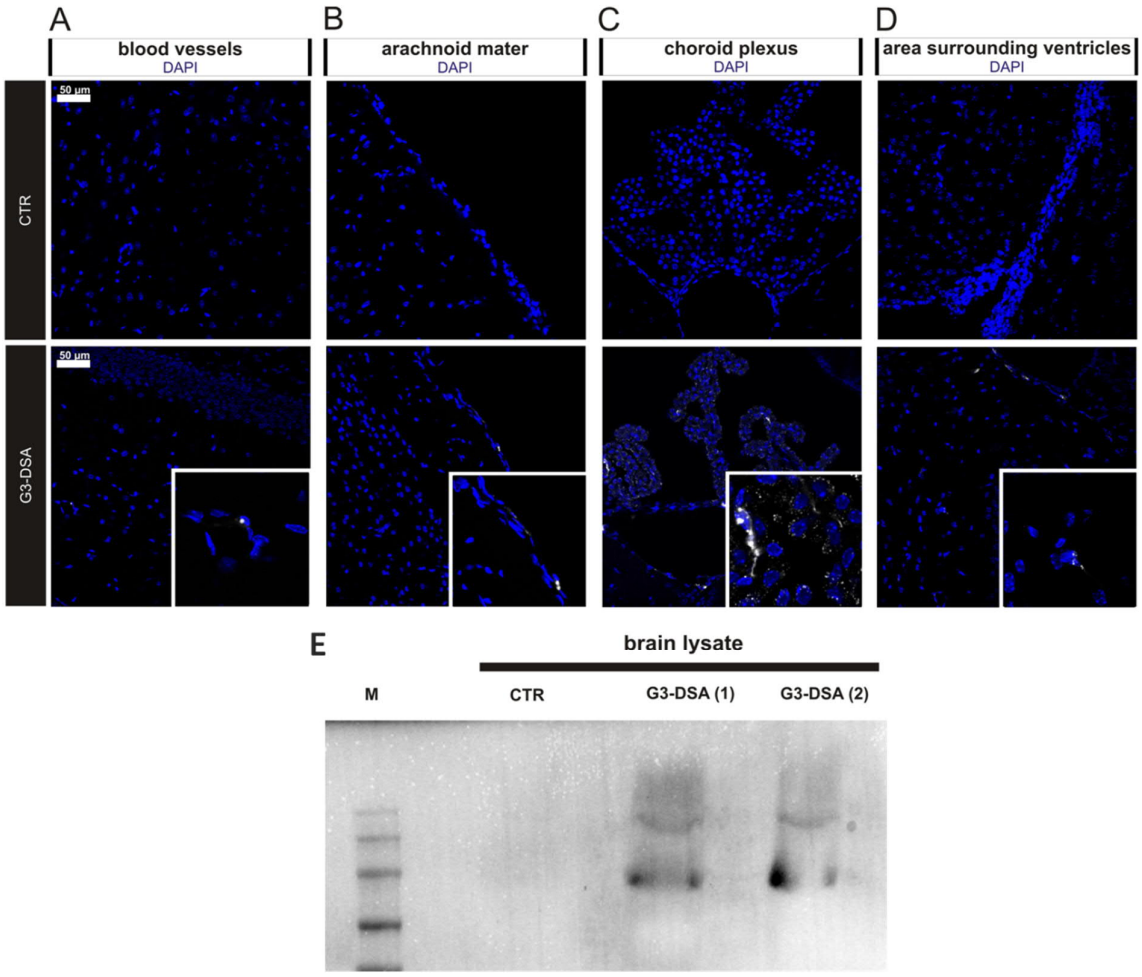

Figure 21. In vivo G3-DSA brain transport in mice. (A-D) Representative confocal images of G3-DSA (white) uptake at blood-brain barriers and periventricular area 24 hours after intravenous injection (450 µg mL^{-1} blood). (E) Streptavidin immunoblotting of brain lysate from CTR and 2 x G3-DSA treated mice (450 µg mL^{-1}) 24 h post intravenous injection.

G3-DSA were also clearly taken up in meninges in correspondence of the second barrier layer represented by the epithelium of the arachnoid mater (Figure 21B). However, highest uptake was observed in choroid plexus and ventricles, suggesting that G3-DSA were released into the cerebrospinal fluid as well (Figure 21C, D). These

three barriers represent the ways our nanocarriers can take to the brain. Uptake of G3-DSA into the brain was also confirmed by WB analysis on brain lysate. On PVDF membrane, clear bands for DSA were visible after detection of streptavidin core (Figure 21E). To more specifically identify the localization of nanocarriers within the brain tissue, G3-DSA signal was detected in combination with staining for endothelial cells using the marker endoglin (CD105), glia using the marker glial fibrillary acidic protein (GFAP), or neurons using the marker NeuN. CD105 staining clearly showed G3-DSA uptake on the lumen side of the vessels as well as in the abluminal brain parenchyma (Figure 22A). Lower intensity DSA signals were detected also in target cells: astrocytes (Figure 22B) and neurons (Figure 22C).

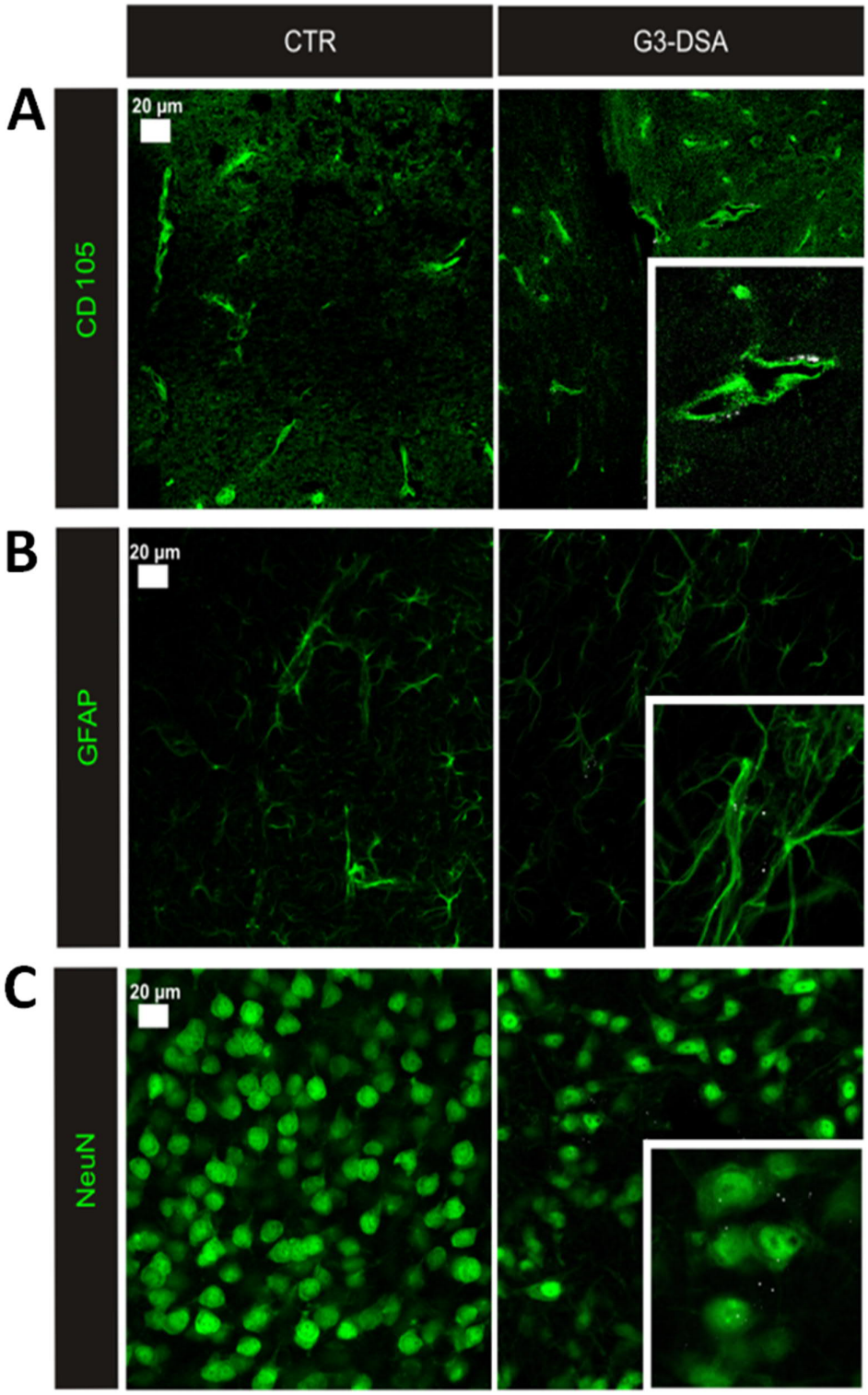

Figure 22. In vivo G3-DSA uptake in NVU cells in mice. (A-C) Representative confocal images of G3-DSA (white) uptake in brain endothelial cells (CD105; green) (A), astrocytes (GFAP; green) (B) and neurons (NeuN; green) (C) 24 h after intravenous injection (900 µg mL^{-1}).

4.1.7 DSA reach also peripheral organs in vivo after intravenous injection

Although this study aims to investigate DSA transport to the brain, additionally the uptake of G3-DSA in other organs was investigated. Therefore, after each NP application, kidney, liver, spleen, lung and heart were also collected and screened for NPs uptake. NPs signal was detected in spleen, lung and heart with low uptake rates (Figure 23A, B, C). However, G3-DSA showed high uptake rates in kidney and liver (Figure 23D, E).

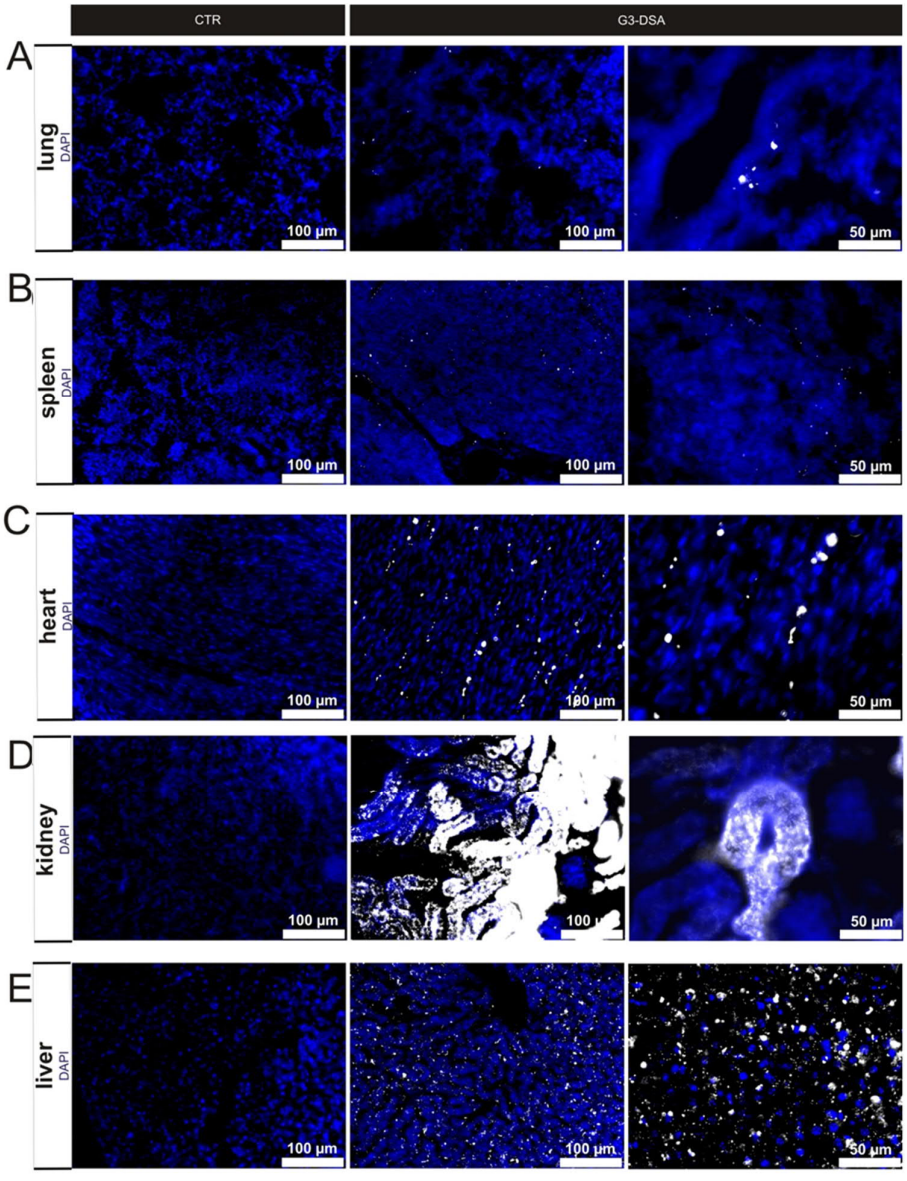

Figure 23. In vivo G3-DSA biodistribution in mice. (A-E) G3-DSA (white) uptake in different organs (kidney (D), liver (E), lung (A), spleen (B), heart (C)) 24 h after intravenous injection (450 µg mL^{-1}).

The present data demonstrate high kidney uptake of DSA, which could indicate a high rate of clearance or renal reabsorption. To further investigate the case for DSA, WB analysis on blood samples collected 24 h after G3-DSA treatment revealed a circulation of the nanocompound indicating that NPs were still available for uptake (Figure 24).

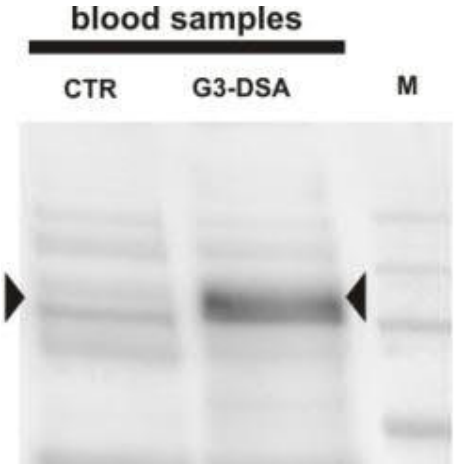

Figure 24. G3-DSA permanence in blood after 24 h from iv. application in mice. Streptavidin immunoblotting of blood samples from CTR and G3-DSA treated mice (450 µg mL^{-1}) 24 h post intravenous injection. On PVDF membrane several not specific bands are detectable due to the presence of endogenous antibodies in blood samples. Arrow head: specific band for G3-DSA.

4.1.8 DSA do not affect BBB integrity in vivo

To assess the use of DSA for medical applications, the BBB integrity was studied by the use of intravital dyes (tracers, markers) of molecular weight greater than 180 Da, which preclude passage across an intact barrier. Evans blue (EB) (MW 961 Da) is one of the largest dyes, which in blood binds to the albumin fraction (EBA) to give rise to a high-molecular complex (EBA = 68,500 Da) (Kozler and Pokorný 2003). EB was intravenously injected 3 h before the end of DSA treatment to assess BBB integrity. The analysis of the brains did not show macroscopically EB infiltration in brain tissue related to DSA treatment (Figure 25A). Epifluorescence microscopy revealed a localized EB fluorescence in blood vessels without extravasation of the dye in both Sham and G3-treated animals (Figure 25B). In addition, analysis of brain lysate did not show significant change of EB fluorescence compared to the sham animal measuring the µg of EB g^{-1} of brain tissue (Sham: 0.17 ± 0.03 µg g^{-1} of brain tissue vs. G3-DSA: 0.19 ± 0.02 µg g^{-1} of brain tissue, n = 3 brain lysates from 3 mice, Mann-Whitney U test, P = 0.6905) (Figure 25C). This data exclude a correlation between in vivo G3-DSA uptake and BBB disruption and proves the biocompatibility of our protein nanocarriers.

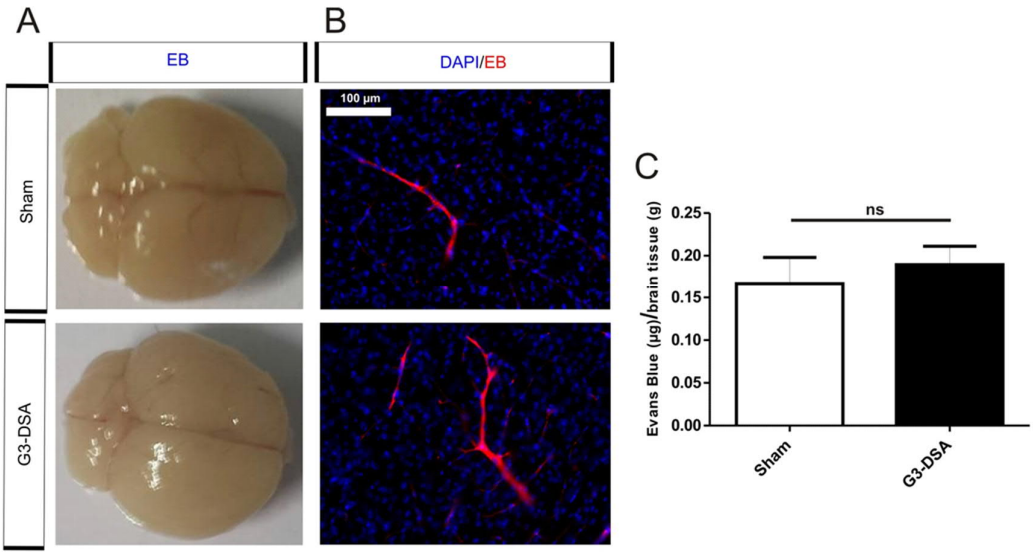

Figure 25. In vivo G3-DSA effect on BBB integrity in mice. (A) Representative pictures of intact brains showing absence of Evans Blue (EB) extravasation in sham as well as G3-DSA-treated mice after 24 h from the injection. (B) Representative epifluorescence microscopy images from brain slices showing presence of EB (red) in blood vessels without permeation in brain parenchyma in sham and G3-DSA-treated mice. (C) EB quantification in brain lysate from sham and G3-DSA-treated mice. Data are expressed as µg of EB per g of brain tissue. n = 3 brain lysates from 3 mice; Mann-Whitney U test; ns = not significant.

4.2 Fluorescent Nanodiamonds as nanotheranostics platform for brain drug delivery via crossing an intact BBB

4.2.1 dcHSA-fNDs are taken up by brain endothelial cells in vitro

To assess the transport of dcHSA-fNDs into the brain, at first in vitro studies were carried out in order to understand whether the investigated nanocompound was able to penetrate the first cell layer composing the BBB: the endothelium of the microvessels.

bEnd.3 cells as brain endothelial cell lines were screened for dcHSA-fNDs-rhodamine signal by confocal microscopy after 24 h of dcHSA-fNDs treatment. Orthogonal view and 3D-reconstruction from deconvolved z-stacks showed dcHSA-fNDs fluorescence in the cell cytosol as dcHSA-fNDs-containing-vesicles (Figure 26).

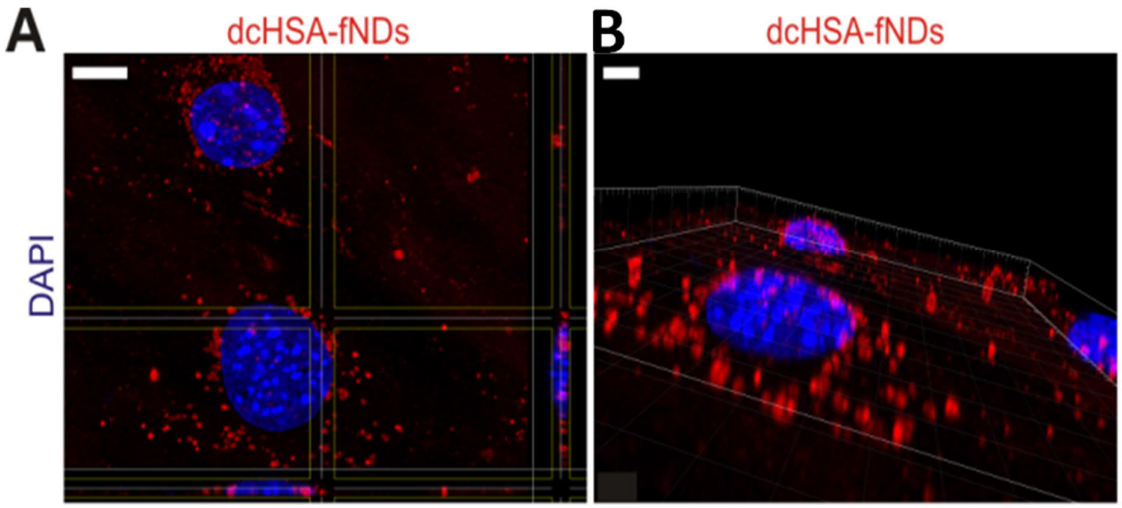

Figure 26. dcHSA-fNDs uptake in bEnd.3. (A-B) Representative confocal orthogonal view (A) and 3D-reconstruction of dcHSA-fNDs (red) uptake (B); cell nuclei were stained with DAPI; scale bar = 5 µm

Additionally, a comparison carried out on the different signals obtainable from dcHSA-fNDs (internal reflection fluorescence, inner fluorescence and shell fluorescence) demonstrated that reflection, bodipy488-labeled-dcHSA-shell and NV

signals were all detectable and colocalizing (Figure 27) demonstrating the maintenance of integrity and inner properties in the biological environment.

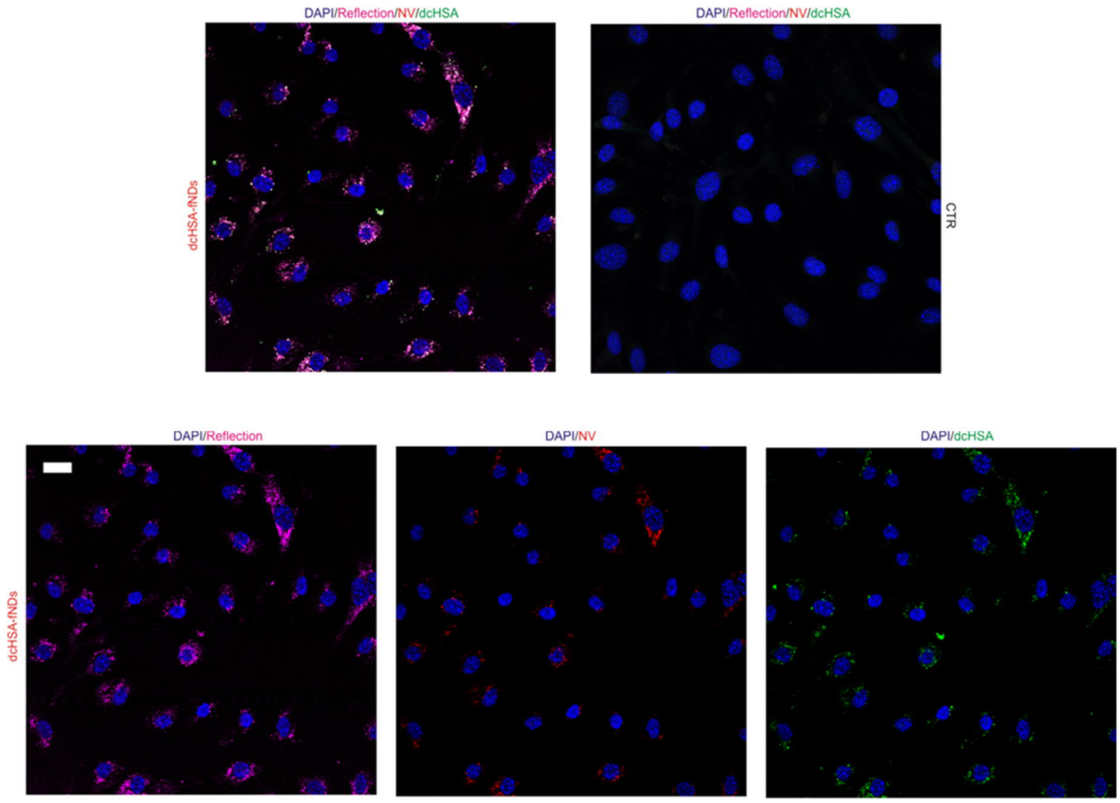

Figure 27. dcHSA-fNDs detectable colocalizing signals. Representative confocal picture of reflection (magenta), NV (red), dcHSA-shell (green) signals for dcHSA-fNDs in bEnd.3 cells; scale bar = 20 µm.

Additionally, bEnd.3 cells were treated for 24 h with dcHSA-fNDs in combination with FITC-transferrin (TF) or the B subunit of cholera toxin-alexa-488 (CTX) to identify the endocytosis mechanism. dcHSA-fNDs colocalized for 27.7 ± 3.07 % with TF and 70.55 ± 3.9 % with CTX showing a significantly higher preference for caveolae-mediated endocytosis (TF vs CTX: n = 12 regions of interest from 3 cultures, Mann-Whitney U test, $P < 0.0001$) (Figure 28A,B).

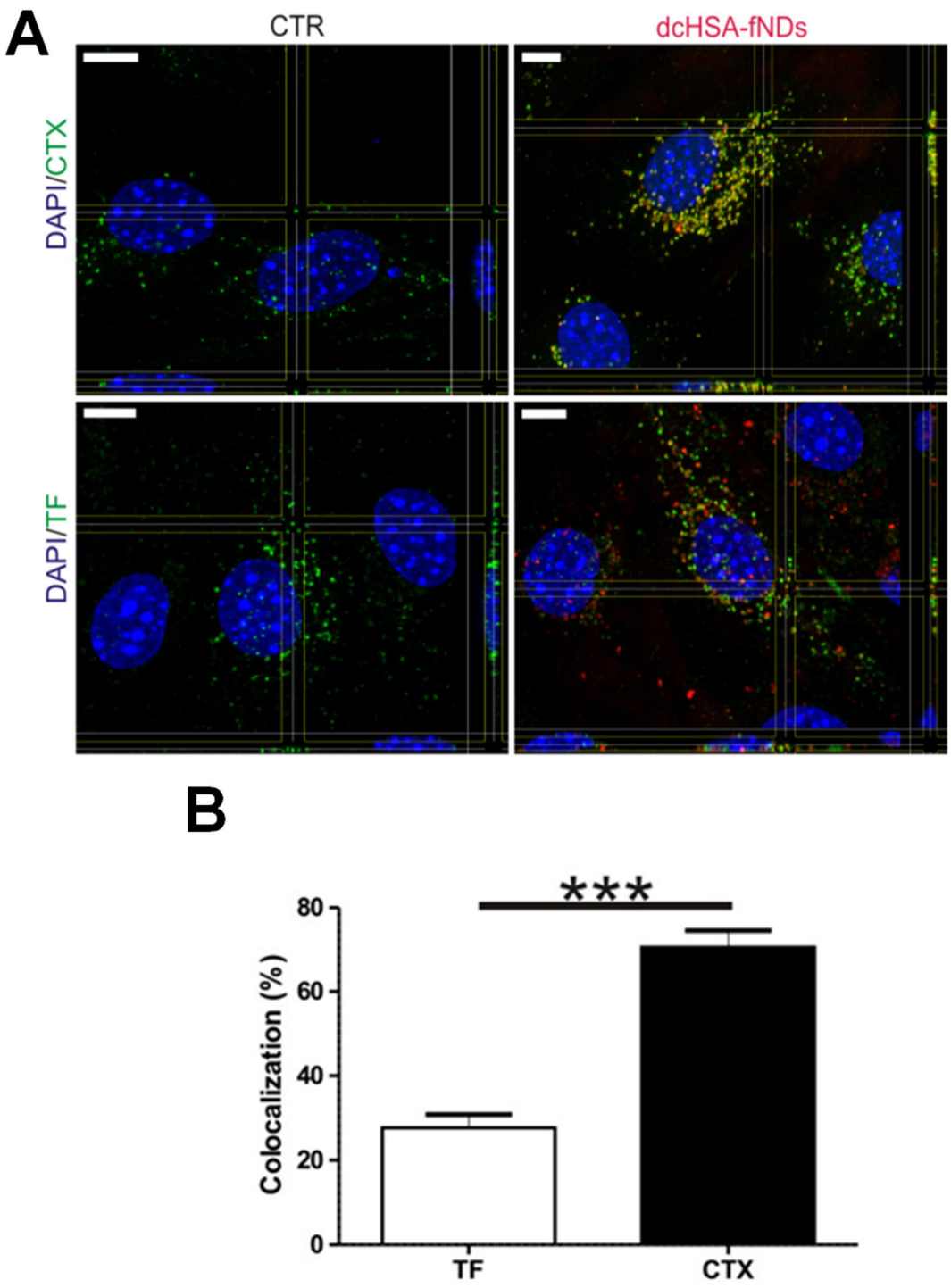

Figure 28. dcHSA-fNDs uptake mechanism in bEnd.3. (A) Representative confocal orthogonal view and 3D-reconstruction of dcHSA-fNDs colocalization with CTX or TF (green); scale bar = 5 µm. (B) Percentage of colocalizing dcHSA-fNDs-containing-vesicles with CTX or TF –containing vesicles; n = 12 ROIs from 3 cultures, Mann-Whitney U test, ***$p < 0.001$.

4.2.2 dcHSA-fNDs are transported across BBB in vitro in a size-independent manner

In order to investigate the ability of dcHSA-fNDs to cross the BBB we used an in vitro model composed by bEnd.3 cells as endothelial cell line seeded on the luminal side of a transwell insert. 30 µg mL^{-1} of 40 nm or 60 nm dcHSA-fNDs were applied in luminal compartment of the transwell BBB model in order to assess their ability to be transported from one side to the other and whether the size contributes considerably to the migration process. After 24 h treatment dcHSA-fNDs fluorescence was measured in collected abluminal medium to estimate the transport rate. The percentage of transport was 45.17 ± 7 % (n = 6 wells from 3 cultures) for 40 nm dcHSA-fNDs and 38.6 ± 7.6 % (n = 6 wells from 3 cultures) for 60 nm dcHSA-fNDs compared to the 100 % (100 % dcHSA-fNDs 40nm: 100 ± 5.4 %; 100 % dcHSA-fNDs 60nm: 100 ± 3 %; n > 6 wells from 3 cultures) of transport with no significant size dependent difference (one-way ANOVA, $P < 0.0001$) (Figure 29A). The data indicate that dcHSA-fNDs are capable to efficiently cross BBB in vitro. Size-independent transport is the reason why further experiments have been carried out using a mixture of 40-60 nm dcHSA-fNDs for which transport efficiency was additionally confirmed as shown in Figure 29B. The choice of a size mixture referred also to the preference of reducing purification steps in order to simplify the dcHSA-fNDs production process decreasing the possible impact of purification reagents on biocompatibility and the time of synthesis.

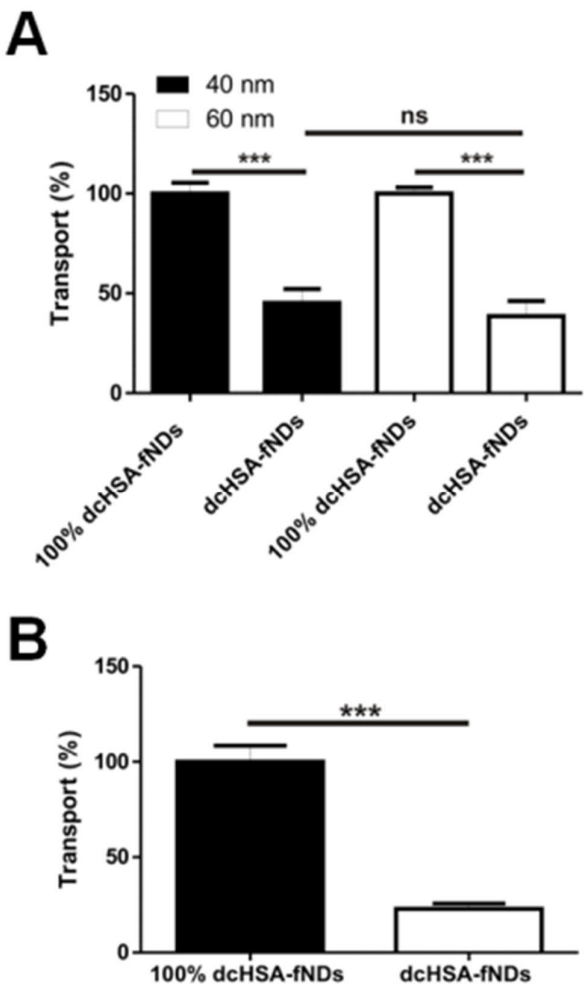

Figure 29. dcHSA-fNDs transport across BBB in vitro. A) Mean relative transport for 40 nm or 60 nm dcHSA-fNDs (A) or 40-60 mixture dcHSA-fNDs (B) across bEnd.3 cells monolayer. At time = 0 h of transport assay dcHSA-fNDs were applied at a concentration of 30 µg mL-1 for 24 h. Abluminal fluorescence is expressed as relative values compared to the 100 % of dcHSA-fNDs transport in inserts without cells (100% dcHSA-fNDs); n ≥ 6 wells from 3 cultures, one-way ANOVA, ***p < 0.001, ns = not significant.

4.2.3 dcHSA-fNDs transport employs transcytosis involving endosomal localization

The initial intracellular pathway of a vesicle upon internalization is the same whether it is internalized via clathrin-mediated or caveolae-mediated endocytosis

and begins with the early endosomes (EE). Without selective retrieval, the material located in EE mostly will be delivered to late endosomes (LE) and lysosomes. In order to understand whether dcHSA-fNDs were located in EE or LE/lysosomes, bEnd.3 cells were fixed after 24 h of treatment and using immunocytochemistry, EE and LE were stained. Orthogonal view from z-stacks obtained by confocal microscopy revealed dcHSA-fNDs-containing-vesicles localizing with EE and LE/lysosomes (Figure 30A).

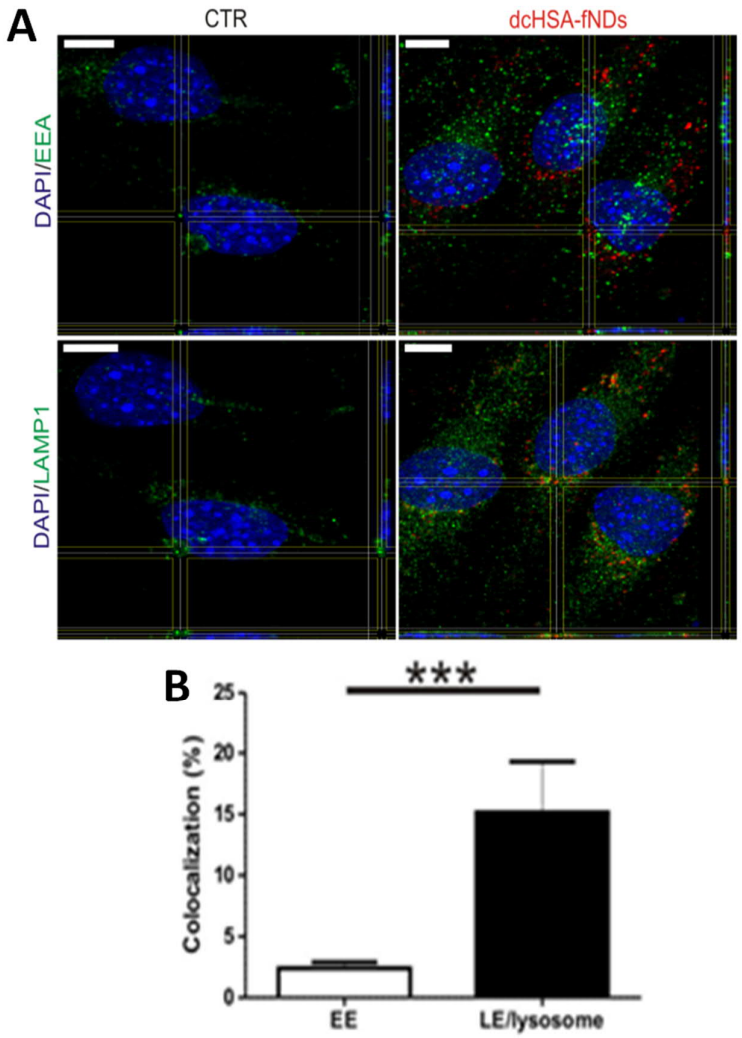

Figure 30. dcHSA-fNDs endosomal compartments localization in bEnd.3 cells. (A) Representative confocal orthogonal view and 3D-reconstruction of dcHSA-fNDs (red) colocalization with EE or LE/lysosome (green); scale bar = 7 µm. (B) Quantification of colocalization for dcHSA-fNDs-containing vesicles with early endosomes or late endosomes; n = 12 ROIs from 3 cultures, Mann-Whitney U test, ***$p < 0.001$.

Quantitative analysis showed a colocalization of 2.4 ± 0.5 % with EE and 15.14 ± 4.15 % with LE/lysosomes (n = 12 regions of interest from 3 cultures, Mann-Whitney U test, P < 0.0001) (Figure 30B). Concerning the intracellular fate of dcHSA-fNDs another possibility would have been the induction of autophagy with subsequent internalization of dcHSA-fNDs in autophagosomes. Therefore, dcHSA-fNDs signal was detected in combination with staining for autophagosomes using LC3. Representative orthogonal z-stacks showed LC3-positive vesicles in both CTR and dcHSA-fNDs treated cultures (Figure 31A). Indeed, it was already described in literature that endothelial cells show high basal autophagy. Very few dcHSA-fNDs-containing vesicles might be identified as autophagosomes. This assumption was clearly confirmed by quantification of colocalization rate of dcHSA-fNDs signal with LC3 signal. dcHSA-fNDs colocalize with a percentage of 0.98 ± 0.52 % (n = 10 regions of interest from 3 cultures) with LC3-positive-vesicles that represents a negligible value considering the high rate of basal autophagy (Figure 31B).

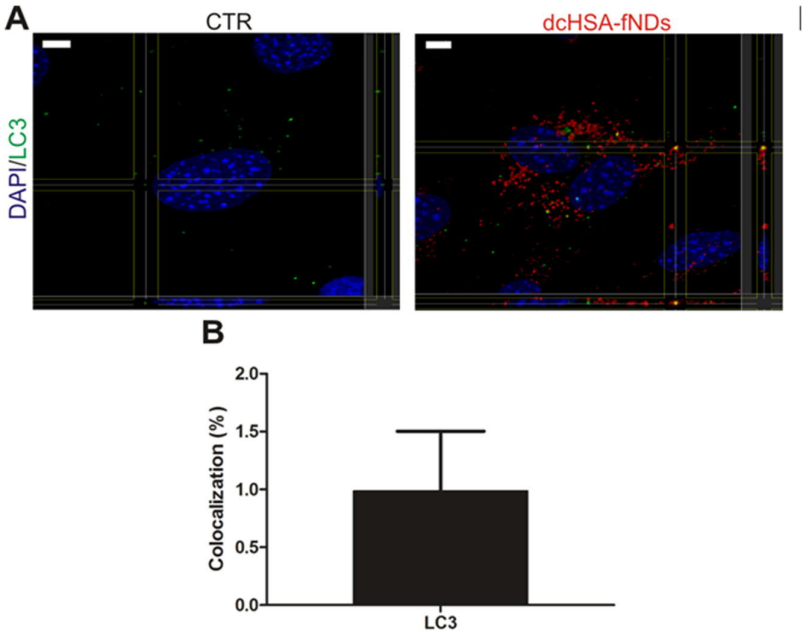

Figure 31. dcHSA-fNDs autophagosomal localization in bEnd.3 cells. (A) Representative confocal orthogonal view of dcHSA-fNDs (red) colocalization with LC3 (green); scale bar = 5 µm. (B) Percentage of colocalizing dcHSA-fNDs with LC3; n = 10 ROIs from 3 cultures.

Taken together this data suggest intracellular trafficking involving endosomes that lead to transcytosis of dcHSA-fNDs from luminal to abluminal side with no involvement and induction of autophagy mechanisms.

4.2.4 dcHSA-fNDs are taken up by astrocytes and neurons in vitro

After transcytosis dcHSA-fNDs reach the abluminal compartment. In physiological condition after moving from the lumen of the blood vessel to the abluminal brain parenchyma, dcHSA-fNDs will get in contact with other cell types: mostly neurons and astrocytes. In order to assess the ability of dcHSA-fNDs to be delivered to neurons and astrocytes, we studied whether dcHSA-fNDs were taken up by target cells using immunocytochemistry on murine primary cultures. Astrocytes were stained with marker glial fibrillary acidic protein (GFAP) while neurons with the marker NeuN to visualize the cell body or β-III-tubulin for axons and dendrites. Orthogonal view from z-stacks of dcHSA-fNDs-treated-astrocytes showed high uptake predominantly in the perinuclear region (Figure 32A). However, in neurons, confocal microscopy revealed higher localization of dcHSA-fNDs in axons and dendrites as visible in β-III-tubulin staining than in perinuclear region as visible in NeuN staining (Figure 32B).

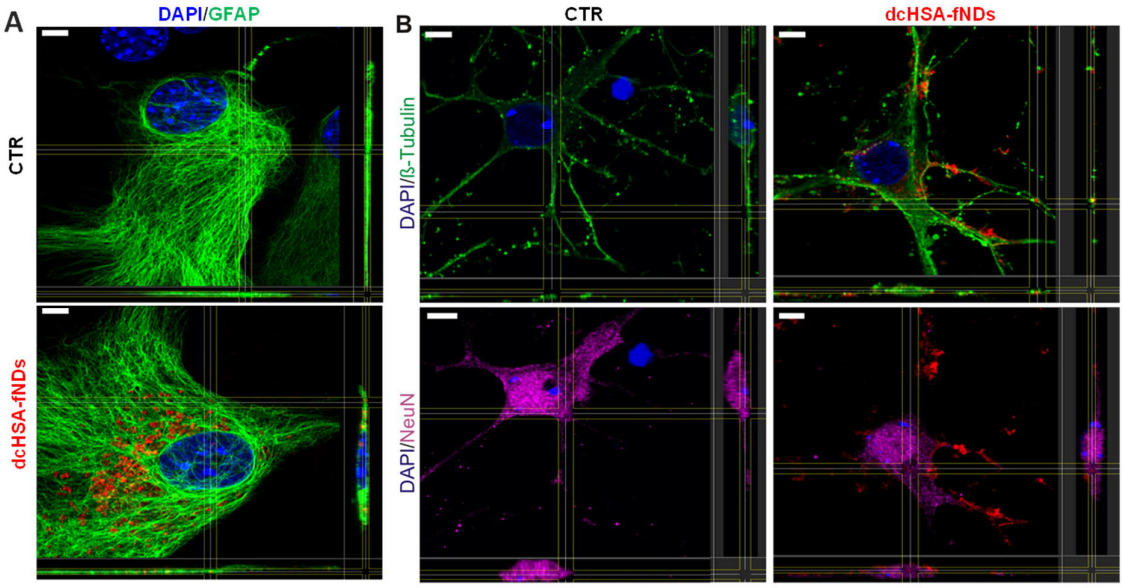

Figure 32. dcHSA-fNDs uptake in primary murine neurons and astrocytes in vitro. (A) Representative confocal orthogonal views of dcHSA-fNDs (red) uptake in astrocytes by GFAP marker (green) and perinuclear localization. (B) Neuronal uptake of dcHSA-fNDs in cell body stained by NeuN (magenta) and dendrites and axons stained by β-tubulin (green); scale bar = 5 µm.

4.2.5 dcHSA-fNDs show direct cell-cell migration mediated by actin bridges

The analysis of the dcHSA-fNDs uptake and localization pointed out that although many NPs-containing vesicles were localized in the perinuclear area especially in bEnd.3 cells and astrocytes, there was also a consistent distal localization that brought us to carry out further investigations. At first, rhodamine-phalloidin was used to stain bEnd.3 cells cytoskeleton in order to identify in which cell area distal localization was occurring. Intriguingly, dcHSA-fNDs-vesicles located in a cell structure connecting two adjacent cells (Figure 33). The identified actin bridges have been characterized as tunneling nanotubes (TNT) already observed in many cell types in vitro and in developing embryos of different species in vivo, representing thin membranous bridges connecting cells over long distances and transferring various cellular components from cell to cell (Gerdes, Rustom and Wang 2013).

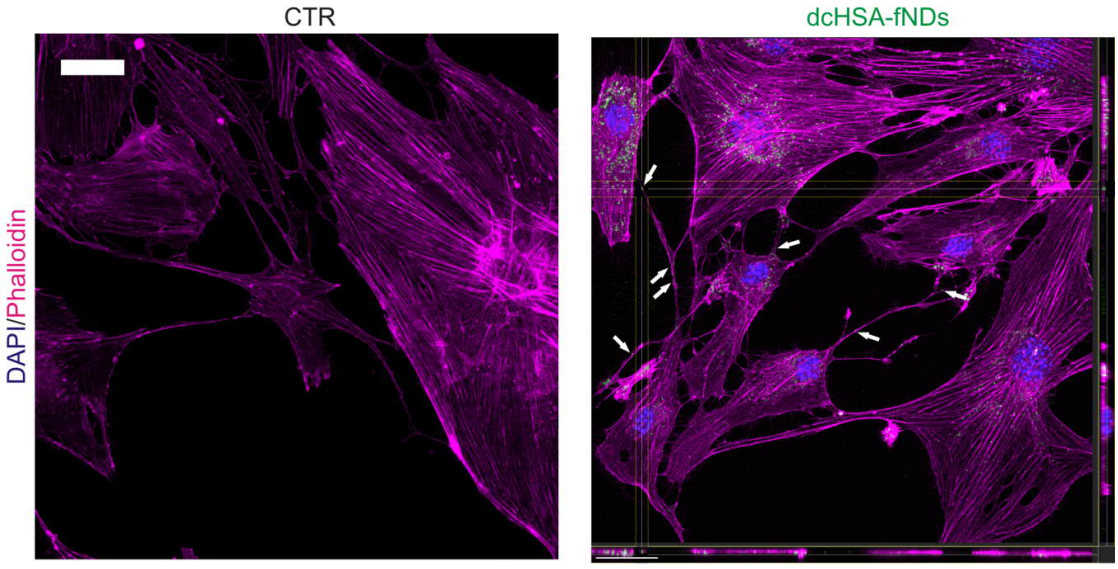

Figure 33. dcHSA-fNDs localization in actin bridges in bEnd.3 cells. Representative confocal orthogonal view of dcHSA-fNDs (green) localization in phalloidin-labeled-actin (magenta) bridges in bEnd.3 cells. White arrows indicate TNTs-colocalizing-particles. Scale bar = 20 µm.

Live cell imaging and time lapse have been carried out on bEnd.3 cells in order to have a closer view on the mechanism of direct cell-cell transport of dcHSA-fNDs along TNTs. Due to high contrast of dcHSA-fNDs in brightfield it was possible to observe dcHSA-fNDs-vesicles moving in TNTs (Figure 34). Fluorescent signal from dcHSA-fNDs made possible to ascribe the brightfield signal to dcHSA-fNDs. Additionally, combining fluorescence at time = 0 min, fluorescence at time = 45 min and brightfield picture at time = 0 allowed us to compare movements of different vesicles located in different positions along the same TNT (Figure 34). The data obtained by the time-lapse revealed a unidirectional migration from an initiating cell to a target cell and a faster movement while getting closer to the target cell (Figure 34; white arrows).

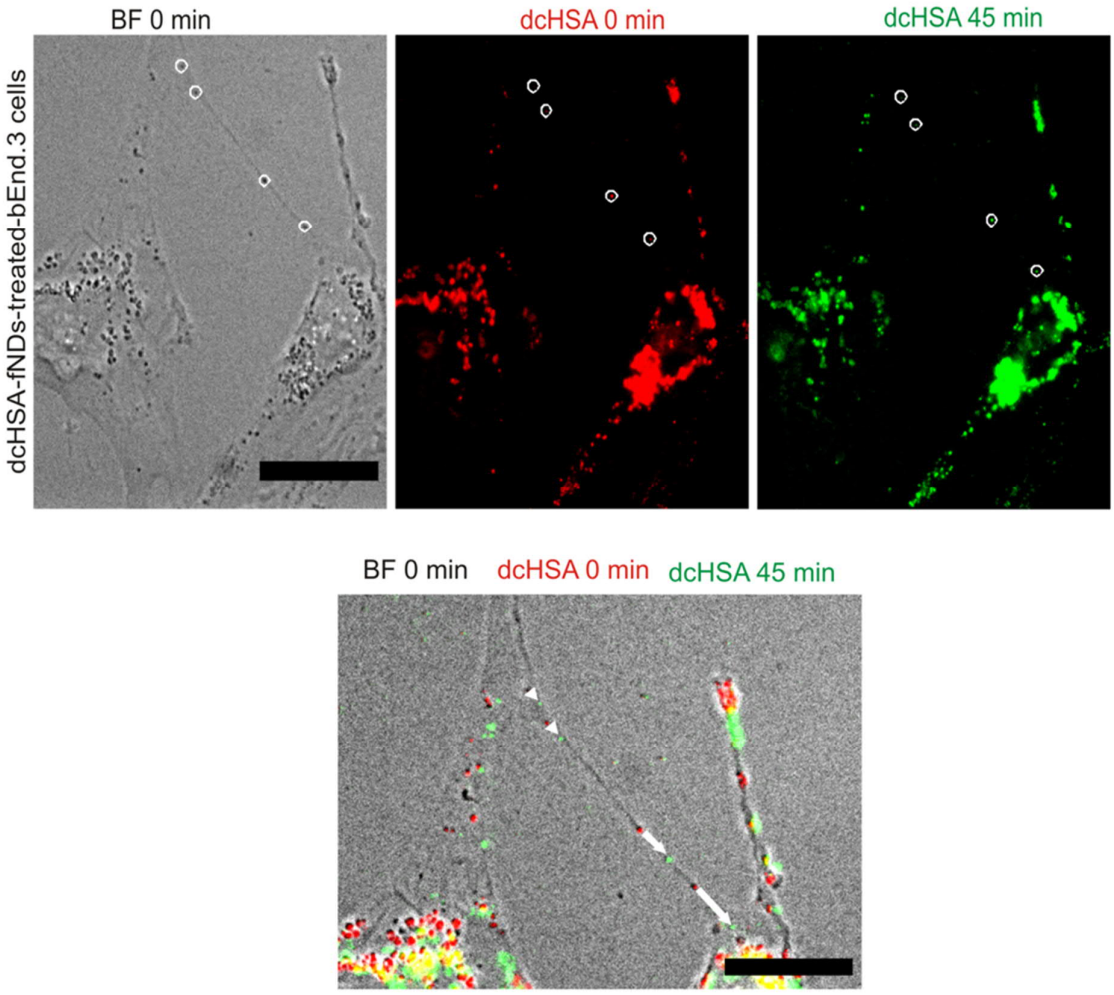

Figure 34. dcHSA-fNDs migration along TNTs in bEnd.3 cells . Time-lapse showing dcHSA-fNDs movements along TNTs in bEnd.3 cells within 45 min via merge of BF picture with fluorescence at time 0 min (red) and time 45 min (green). White circles indicate the dcHSA-fNDs taken into consideration; white arrows indicate length and direction of dcHSA-fNDs migration. Scale bar = 20 µm.

Previously published studies have also demonstrated TNT formation occurring in neurons and astrocytes in mono-culture as well as in co-cultures (Gerdes et al. 2013, Sun et al. 2012, Tardivel et al. 2016). Indeed, live cell imaging and time lapse on co-cultures of immature neurons/glia showed dcHSA-fNDs-vesicles in comparable structures to the ones observed for bEnd.3 cells (Figure 35A). GFAP/ß-III-tubulin/rhodamine-phalloidin costainings revealed also TNTs connecting astrocytes and neurons (Figure 35B). Interestingly, these data strongly support the hypothesis of direct transfer of dcHSA-fNDs observable for all NVU investigated cells.

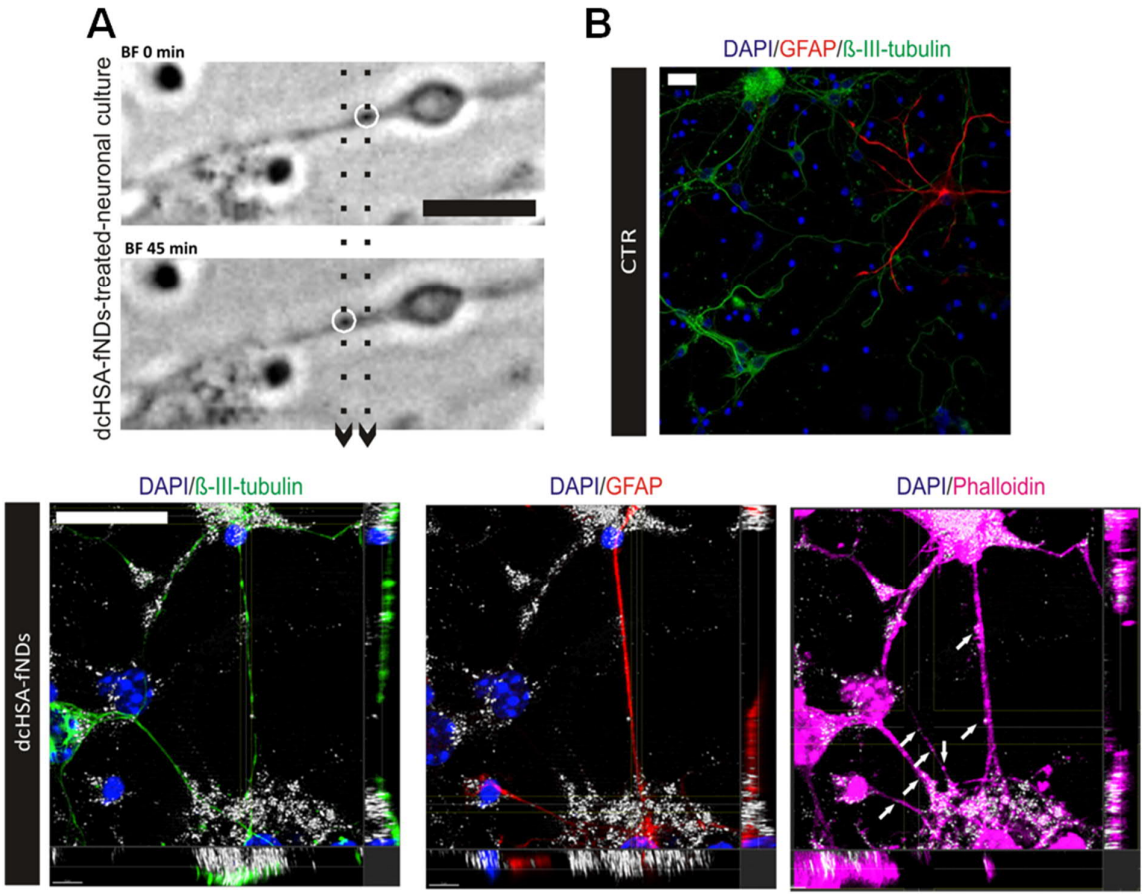

Figure 35. dcHSA-fNDs localization in actin bridges in neurons/glia co-cultures. (A) Representative time lapse of dcHSA-fNDs movement along TNTs in neurons. Dashed lines indicate the edges of dcHSA-fNDs-containg vesicle movement. (B) Representative confocal orthogonal view of dcHSA-fNDs (white) colocalization with TNTs (white arrows) observable via phalloidin staining (magenta) and cellular specific markers: GFAP for astrocytes (red) and ß-III-tubulin for neurons (green). Scale bar = 20 µm

4.2.6 dcHSA-fNDs do not affect cell vitality and BBB integrity in vitro

Effect on bEnd.3 cells monolayer and on astrocytes and neurons viability was carefully investigated. In order to monitor the bEnd.3 cells monolayer integrity, using CellZscope, TEER was constantly measured during the dcHSA-fNDs treatment in transwell inserts. The TEER dropped slightly for both CTR and dcHSA-fNDs-treated inserts while during the whole time of the treatment no difference between CTR and dcHSA-fNDs-treated samples could be observed (n = 6 wells from 3 cultures, two-way ANOVA, $P > 0.05$) (Figure 36A, B). For experiments carried out on mixture 40-60 nm dcHSA-fNDs, for treated cells TEER measurement showed a slight increase in TEER values compared to untreated samples (n = 6 wells from 3 cultures, two-way ANOVA, $P > 0.05$) (Figure 36B). In addition, to assess cell vitality in astrocytes and neurons, Alamar blue assays have been carried out applying rising concentrations (0.5, 10 or 30 µg mL^{-1}) of dcHSA-fNDs or dcHSA. This experimental design was established to be able to investigate the contribution of the HSA-based coating in case of toxicity. Naked-NDs could not be used to assess cell vitality due to the tendency to aggregate. Indeed, as already described in the introduction (1.5.1), the dcHSA is responsible for the NDs colloidal stability. The results showed no significant change in cell vitality of both astrocytes (n > 7 wells from 3 cultures, one-way ANOVA) (Figure 36C) and neurons (n > 7 wells from 3 cultures, one-way ANOVA) (Figure 36D) for all investigated concentrations and treatments. On the contrary, staurosporine positive control treatment resulted in a significant decrease in cell vitality compared to CTR (n > 7 wells from 3 cultures, one-way ANOVA, $P < 0.0001$) (Figure 36C, D). These data suggest that dcHSA-fNDs do not have evident toxic effects on investigated cells.

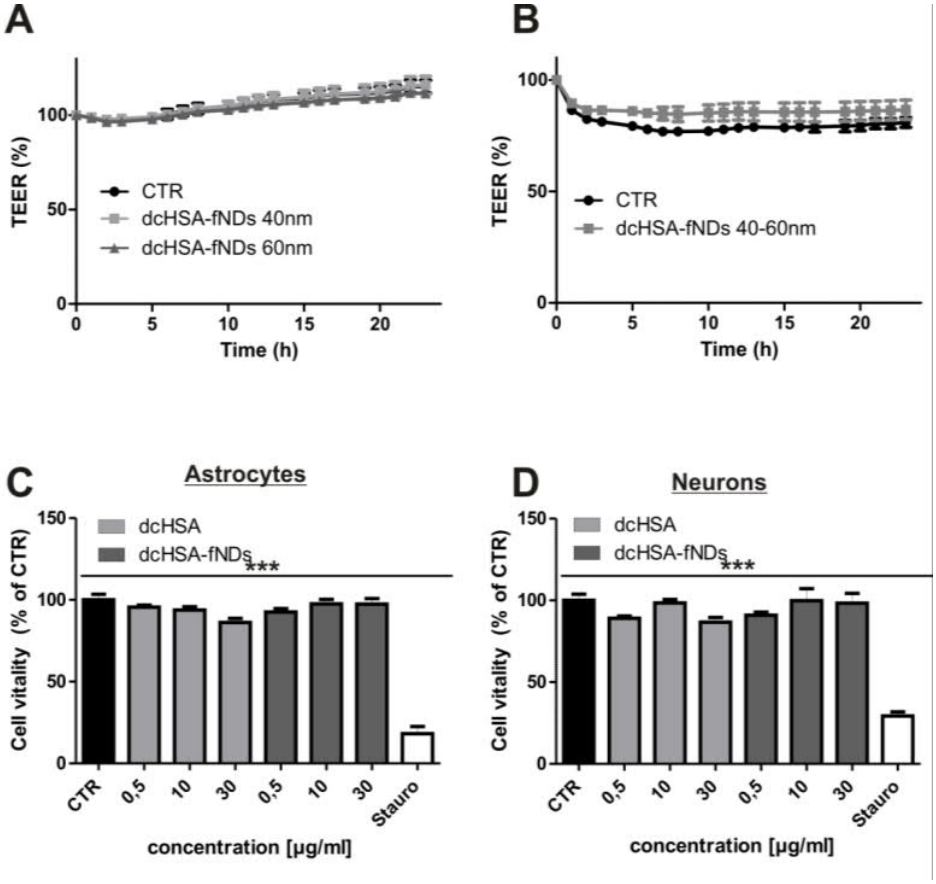

Figure 36. dcHSA-fNDs effect on BBB integrity and cell viability. (A, B) On bEnd.3 cell monolayer BBB in vitro integrity investigated for the duration of the treatment (24 h) with dcHSA-fNDs 40 nm, 60 nm (A) or dcHSA-fNDs mixture 40-60 nm (B). TEER was measured by CellZscope and the values at t = 0 were set to 100 % and each following measurement was expressed in relative percentage; n = 6 wells from 3 cultures. (C, D) Cell vitality after different concentration of dcHSA or dcHSA-fNDs treatment (24 hr) in primary murine astrocytes (C) or in primary murine neurons (D) quantified by Alamar Blue assay. Positive control: cell toxin staurosporine. Astrocytes: n > 7 from 3 cultures; neurons: n > 7 wells from 3 cultures; one-way ANOVA; ***p < 0.001.

4.2.7 dcHSA-fNDs cross the BBB and reach the brain after intravenous injection in mice

The in vitro data highlighted the potential ability of dcHSA-fNDs to cross the BBB. Next, in order to envision a possible clinical application, we investigated whether dcHSA-fNDs were able to reach the brain after tail vein injection in mice. After 24 h

from the application (500 µg mL^{-1} of blood of dcHSA-fNDs), 30 µm slices from brain and liver were screened for dcHSA-fNDs signals. Since previous biodistributional studies have demonstrated that cationic NPs are higly taken up by liver, liver slices were used as positive control for injection efficiency (Blanco, Shen and Ferrari 2015). dcHSA-fNDs signals were clearly visible in liver slices allowing us to additionally compare the different dcHSA-fNDs signals (reflection, bodipy488-labeled-dcHSA-shell, NV) intensity in tissue (Figure 37). The high tissue autofluorescence strongly affected clear detection for fluorescence signals, thus, reflection resulted in the most efficient detection system presenting high signal to noise ratio.

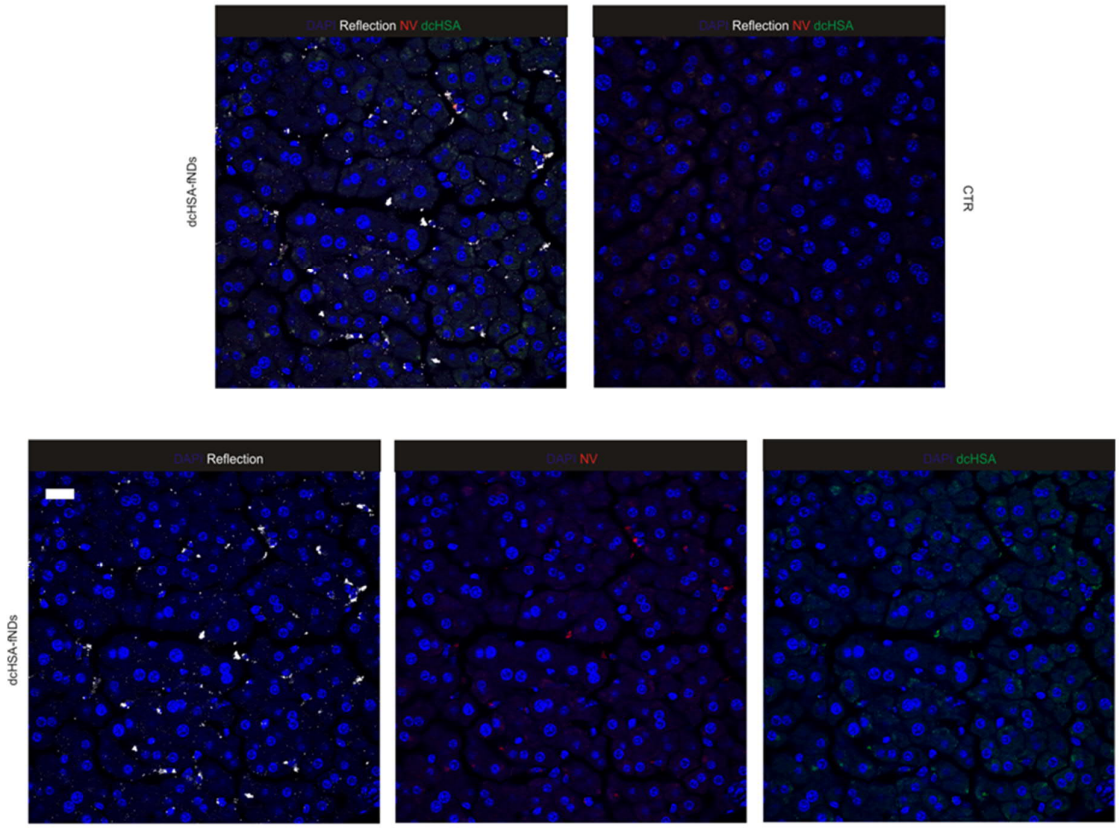

Figure 37. dcHSA-fNDs uptake in liver in vivo. Representative confocal picture of reflection (white), NV (red), dcHSA-shell (green) signals for dcHSA-fNDs in liver; scale bar = 20 µm.

According to this evidence, brain slices were carefully screened for dcHSA-fNDs reflection signals. Orthogonal view of confocal z-stacks showed dcHSA-fNDs in brain slices (Figure 38A). Astrocytes and neuronal cell bodies were stained respectively for GFAP and NeuN, thus it was possible to better characterize the brain uptake and identify the dcHSA-fNDs-positive cells. dcHSA-fNDs were clearly detectable close at the BBB site and some NPs-containing-vesicles colocalized with GFAP-positive-astrocytes surrounding vessels or NeuN-positive neurons as observable from 3D-reconstructions (Figure 38B, C). Thus, these data clearly confirmed the ability of dcHSA-fNDs to cross the BBB and reach the brain parenchyma in vivo.

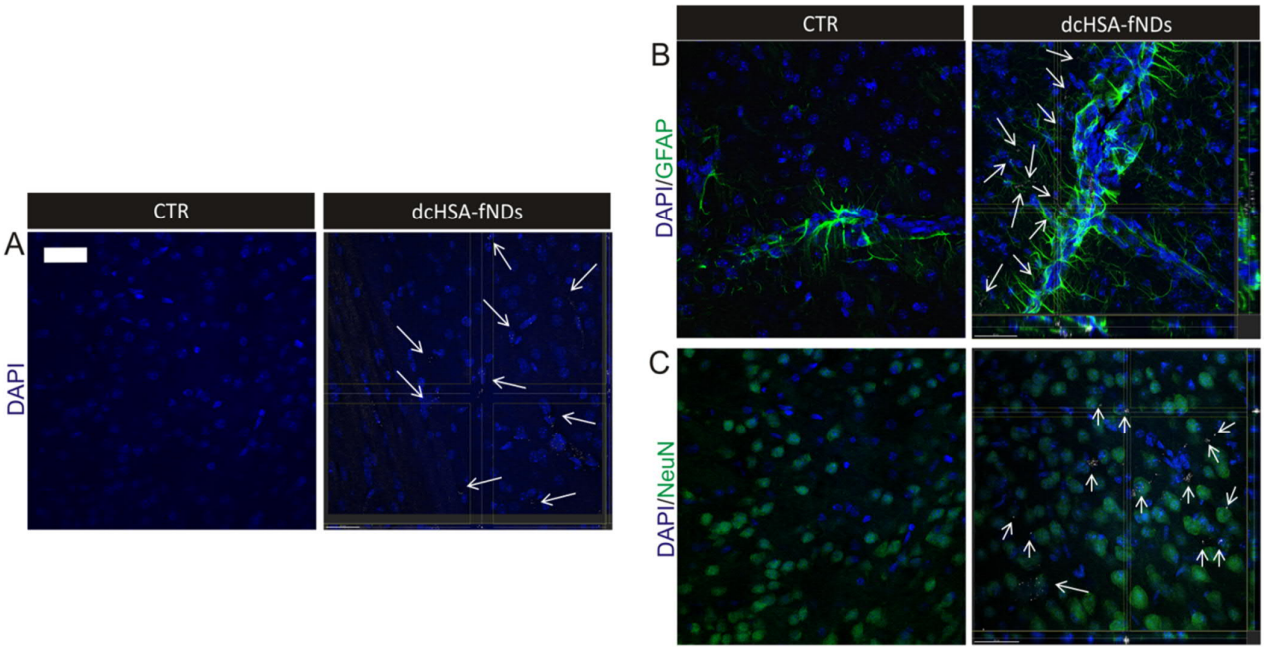

Figure 38. dcHSA- fNDs transport across the BBB and uptake in neurons and astrocytes in vivo. (A) Representative confocal orthogonal views of dcHSA-fNDs (white) signals in brain slices. (B, C) Representative confocal orthogonal view of dcHSA-fNDs (white) localization in GFAP-positive astrocytes (green) (B) and NeuN-positive neurons (green) (C); white arrows indicate area of clear dcHSA-fNDs uptake; scale bar = 40 µm.

5. Discussion

Neurological disorders have high social impact due to severe morbidity and mortality. Although many therapeutic targets and suitable drugs have already been identified and characterized, the BBB, a very tight and unassailable biological barrier, prevents them from reaching the CNS. The current approaches for neurological disease treatments make use of very limited or invasive methods. Therefore, the development of non-invasive, biocompatible and efficient new brain drug delivery systems is eagerly needed.

A high variety of NP-based systems has been investigated to achieve a successful treatment of CNS diseases such as Poly(n-butylcyanoacrylate)-NPs, Methoxypoly(ethylene glycol)-polylactide or Poly(lactide-co-glycolide), liposomes and many inorganic compounds (quantum rods, mesoporous silica NPs) mostly functionalized with BBB-targeting molecules. However, all these nanosystems have shown still limited potential for clinical application mainly due to inefficient pharmacological effects and limited capabilities for drug loading, safety and bioavailability of the encapsulated drug (Grabrucker et al. 2013). According to the need of providing still new strategies for successful clinical implementation of nanomedicine, in this doctoral thesis two different nanosystems have been characterized and studied for brain targeting: dendronized streptavidin (DSA) and dcHSA-fluorescent nanodiamonds (dcHSA-fNDs).

5.1 Dendronized streptavidin represents a promising nanoplatform for brain drug delivery

In the first part of this study a customized, non-invasive hybrid nanocarrier system (DSA) suitable for transporting therapeutic agents into CNS via systemically intravenous administration is presented. DSA are composed by a tetrameric streptavidin core linked to second or third generation PAMAM dendrimers. The nanosystems provided kindly by Dr. David Ng from the laboratory of Prof. Tanja Weil at the Max Planck Institute for polymer research in Mainz, have a size of 5 nm and are positively charged (positive charges: 28 for G2-DSA and 60 for G3-DSA). In a previous study, Ng and colleagues successfully demonstrated that the “bio-click” self-assembly of dendrons and therapeutics on a streptavidin adapter

supplies a supramolecular complex with high stability and simple possibility of functionalization (Ng et al. 2013).

The first question that has been addressed in this thesis is whether DSA are taken up by NVU cells. Initially, the brain endothelial cells as first cell layer DSA have to penetrate in order to reach the brain via crossing the BBB were studied. bEnd.3 cell uptake was observable by fluorocytochemistry as well as via western blot (Figure 9). Combining microscopy and biochemistry data provides a not trivial advantage. Indeed, direct detection of the NP core independent of fluorescent labels excludes false positive data by free fluorescent-dye. Furthermore, a degradation of the detected protein core within 24 h could be excluded. The uptake results point out an important fact. Indeed, the data indicate that differences in the structures and in the amount of positive charges of the dendrimers trigger the ability of DSA to penetrate brain endothelial cells with a more pronounced uptake for G3-DSA than for G2-DSA. It is assumable that the cell uptake is facilitated by the amount of positive charges because of their interaction with the negative charges of the cell membrane as driving force for cell penetration. Additionally, although previous studies demonstrated that PAMAM dendrimers follow a clathrin-mediated endocytosis in HeLa cells (Albertazzi et al. 2010), in contrast to this, co-uptake results show that, the DSA in bEnd.3 cells do not follow only the clathrin-mediated but also and with higher percentage a caveolae-mediated pathway, which is the most common uptake mechanism in endothelial cells (Voigt et al. 2014, Hillaireau and Couvreur 2009, Frank et al. 2003) (Figure 10), indicating that the PAMAM dendrimer hybrids acquire different uptake properties compared to dendrimers alone. DSA uptake was also demonstrated in the other investigated NVU cells: primary murine astrocytes and neurons (Figure 19). Thus, DSA are able to penetrate all the NVU cells showing the ability of potentially crossing the endothelial layer and reaching brain target cells (astrocytes and neurons).

Subsequently, transport was addressed in two different in vitro BBB models: a porcine model composed of a monolayer of primary porcine brain endothelial cells (PBECs) and a murine triple co-culture employing bEnd.3 cells as brain endothelial cell line, primary murine astrocytes and primary murine neurons. The advantage of primary cells is that they keep features cell lines might have lost, like expression of efflux transporters and brain capillary specific enzymes important for the physiological function of the BBB. The porcine model was selected to obtain high transendothelial electrical resistance (TEER) values without the need

of co-culturing with astrocytes. Additionally, porcine genome, physiology and anatomy reflect best the human biology compared to other laboratory animals (Patabendige et al. 2013b, Patabendige et al. 2013a). On the other hand, since astrocytes and neurons are mainly responsible for the specialization of brain endothelial cells, the triple-co-culture system represents the best in vitro approach to model the BBB (Ruck, Bittner and Meuth 2015).

The obtained results showed that in both in vitro BBB systems, high transport efficiency for G2-DSA and G3-DSA from the luminal to the abluminal compartment could be observed (Figure 11). Comparing DSA transport rate (in the range from 16 to 38 %) with previously published in vitro transport rates for other nanosystems highlights strongly the great potential of DSA to efficiently target the brain. However, the comparison has to be carefully addressed due to different used experimental settings (e.g., the species of cells used, mono- and co-cultures models). Indeed, using BBB models with low TEER (higher passive diffusion) we have to expect higher transport rates (Liu et al. 2014) as well as for nanosystems employing specific brain-targeting ligands (Clark and Davis 2015). DSA show in general a percentage of transport higher compared to transport of gold-NP (conjugated to therapeutic agent and brain-targeted peptide), transferrin receptor-targeted immunoliposomes and neutral, anionic, and cationic malto-dextrin 60 nm nanoparticles (transport rates in a range from 0.4 to 14 %) (Fenart et al. 1999, Johnsen et al. 2017, Prades et al. 2012). Thus, the high in vitro transport efficiency for DSA reveals promising brain-targeting properties of the investigated PAMAM dendrimer-bioconjugates.

In triple co-culture a significant higher luminal transported fraction for G2-DSA (Figure 11D) compared to G3-DSA was observable. Interpreting these results, it has to be considered that quantification of NPs in the media did not take into account NPs taken up by NVU cells in the abluminal compartment also involved in the uptake of DSA as clearly shown in the uptake experiments in astrocytes and neurons (Figure 19). Therefore, an underestimation of the real transport rate is expected since the total transport of DSA is constituted by DSA in abluminal medium + DSA taken up from cells seeded at the bottom of the abluminal compartment. The used method measured the DSA fluorescence in the abluminal medium that represent only one component of the total transport. Intriguingly, further determination of estimated DSA fraction incorporated in cells (estimated DSA cellular fraction = DSA initial fluorescence - DSA abluminal fluorescence - DSA luminal fluorescence) (gray bar; Figure 12) revealed that for G3-

DSA in the triple co-culture model a considerably higher fraction of fluorescence than mono-culture vanished from the luminal and abluminal compartments (Figure 12), while for G2-DSA the loss of fluorescence was constant and comparable between the two investigated BBB models (Figure 12). Indirectly, these results strongly suggest that a higher fraction of G3-DSA than G2-DSA is taken up by cells in triple co-culture compared to mono-culture.

To validate the used in vitro transwell systems as suitable model to study the transport, TEER was monitored and as additional parameter, since the tight junctions restrict the paracellular diffusion of hydrophilic tracers (Gaillard and de Boer 2000), the apparent permeability coefficient (Papp) for FITC-dextran 4 KDa was also measured. TEER and Papp measurements assured that the shown efficiency of DSA to cross BBB in vitro is not related to relevant paracellular transport (Figure 11F, G).

Uptake and transport results suggest transcytosis. Therefore, intracellular trafficking was deeper investigated and DSA were found to localize in both early (EE) and late (LE) endosomes with a very pronounced colocalization percentage for EE (Figure 13). Indeed, the initial intracellular trafficking of a vesicle upon internalization begins with EE. For G2-DSA higher EE colocalization than G3-DSA was observed. The short trafficking time in EE for G3-DSA might be responsible for high uptake and transport rates. Additionally, blocking the endosomes-lysosomes fusion, no lysosome-mediated short term degradation of DSA was observed (Figure 16).

These data, combined with the evidence of low localization in late endosomes (Figure 13C), suggest the involvement of a “proton-sponge” mechanism as already proposed in previous studies for PAMAM dendrimers (Wanling and KW 2012), which describes that cationic polymers have pH-buffering properties inducing endosomal disruption. For this reason, PAMAM dendrimers exhibit high transfection efficiency compared to compounds without buffering ability (Zhou et al. 2006, Zhou et al. 2007). This fact offers the additional possibility of using DSA as a promising nanocarrier for nucleic acid and siRNA delivery preventing lysosomal degradation, one of the limiting steps for successful nucleic acid efficiency.

Thus, many DSA were localized in endosomes but still, looking at the percentage of colocalization we were able to identify the 84 % of intracellular compartment for G2-DSA and 48 % for G3-DSA. In order to identify the remaining intracellular compartment sequestering DSA, we studied the colocalization with other intracellular compartments markers (VAMP3 for

recycling endosomes, TfR for transferrin receptor, LC3 for autophagosomes). Colocalization with the other investigated intracellular compartments was not observable despite few DSA-containing vesicles localizing with LC3-positive-autophagosomes (Figure 15). Therefore, autophagosomal localization required some further investigation in order to exclude induction of autophagy as sensor of induced cellular stress (Cherra and Chu 2008, Codogno and Meijer 2005). Combining immunocytochemistry and western blot analysis, no induction of autophagy was observed (Figure 15). Thus, since endothelial cells show a relatively high basal autophagy (Urbanek et al. 2014), the detection of few NPs-containing-autophagosomes suggests that DSA, in particular G3-DSA given the high rate of uptake, might also be incorporated in autophagosomes during basal autophagy. The study of autophagy induction as toxicity parameter relates to another important question to be addressed: are DSA biocompatible?

Therefore, cell vitality and barrier integrity to study the biocompatibility of DSA in vitro were analyzed. DSA did not show any effects on cell vitality of NVU cells up to concentration of 400 µg mL^{-1} (Figure 17A; 20). This finding was extremely important due to the fact that cationic PAMAM dendrimers have been often associated to high cytotoxicity (Jain et al. 2010). For example, Jevprasesphant and colleagues have carried out a meticulous study aiming to correlate dendrimer generation to cell viability. They have found that although G2-PAMAM dendrimers do not affect cell viability also at relatively high concentration, G3-PAMAM induce severe cell viability decrease (Jevprasesphant et al. 2003). On the contrary, the results presented in this thesis revealed that the use of a streptavidin core provides an elegant approach towards synthesis and biocompatibility. Simultaneously, experiments on BBB integrity showed maintenance of TEER stability over treatment time at a concentration of 45 µg mL^{-1} and a slight temporary decrease in TEER at 400 µg mL^{-1} of maximal 27 % (Figure 17B, C). In agreement with previous studies and established therapies, this is a mild transient paracellular opening of BBB without destroying the NVU (Hülper et al. 2013), which does not have to be considered strictly as a deleterious event but even as a system to better deliver molecules to the CNS (Choi et al. 2008).

The in vitro studies showed the potential of DSA to cross the BBB, target neuronal cells and therefore potentially act as delivery system in clinical applications. The in vitro data presented so far demonstrated the importance of the dendrimer shell in promoting uptake and

transport, which is dependent on the dendrimer-generation most likely due to the amount of positive-charges. The in vitro approach enables to evaluate effects and interactions of DSA on each cell type, to investigate cytotoxicity and to look in depth to mechanism of intracellular trafficking. On the other hand, in vivo behaviour of nanocarriers is unpredictable due to the interaction with blood components which might induce changes in the nature of the nanocarriers before reaching their target. Therefore, in vivo studies are essential to prove the suitability of a candidate compound for nanomedicine applications.

Uptake and transport assays in vitro proved that G3-DSA is more promising for further applications since the higher uptake in cells suggests higher efficiency in penetrating endothelial cells, crossing the BBB and more easily reaching target cells. For this reason, we focused the study on G3-DSA to reach CNS after tail intravenous injection in mice.

In vivo experiments performed with G3-DSA showed uptake and transport at the BBBs site predominantly in ventricles and choroid plexus (Figure 21). Three main barrier layers are considered to separate the blood and the CNS: the endothelium of the brain microvessels, the epithelium of the choroid plexus, and the epithelium of the arachnoid mater (Abbott 2014). Therefore, it is not surprising that G3-DSA were more easily detectable in areas surrounding the ventricles as consequence of the high uptake in that specific brain area (Figure 21D). G3-DSA were detectable in investigated NVU cells with higher intensity signals close to brain endothelial cells than in astrocytes and neurons (Figure 22A). Indeed, the CD105 staining for brain endothelial cells showed clearly G3-DSA signal localized on the abluminal side of the blood vessels (Figure 22A). These results indicate an effective migration of nanocarriers from blood to brain which might follow the hypothesis of permeation from endothelial cells to neurons mediated by astrocytes whose endfeet take up DSA by surrounding the endothelium of blood vessels (Figure 39). A comparable mechanism might be responsible for the migration of pure PAMAM dendrimers through the corpus callosum 1-week post intracranial injection described by Srinageshwar and colleagues (Srinageshwar et al. 2017).

Additionally, by quantification of G3-DSA fluorescence in brain lysates, it was possible to determine the % of injected dose (% ID) in the brain with 0.03 ± 0.0 % and an average concentration of 0.44 ± 0.03 µg/g brain after iv injection of 60 mg/kg cy5-G3-DSA. The obtained values of G3-DSA in the brain are in the range of known dendrimer systems (Ke et al. 2009, Nance et al. 2016) showing a 10-fold higher efficiency of transport to the brain in

healthy animals than the values reported for a published PAMAM G4- hydroxyl-terminated dendrimer (Nance et al. 2016). Assessing a critical analysis of these results, the fact that G3-DSA penetrated an intact BBB in healthy animals represents a crucial point. Indeed, most of already published studies usually evaluate transport efficiency for in vivo disease models in neurological disorders, when BBB is highly impaired. An overestimation of the actual crossing ability of the used nanosystem has to be expected due to increased BBB permeability in pathological conditions, if transport is not determined also in healthy animals. For G3-DSA, demonstrating high transport efficiency across BBB in healthy animals, a higher transport rate, if the BBB is affected by the neurological disorders or in brain cancer can be awaited. Additionally, the concentration of G3-DSA reaching the brain falls in a range comparable to the needed brain concentration for therapeutic molecules like nucleic acids. For example, Tyler and colleagues demonstrated a decrease in gene expression of neurotensin receptor using peptide nucleic acids at a brain molecular concentration almost 5-fold lower than G3-DSA (Tyler et al. 1999). Nance et al. found a % ID of 0.003% (healthy animal) for G4-OH PAMAM dendrimer loaded with N-acetylcysteine to efficiently deliver the drug load in the diseased animal with 100-fold greater brain accumulation compared to free drug (Nance et al. 2017).

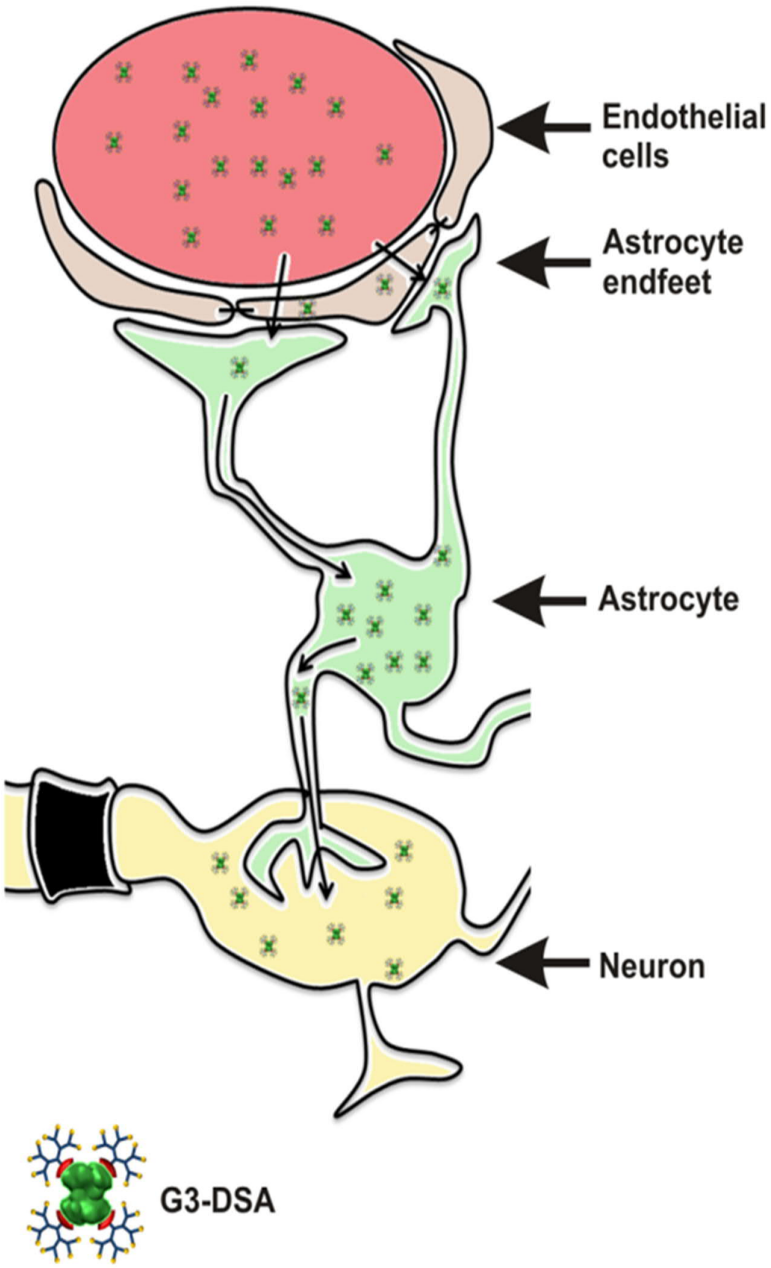

Figure 39. Schematic representation of possible G3-DSA trafficking from the blood to brain target cells in vivo. G3-DSA migrate from bloodstream to brain endothelial cells. Astrocytes endfeet might take up G3-DSA and transfer it to neurons.

Although the target organ of this study is the brain, further experiments were performed to study the biodistribution in several organs in mice. DSA uptake was observable in every investigated organ, but mainly in kidney and liver (Figure 23).

According with previous publications high uptake in kidney is predictable for NPs with a size of 5 nm as in the case of G3-DSA. The other main feature of DSA is to be positive-charged. Positive-charges trigger high uptake in liver (Blanco et al., 2015). Moreover, the data suggest some further considerations. The kidney is involved in two relevant processes: filtration and reabsorption of blood molecules. In the glomerular all molecules of low molecular weight (< 60 KDa) are filtered out of the blood. For instance, most drugs are filtered from blood in the glomerular; however, the overall renal excretion is controlled by what happens in the tubules. More than 90 % of the filtrate is reabsorbed and finally the normal urine output is just a small volume of what it is filtered at the beginning (Julian et al. 2009). The reabsorption is the process that moves solutes and water out of the filtrate and back into the bloodstream and this process could play an important role for DSA bioavailability. On one hand, high kidney uptake of DSA indicates the activation of filtering mechanisms pulling the clearance of the nanocompounds; on the other hand, that might prove the involvement of reabsorpative processes designed to make DSA available again in bloodstream with the possibility to increase the acting life of the nanocompound. WB on blood samples collected after 24 h of G3-DSA treatment revealed a circulation of DSA and, therefore, NPs were still available for uptake (Figure 24). Concurrently, these findings might support the hypothesis that G3-DSA is partly reabsorbed by kidney tubules back into the bloodstream.

The biodistribution data showing high uptake of G3-DSA in off-target organs are due to the fact that the nanosystem presented here has not been designed to selectively target the brain. To improve specific targeting, functionalization with brain-directed molecules (eg.: antibodies, receptor binding proteins) is necessary and possible due to the high flexibility and simple functionalization possibilities of the DSA system.

Finally, the effect of G3-DSA on BBB integrity in vivo was evaluated by an Evans Blue assay. The obtained results did not show increase in BBB permeability for G3-DSA-treated mice compared to sham animals (Figure 25). Thus, a correlation between in vivo G3-DSA uptake and BBB disruption could be excluded proving the biocompatibility of the investigated protein nanocarrier also in vivo.

In summary, combining in vitro and in vivo approaches by using BBB models, NVU cell cultures as well as in vivo experiments on mice, it was demonstrated that DSA (I) are taken up by neurovascular unit cells, (II) are transported from the bloodstream to the brain via transcytosis, (III) are biocompatible for NVU cells, and (IV) do not impair BBB integrity.

The scientific questions addressed in this study defined a promising system to cross the BBB. Thinking to future prospects, a new scientific question strongly emerges: is it possible to efficiently load a drug cargo on DSA reaching the brain after systemic administration still keeping effective the biological function of the loaded molecule?

Answering to this question will require further experiments but previously published studies raise the hope of successful results. Indeed, Ng and colleagues demonstrated that DSA functionalized with tumor suppressor p53 and cytochrome C as cargo increased uptake specificity and impaired cell viability with activation of caspase 3 and 7 in cancer cells (Ng et al. 2013). In this study the loading process of drugs on DSA did not affect the biological activity of potential cargo.

5.2 Fluorescent Nanodiamonds might contribute to the improvement of nanotheranostics approaches for neurological diseases treatments

In the second part of this thesis dcHSA-fNDs as a novel theranostics tool for treatment of neurological diseases via crossing an intact BBB were introduced. NDs have gained a strong interest due to their unique optical and physicochemical properties responsible of their potential intrinsic stable fluorescence, sophisticated surface and biocompatibility which could enable personalized treatment by real time monitoring of drug delivery. Indeed, NDs fall in the category of promising nanotheranostics tool, a combination of diagnosis and therapeutics aiming to the transition from conventional medicine to personalized patient care (Jeelani et al. 2014, Kim et al. 2013). The possibility to monitor the drug reaching a sufficient concentration in the target and a maximum tolerable concentration in off-target organs would give a significant advantage over current techniques, with separated treatment and monitoring. dcHSA-fNDs provided by Weina Liu and Marco Raabe from the lab of Prof. Dr. Tanja Weil at the Max Planck Institute for polymer research in Mainz are composed of NDs encapsulated by a programmable cationized HSA-based biopolymer providing a platform with excellent colloidal stability and reproducible surface functionalization as previously described by Wu and colleagues (Wu et al. 2015).

Aiming to study the potential transport of dcHSA-fNDs across the BBB, at first, the investigated NPs need to penetrate a manolayer of brain endothelial cells.

Indeed, dcHSA-fNDs uptake was observable in bEnd.3 cells (brain endothelial cell lines) (Figure 26). The HSA-based biopolymer is produced by denaturation, cationization and PEGylation of HSA. The presence of positive charges, which enabled the dcHSA-fNDs coating, also provides a favorable condition for cell penetration due to electrostatic interaction with the negative charges of the cell membrane as already described for DSA. Additionally, previous findings have shown the peculiarity of serum albumin to trigger targeted cellular delivery for cancer or rheumatoid arthritis (Wunder et al. 2003) also confirmed for nanosystems employing cationic albumin (Abbasi et al. 2012, Lu et al. 2006) and that could be also a leading process for dcHSA-fNDs uptake. Co-uptake studies aiming to investigate the underlying mechanism of uptake using makers for specific endocytosis pathway demonstrated that the observed uptake occurred via clathrin-mediated and caveolae-mediated endocytosis (Figure 28). Previous findings have stated that often albumin is internalized by cells in general via receptor

mediated endocytosis and specifically also via clathrin-mediated or caveolae-mediated uptake (Schwegler et al. 1991, Yumoto et al. 2006). Therefore, due to the HSA-based coating of dcHSA-fNDs we could expect one of this two mentioned uptake mechanisms. Additionally, quantitative data suggest that dcHSA-fNDs follow a pathway, which starts preferentially with caveolae-mediated uptake (70 %), which is the most common endocytosis in brain endothelial cells (Hillaireau and Couvreur 2009, Frank et al. 2003) and it is also the endocytosis mechanisms observed for albumin in pulmonary endothelial cells (Li et al. 2013, Schubert et al. 2001). dcHSA-fNDs uptake was additionally observed in primary murine astrocytes and neurons suggesting also the possibility of delivery into target neuronal cells after crossing the BBB (Figure 32).

These data suggest that dcHSA-fNDs could underlie a caveolae-mediated transcytosis potentially leading to BBB crossing. Therefore, in vitro BBB transport was evaluated using a monolayer of bEnd.3 cells sedeed on transwell inserts.

The transport data showed the ability of dcHSA-fNDs of different sizes (40 and 60 nm) to be transported from one side to the other of the transwell system. Additionally, the suggested transcytosis was happening in a size-independent manner (Figure 29). One limiting step for nanocarriers to be transported could be the size, which may affect the ability of being transported. Therefore, demonstrating that the size of the nanosystem does not affect the transport rate suggests a higher flexibility in dcHSA-fNDs size and many possibilities of cargo choice applied in drug delivery in future. Indeed, the additional loading of a therapeutic molecule on nanoparticles, more than the physicochemical properties, affect the size with the disadvantage of further modifying the biological “behavior” of the cargo-carrier system.

In order to understand the molecular mechanism leading to the transport, the intracellular trafficking was studied by analysis of the colocalization of dcHSA-fNDs with endosomal markers. 15 % of dcHSA-fNDs have been found in late endosomes after 24 h incubation in bEnd.3 cells while only 2,5 % in early endosomes (Figure 30). This data are in agreement with a previously published study of Wu and colleagues that already demonstrated the LE/lysosomes localization of dcHSA-fNDs in cancer cells. They also demonstrated that cancer cells treated with doxorubicin-loaded-dcHSA-fNDs were showing additionally release of doxorubicin in the cell cytsosol underlying endosome/lysosome escape mechanisms (Wu et al. 2015). However, although part of detectable dcHSA-fNDs localize in LE/lysosomes and their

fate is unpredictable since they might undergo trough several degradation or modifying processes, transport data revealed that partly dcHSA-fNDs are able to avoid entrapment in intracellular compartments and follow a transcytotic pathway responsible of their migration from luminal to abluminal compartment. Concerning the intracellular fate of dcHSA-fNDs another possibility would have been the induction of autophagy with subsequent internalization of dcHSA-fNDs in autophagosomes. dcHSA-fNDs colocalized with a percentage of 0.98 ± 0.52 % with autophagosome that represents a negligible value considering the high rate of basal autophagy in endothelial cells (Urbanek et al. 2014) (Figure 31).

Uptake and intracellular trafficking data revealed additionally a distal localization of dcHSA-fNDs, which enabled the identification of dcHSA-fNDs located in actin bridges connecting two adjacent cells in bEnd.3 (Figure 33) and primary neurons/glia co-culture (Figure 34). The actin bridges have been identified as tunneling nanotubes (TNT), membranous bridges connecting cells over long distances and transferring various cellular components from cell to cell, observed in many cell types in vitro and in developing embryos of different species in vivo (Gerdes et al. 2013). Live cell imaging and time-lapse experiments in brain endothelial cells clearly showed a unidirectional migration from an initiating cell to a target cell and a faster movement while getting closer to the target cell (Figure 33; white arrows) maybe due to the size of the dcHSA-fNDs-containing vesicles determining a slower speed of migration compared to other previously published studies. Indeed, molecules migration along TNTs has been shown to usually fall at least in the speed range of actin-dependent transport (Sun et al. 2012, Gerdes et al. 2013). It seems that dcHSA-fNDs-vesicles need to overcome sort of bottle-neck during the TNTs entry phase assumable from the observed shorter migration of dcHSA-fNDs-vesicles close to the starting edge of the TNT (Figure 33). The data presented here confirm the findings of Epperla and colleagues demonstrating trafficking via TNTs of bovine serum albumin-coated-fNDs in HEK293T and SH-SY5Y cells in vitro (Epperla et al. 2015). These results, in the context of transport across the BBB acquire an emerging interesting value: dcHSA-fNDs might be potentially able to cross the BBB also migrating from one cell to the other without need of being released in the extracellular environment.

The high biocompatibility of NDs among the many carbonaceous nanomaterials has been strongly discussed over time. Although NDs showed no effects on cell viability in many cell

types, toxicity represents a parameter to evaluate very deeply in studies addressing biomedical applications. Indeed, the biocompatibility has to be strictly evaluated according to the specific cell types and the specific complex nanosystem. In this case the dcHSA-coating on fNDs might trigger undesired and unpredictable interactions with components in biological environment leading to possible deleterious effects in particular while working on primary neuronal cells extremely sensitive to changes in their biological environment. Additionally, in the case of brain delivery studies using transwell in vitro model, the BBB integrity represents a parameter to monitor in order to exclude induced BBB disruption.

The biocompatibility data presented in this doctoral work showed that, dcHSa-fNDs do not affect the viability of NVU cells and do not show impairment of BBB in vitro (Figure 36). The observed general decrease of TEER values from time = 0 h until time = 10 h is predictable due to perturbation in the system related to medium exchange. Indeed, the treatment at time = 0 produced a fluctuation-dependent instability in the TEER measurement that recovered within the following hours.

The absence of cytotoxicity or BBB impairment raises the hope of a high biocompatibility. However, further toxicity parameters need to be assessed in vivo. Indeed, clearance mechanism remain still a very crucial aspect to be investigated due to the question whether carbonaceous nanomaterials like fNDs are able to fulfill their proper function and, after, be eliminated of the organism without long-term side effects.

The in vitro studies highlighted the potential of dcHSA-fNDs to cross the BBB. Thus, to assess a possible clinical application, the ability of intravenously injected dcHSA-fNDs to reach the brain via crossing an intact BBB in healthy animals was evaluated. dcHSA-fNDs have been found in brain parenchyma and partly colocalizing with astrocytes and neurons (Figure 38). This data clearly confirmed the ability of dcHSA-fNDs to cross the BBB, reach the brain parenchyma and target different NVU cells in vivo. Combined with the previously discussed in vitro data, it is possible to assume a transcytosis process involving also direct cell-cell migration from brain endothelial cells to neurons via astrocytes incorporation occurring in vivo as in vitro.

In summary, in the second part of this doctoral work, in vitro approaches based on cell culture, transwell assay and confocal microscopy as well as in vivo studies have been used in order to address the question whether dcHSA-fNDs are able to cross the BBB and reach the brain

envisioning possible future neurological personalized treatment. It was demonstrated that dcHSA-fNDs (I) are efficiently transported from one side of a BBB model to the other in a size-independent manner, (II) are delivered to the abluminal side via intracellular trafficking and direct cell-cell interactions mediated by TNTs, (III) are taken up by astrocytes and neurons and (IV) are not toxic for endothelial and neuronal cells and do not impair BBB integrity.

6. Conclusions and future prospects

Nanoparticle research is a fascinating branch of science founded in the observation of unusual, often unexpected effects related to the tiny size of the particles. Indeed, as a matter of fact, one of the most interesting aspects of nanoparticle research is that well-known materials like titania, carbon, gold, diamond (to mention only a few) exhibit surprisingly different properties on the nanoscale. This characteristic led to the development of a broad range of applications involving materials at nanoscale. Nanomaterials started to be explored also in biomedicine brought about an increasing number of findings demonstrating the great potential of nanomedicine in treatment of many diseases. In application for neurological disorders the broad range of nanoparticle properties led to the investigation of their possible use as molecular Trojan horse to cross the BBB, an unassailable biological barrier hindering the delivery of therapeutics to the brain after systemically administration.

This thesis provides evidence that dendrimer protein bioconjugates (DSA) as well as fluorescent nanodiamonds coated with a human serum albumin based biopolymer (dcHSA-fNDs) represent two potential nanosystems able to cross the BBB and move forward the field of neurological disease treatments. Indeed, in this study it was demonstrated that DSA and dcHSA-fNDs 1) are taken up by NVU cells, 2) transported from luminal to abluminal in vitro and in vivo after intravenous injection, 3) do not affect cell viability and BBB integrity.

Looking at DSA, the streptavidin adapter offers a robust scaffold to the simple attachment of biotinylated molecules. This characteristic provides high flexibility due to the simplicity of the biotinylation process. Indeed, the bio-click systems have gained increasing interest since it is ideally possible to imagine a therapy where a vial A with streptavidin adapter could be mixed with a vial B containing any biotinylated drug and PAMAM dendrimers to provide a mixture solution to inject driven by self-assembly mechanism. Like this, potentially any drugs could be easily applied via DSA. The protein nature of dendrimer protein bioconjugates exhibits an additional intrinsic advantage: high biocompatibility due to the fact that protein based NPs hold the ability to interact with biological systems and to be degraded, improving the clearance of the compound.

For neurological disorders treatments, the use of DSA to transport endogenous molecules or growth factors to complement endogenous mechanism for neuronal protection and repair

might be envisioned. The observed high uptake into astrocytes could have potential for treating reactive gliosis occurring in Alzheimer`s disease, multiple sclerosis and glioblastoma by loading DSA with growth factors, such as NGF (nerve growth factor) which has been already shown to be anti-gliosis and neuroprotective (Colangelo et al. 2014). Nonetheless, brain targeted chemotherapeutics may also represent a possible suitable drug cargo for brain tumor. Additionally, DSA could serve as a platform for gene therapy approaches. The lysosomal escape mechanism associated to the cationic nature of DSA points to the possible delivery of nucleic acids, which could compensate gene mutations often related to neurological disorders. In case of prion diseases, a group of fatal neurodegenerative disorders in human and animals (Prusiner 1998), PAMAM dendrimers with high surface density of amino groups have been shown to be effective in inhibiting prion proteins, whose accumulation in CNS is associated to neurological dysfunction (Supattapone et al. 1999, Lim et al. 2010). Thus, the possibility of implementing DSA for treatment of prion diseases could be envisioned. Furthermore, DSA provide the potential to combine anti-prion properties of dendrimers with biotinylated therapeutic molecules in one delivery system.

On the other hand, talking about dcHSA-fNDs, the key feature of fNDs is the intrinsic optical and magnetic nature that suggests a promising potential use for nanotheranostics being able to follow the steps of a therapeutic treatment raising the hope of a personalized therapy from which DSA are still far away. Combining new data obtained on the evaluation of the BBB crossing ability with already published data, the NDs formulation (dcHSA-fNDs) investigated in this work revealed excellent nanotheranostic potential for neurological disorders therapy still presenting a lack of actual therapeutic strategies. NDs have been shown to improve the sensitivity of MRI thanks to their dynamic nuclear spin polarization and the presence of NV centers which might lead to achieve individual care plans for patients, by monitoring target and off-target drug delivery. Additionally, it is possible to envision the use of dcHSA-fNDs for therapy of brain tumors. Indeed, already Matsumura and Maeda in the 1986 demonstrated that an intravenously injected Evans blue-albumin complex accumulated in sarcoma 180 tumors of ddY Mice (Matsumura and Maeda 1986). The retention of albumin in tumors has since then been observed in various experimental solid tumors (e.g., sarcoma, ovarian carcinoma, Novikof hepatoma, etc.) using radiolabeled- or dye-complexed serum albumin (Sinn et al. 1990). Furthermore, fNDs have been demonstrated to achieve phototermal reactivity (Ryu et al. 2016). Combining tumor localization and phototermal properties of fNDs

could be an interesting potential therapeutic approach for selective tumor ablation. Therefore, the dcHSA-fNDs may lead to a charming nanotheranostics approach for brain tumor via crossing BBB and selectively target tumor site due to the human serum albumin coating. Thus, combining the inner properties of fNDs, the possibility of anticancer drug functionalization and the natural albumin-mediated recruitment at the tumor site might be an innovative biomedical strategy.

However, to prove the use of DSA and dcHSA-fNDs for further clinical applications of neurological disorders, beside the investigated ability to cross an intact BBB, further studies have to be carried out to evaluate the efficiency of a drug cargo loaded on the nanocompounds to address its therapeutic functions. Additionally, in both cases to achieve an optimal efficiency, the biodistribution in off-target organs need to be reduced. Thus, to further improve DSA and dcHSA-fNDs, functionalization with BBB specific targeting molecules (eg. lectins, transferrin, angiopep-2, antibodies) represent an essential future prospect. Furthermore, in vivo potential toxicity need to be more carefully addressed by analysis on proinflammatory cytokines distribution, clearance and long term NPs fate.

7. References

Abbasi, E., S. F. Aval, A. Akbarzadeh, M. Milani, H. T. Nasrabadi, S. W. Joo, Y. Hanifehpour, K. Nejati-Koshki & R. Pashaei-Asl (2014) Dendrimers: synthesis, applications, and properties. Nanoscale Research Letters, 9, 247-247.

Abbasi, S., A. Paul, W. Shao & S. Prakash (2012) Cationic albumin nanoparticles for enhanced drug delivery to treat breast cancer: preparation and in vitro assessment. J Drug Deliv, 2012, 686108.

Abbott, N. J. 2014. Anatomy and Physiology of the Blood–Brain Barriers. In Drug Delivery to the Brain: Physiological Concepts, Methodologies and Approaches, eds. M. Hammarlund-Udenaes, E. C. M. de Lange & R. G. Thorne, 3-21. New York, NY: Springer New York.

Ai, Y., W. Markesbery, Z. Zhang, R. Grondin, D. Elseberry, G. A. Gerhardt & D. M. Gash (2003) Intraputamenal infusion of GDNF in aged rhesus monkeys: distribution and dopaminergic effects. J Comp Neurol, 461, 250-61.

Alawdi, S. H., E. S. El-Denshary, M. M. Safar, H. Eidi, M. O. David & M. A. Abdel-Wahhab (2017) Neuroprotective Effect of Nanodiamond in Alzheimer's Disease Rat Model: a Pivotal Role for Modulating NF-κB and STAT3 Signaling. Mol Neurobiol, 54, 1906-1918.

Albertazzi, L., M. Serresi, A. Albanese & F. Beltram (2010) Dendrimer internalization and intracellular trafficking in living cells. Mol Pharm, 7, 680-8.

Amor, S., F. Puentes, D. Baker & P. van der Valk (2010) Inflammation in neurodegenerative diseases. Immunology, 129, 154-69.

Artursson, P. (1990) Epithelial transport of drugs in cell culture. I: A model for studying the passive diffusion of drugs over intestinal absorptive (Caco-2) cells. J Pharm Sci, 79, 476-82.

Balasubramanian, G., I. Y. Chan, R. Kolesov, M. Al-Hmoud, J. Tisler, C. Shin, C. Kim, A. Wojcik, P. R. Hemmer, A. Krueger, T. Hanke, A. Leitenstorfer, R. Bratschitsch, F. Jelezko & J. Wrachtrup (2008) Nanoscale imaging magnetometry with diamond spins under ambient conditions. Nature, 455, 648-51.

Ballabh, P., A. Braun & M. Nedergaard (2004) The blood-brain barrier: an overview: structure, regulation, and clinical implications. Neurobiol Dis, 16, 1-13.

Bamrungsap, S., Z. Zhao, T. Chen, L. Wang, C. Li, T. Fu & W. Tan (2012) Nanotechnology in therapeutics: a focus on nanoparticles as a drug delivery system. Nanomedicine (Lond), 7, 1253-71.

Banks, W. A. (2016) From blood-brain barrier to blood-brain interface: new opportunities for CNS drug delivery. Nat Rev Drug Discov, 15, 275-92.

Beaudoin, G. M., S. H. Lee, D. Singh, Y. Yuan, Y. G. Ng, L. F. Reichardt & J. Arikkath (2012) Culturing pyramidal neurons from the early postnatal mouse hippocampus and cortex. Nat Protoc, 7, 1741-54.

Begley, D. J. & M. W. Brightman (2003) Structural and functional aspects of the blood-brain barrier. Prog Drug Res, 61, 39-78.

Bellavance, M. A., M. Blanchette & D. Fortin (2008) Recent advances in blood-brain barrier disruption as a CNS delivery strategy. AAPS J, 10, 166-77.

Bernacki, J., A. Dobrowolska, K. Nierwińska & A. Małecki (2008) Physiology and pharmacological role of the blood-brain barrier. Pharmacol Rep, 60, 600-22.

Blanco, E., H. Shen & M. Ferrari (2015) Principles of nanoparticle design for overcoming biological barriers to drug delivery. Nat Biotechnol, 33, 941-51.

Braniste, V., M. Al-Asmakh, C. Kowal, F. Anuar, A. Abbaspour, M. Tóth, A. Korecka, N. Bakocevic, L. G. Ng, N. L. Guan, P. Kundu, B. Gulyás, C. Halldin, K. Hultenby, H. Nilsson, H. Hebert, B. T. Volpe, B. Diamond & S. Pettersson (2014) The gut microbiota influences blood-brain barrier permeability in mice. Sci Transl Med, 6, 263ra158.

Burté, F., V. Carelli, P. F. Chinnery & P. Yu-Wai-Man (2015) Disturbed mitochondrial dynamics and neurodegenerative disorders. Nat Rev Neurol, 11, 11-24.

Caraglia, M., G. De Rosa, G. Salzano, D. Santini, M. Lamberti, P. Sperlongano, A. Lombardi, A. Abbruzzese & R. Addeo (2012) Nanotech revolution for the anti-cancer drug delivery through blood-brain barrier. Curr Cancer Drug Targets, 12, 186-96.

Chen, D., C. A. Dougherty, K. Zhu & H. Hong (2015) Theranostic applications of carbon nanomaterials in cancer: Focus on imaging and cargo delivery. J Control Release, 210, 230-45.

Cherra, S. J. & C. T. Chu (2008) Autophagy in neuroprotection and neurodegeneration: A question of balance. Future Neurol, 3, 309-323.

Choi, J. J., S. Wang, T. R. Brown, S. A. Small, K. E. Duff & E. E. Konofagou (2008) Noninvasive and transient blood-brain barrier opening in the hippocampus of Alzheimer's double transgenic mice using focused ultrasound. Ultrason Imaging, 30, 189-200.

Clark, A. J. & M. E. Davis (2015) Increased brain uptake of targeted nanoparticles by adding an acid-cleavable linkage between transferrin and the nanoparticle core. Proc Natl Acad Sci U S A, 112, 12486-91.

Codogno, P. & A. J. Meijer (2005) Autophagy and signaling: their role in cell survival and cell death. Cell Death Differ, 12 Suppl 2, 1509-18.

Colangelo, A. M., L. Alberghina & M. Papa (2014) Astrogliosis as a therapeutic target for neurodegenerative diseases. Neurosci Lett, 565, 59-64.

Cole, J. P., A. M. Hanlon, K. J. Rodriguez & E. B. Berda (2017) Protein-like structure and activity in synthetic polymers. Journal of Polymer Science Part A: Polymer Chemistry, 55, 191-206.

Dai, H., R. S. Navath, B. Balakrishnan, B. R. Guru, M. K. Mishra, R. Romero, R. M. Kannan & S. Kannan (2010) Intrinsic targeting of inflammatory cells in the brain by polyamidoamine dendrimers upon subarachnoid administration. Nanomedicine (Lond), 5, 1317-29.

Daneman, R. & A. Prat (2015) The blood-brain barrier. Cold Spring Harb Perspect Biol, 7, a020412.

Dore-Duffy, P., C. Owen, R. Balabanov, S. Murphy, T. Beaumont & J. A. Rafols (2000) Pericyte migration from the vascular wall in response to traumatic brain injury. Microvasc Res, 60, 55-69.

Duncan, R. (2006) Polymer conjugates for drug targeting. From inspired to inspiration! J Drug Target, 14, 333-5.

Duncan, R., H. Ringsdorf & R. Satchi-Fainaro (2006) Polymer therapeutics--polymers as drugs, drug and protein conjugates and gene delivery systems: past, present and future opportunities. J Drug Target, 14, 337-41.

Elblbesy, M. A. (2016) Hemocompatibility of Albumin Nanoparticles as a Drug Delivery System¡ªAn in Vitro Study. Journal of Biomaterials and Nanobiotechnology, Vol.07No.02, 8.

Engelhardt, S., S. Patkar & O. O. Ogunshola (2014) Cell-specific blood-brain barrier regulation in health and disease: a focus on hypoxia. Br J Pharmacol, 171, 1210-30.

Epperla, C. P., N. Mohan, C. W. Chang, C. C. Chen & H. C. Chang (2015) Nanodiamond-Mediated Intercellular Transport of Proteins through Membrane Tunneling Nanotubes. Small, 11, 6097-105.

Etame, A. B., R. J. Diaz, C. A. Smith, T. G. Mainprize, K. Hynynen & J. T. Rutka (2012) Focused ultrasound disruption of the blood-brain barrier: a new frontier for therapeutic delivery in molecular neurooncology. Neurosurg Focus, 32, E3.

Fakhoury, M. (2015) Role of Immunity and Inflammation in the Pathophysiology of Neurodegenerative Diseases. Neurodegener Dis, 15, 63-9.

Fenart, L., A. Casanova, B. Dehouck, C. Duhem, S. Slupek, R. Cecchelli & D. Betbeder (1999) Evaluation of effect of charge and lipid coating on ability of 60-nm nanoparticles to cross an in vitro model of the blood-brain barrier. J Pharmacol Exp Ther, 291, 1017-22.

Frank, P. G., S. E. Woodman, D. S. Park & M. P. Lisanti (2003) Caveolin, caveolae, and endothelial cell function. Arterioscler Thromb Vasc Biol, 23, 1161-8.

Freese, C., S. Reinhardt, G. Hefner, R. E. Unger, C. J. Kirkpatrick & K. Endres (2014) A novel blood-brain barrier co-culture system for drug targeting of Alzheimer's disease: establishment by using acitretin as a model drug. PLoS One, 9, e91003.

Förstner, P., F. Bayer, N. Kalu, S. Felsen, C. Förtsch, A. Aloufi, D. Y. Ng, T. Weil, E. M. Nestorovich & H. Barth (2014) Cationic PAMAM dendrimers as pore-blocking binary toxin inhibitors. Biomacromolecules, 15, 2461-74.

Gaillard, P. J. & A. G. de Boer (2000) Relationship between permeability status of the blood-brain barrier and in vitro permeability coefficient of a drug. Eur J Pharm Sci, 12, 95-102.

Gamage, N. H., L. Jing, M. J. Worsham & M. M. Ali (2016) Targeted Theranostic Approach for Glioma Using Dendrimer-Based Curcumin Nanoparticle. J Nanomed Nanotechnol, 7.

Geny, B., B. Mettauer, B. Muan, P. Bischoff, E. Epailly, F. Piquard, B. Eisenmann & P. Haberey (1993) Safety and efficacy of a new transpulmonary echo contrast agent in echocardiographic studies in patients. J Am Coll Cardiol, 22, 1193-8.

Gerdes, H. H., A. Rustom & X. Wang (2013) Tunneling nanotubes, an emerging intercellular communication route in development. Mech Dev, 130, 381-7.

Giacomelli, C., S. Daniele & C. Martini (2017) Potential biomarkers and novel pharmacological targets in protein aggregation-related neurodegenerative diseases. Biochem Pharmacol, 131, 1-15.

Goedert, M. (2001) Alpha-synuclein and neurodegenerative diseases. Nat Rev Neurosci, 2, 492-501.

Gothwal, A., P. Kesharwani, U. Gupta, I. Khan, M. C. Iqbal Mohd Amin, S. Banerjee & A. K. Iyer (2015) Dendrimers as an Effective Nanocarrier in Cardiovascular Disease. Curr Pharm Des, 21, 4519-26.

Grabrucker, A., R. Chhabra, D. Belletti, F. Forni, M. Vandelli, B. Ruozi & G. Tosi. 2013. Nanoparticles as Blood–Brain Barrier Permeable CNS Targeted Drug Delivery Systems.

Harris, H. & D. C. Rubinsztein (2011) Control of autophagy as a therapy for neurodegenerative disease. Nat Rev Neurol, 8, 108-17.

Hawkins, B. T. & T. P. Davis (2005) The blood-brain barrier/neurovascular unit in health and disease. Pharmacol Rev, 57, 173-85.

Hillaireau, H. & P. Couvreur (2009) Nanocarriers' entry into the cell: relevance to drug delivery. Cell Mol Life Sci, 66, 2873-96.

Hu, C., D. Hardee & F. Minnear (2007) Membrane fusion by VAMP3 and plasma membrane t-SNAREs. Exp Cell Res, 313, 3198-209.

Huang, R., H. Ma, Y. Guo, S. Liu, Y. Kuang, K. Shao, J. Li, Y. Liu, L. Han, S. Huang, S. An, L. Ye, J. Lou & C. Jiang (2013) Angiopep-conjugated nanoparticles for targeted long-term gene therapy of Parkinson's disease. Pharm Res, 30, 2549-59.

Hülper, P., S. Veszelka, F. R. Walter, H. Wolburg, P. Fallier-Becker, J. Piontek, I. E. Blasig, M. Lakomek, W. Kugler & M. A. Deli (2013) Acute effects of short-chain alkylglycerols on blood-brain barrier properties of cultured brain endothelial cells. Br J Pharmacol, 169, 1561-73.

Ibrahim, N. K., N. Desai, S. Legha, P. Soon-Shiong, R. L. Theriault, E. Rivera, B. Esmaeli, S. E. Ring, A. Bedikian, G. N. Hortobagyi & J. A. Ellerhorst (2002) Phase I and pharmacokinetic study of ABI-007, a Cremophor-free, protein-stabilized, nanoparticle formulation of paclitaxel. Clin Cancer Res, 8, 1038-44.

Jain, A. & K. Cheng (2017) The principles and applications of avidin-based nanoparticles in drug delivery and diagnosis. J Control Release, 245, 27-40.

Jain, K., P. Kesharwani, U. Gupta & N. K. Jain (2010) Dendrimer toxicity: Let's meet the challenge. Int J Pharm, 394, 122-42.

Jeelani, S., R. C. Reddy, T. Maheswaran, G. S. Asokan, A. Dany & B. Anand (2014) Theranostics: A treasured tailor for tomorrow. J Pharm Bioallied Sci, 6, S6-8.

Jevprasesphant, R., J. Penny, R. Jalal, D. Attwood, N. B. McKeown & A. D'Emanuele (2003) The influence of surface modification on the cytotoxicity of PAMAM dendrimers. Int J Pharm, 252, 263-6.

Johnsen, K. B., A. Burkhart, F. Melander, P. J. Kempen, J. B. Vejlebo, P. Siupka, M. S. Nielsen, T. L. Andresen & T. Moos (2017) Targeting transferrin receptors at the blood-brain barrier improves the uptake of immunoliposomes and subsequent cargo transport into the brain parenchyma. Sci Rep, 7, 10396.

Julian, B. A., H. Suzuki, Y. Suzuki, Y. Tomino, G. Spasovski & J. Novak (2009) Sources of Urinary Proteins and their Analysis by Urinary Proteomics for the Detection of Biomarkers of Disease. Proteomics. Clinical applications, 3, 1029-1043.

Kaech, S. & G. Banker (2006) Culturing hippocampal neurons. Nat Protoc, 1, 2406-15.

Kamaly, N., Z. Xiao, P. M. Valencia, A. F. Radovic-Moreno & O. C. Farokhzad (2012) Targeted polymeric therapeutic nanoparticles: design, development and clinical translation. Chem Soc Rev, 41, 2971-3010.

Kamphorst, W., A. G. de Boer & P. J. Gaillard (2002) Brain Drug Targeting: The Future of Brain Drug Development.: Pardridge W M. Cambridge University Press, 2001, £65.00. ISBN 0 521 80077 3. Journal of Clinical Pathology, 55, 158-158.

Karimi, M., S. Bahrami, S. B. Ravari, P. S. Zangabad, H. Mirshekari, M. Bozorgomid, S. Shahreza, M. Sori & M. R. Hamblin (2016) Albumin nanostructures as advanced drug delivery systems. Expert Opin Drug Deliv, 13, 1609-1623.

Ke, W., K. Shao, R. Huang, L. Han, Y. Liu, J. Li, Y. Kuang, L. Ye, J. Lou & C. Jiang (2009) Gene delivery targeted to the brain using an Angiopep-conjugated polyethyleneglycol-modified polyamidoamine dendrimer. Biomaterials, 30, 6976-85.

Khanadeev, V., B. Khlebtsov, G. Packirisamy & N. Khlebtsov. 2017. Bovine serum albumin nanoparticles loaded with Photosens photosensitizer for effective photodynamic therapy. In Saratov Fall Meeting 2016: Fourth International Symposium on Optics and Biophotonics, 7. SPIE.

Kievit, F. M. & M. Zhang (2011) Cancer nanotheranostics: improving imaging and therapy by targeted delivery across biological barriers. Adv Mater, 23, H217-47.

Kim, T. H., S. Lee & X. Chen (2013) Nanotheranostics for personalized medicine. Expert Rev Mol Diagn, 13, 257-69.

Klementieva, O., E. Aso, D. Filippini, N. Benseny-Cases, M. Carmona, S. Juvés, D. Appelhans, J. Cladera & I. Ferrer (2013) Effect of poly(propylene imine) glycodendrimers on β-amyloid aggregation in vitro and in APP/PS1 transgenic mice, as a model of brain amyloid deposition and Alzheimer's disease. Biomacromolecules, 14, 3570-80.

Kozler, P. & J. Pokorný (2003) Altered blood-brain barrier permeability and its effect on the distribution of Evans blue and sodium fluorescein in the rat brain applied by intracarotid injection. Physiol Res, 52, 607-14.

Kwon, E. J., M. Skalak, R. Lo Bu & S. N. Bhatia (2016) Neuron-Targeted Nanoparticle for siRNA Delivery to Traumatic Brain Injuries. ACS Nano, 10, 7926-33.

LaFerla, F. M., K. N. Green & S. Oddo (2007) Intracellular amyloid-beta in Alzheimer's disease. Nat Rev Neurosci, 8, 499-509.

Lagassé, H. A., A. Alexaki, V. L. Simhadri, N. H. Katagiri, W. Jankowski, Z. E. Sauna & C. Kimchi-Sarfaty (2017) Recent advances in (therapeutic protein) drug development. F1000Res, 6, 113.

Lammers, T., F. Kiessling, W. E. Hennink & G. Storm (2010) Nanotheranostics and image-guided drug delivery: current concepts and future directions. Mol Pharm, 7, 1899-912.

Leiro, V., S. Duque Santos, C. D. F. Lopes & A. Paula Pêgo Dendrimers as Powerful Building Blocks in Central Nervous System Disease: Headed for Successful Nanomedicine.

Leiro, V., J. P. Garcia, H. Tomás & A. P. Pêgo (2015) The Present and the Future of Degradable Dendrimers and Derivatives in Theranostics. Bioconjug Chem, 26, 1182-97.

Li, H. H., J. Li, K. J. Wasserloos, C. Wallace, M. G. Sullivan, P. M. Bauer, D. B. Stolz, J. S. Lee, S. C. Watkins, C. M. St Croix, B. R. Pitt & L. M. Zhang (2013) Caveolae-dependent and -independent uptake of albumin in cultured rodent pulmonary endothelial cells. PLoS One, 8, e81903.

Lim, Y. B., C. E. Mays, Y. Kim, W. B. Titlow & C. Ryou (2010) The inhibition of prions through blocking prion conversion by permanently charged branched polyamines of low cytotoxicity. Biomaterials, 31, 2025-33.

Liu, D., B. Lin, W. Shao, Z. Zhu, T. Ji & C. Yang (2014) In vitro and in vivo studies on the transport of PEGylated silica nanoparticles across the blood-brain barrier. ACS Appl Mater Interfaces, 6, 2131-6.

Loos, B., A. du Toit & J. H. Hofmeyr (2014) Defining and measuring autophagosome flux—concept and reality. Autophagy, 10, 2087-96.
Lu, W., Q. Sun, J. Wan, Z. She & X. G. Jiang (2006) Cationic albumin-conjugated pegylated nanoparticles allow gene delivery into brain tumors via intravenous administration. Cancer Res, 66, 11878-87.
Matsumura, Y. & H. Maeda (1986) A new concept for macromolecular therapeutics in cancer chemotherapy: mechanism of tumoritropic accumulation of proteins and the antitumor agent smancs. Cancer Res, 46, 6387-92.
Mauvezin, C. & T. P. Neufeld (2015) Bafilomycin A1 disrupts autophagic flux by inhibiting both V-ATPase-dependent acidification and Ca-P60A/SERCA-dependent autophagosome-lysosome fusion. Autophagy, 11, 1437-8.
McCarthy, J. M., B. Rasines Moreno, D. Filippini, H. Komber, M. Maly, M. Cernescu, B. Brutschy, D. Appelhans & M. S. Rogers (2013) Influence of surface groups on poly(propylene imine) dendrimers antiprion activity. Biomacromolecules, 14, 27-37.
Meairs, S. & A. Alonso (2007) Ultrasound, microbubbles and the blood-brain barrier. Prog Biophys Mol Biol, 93, 354-62.
Mignani, S., M. Bryszewska, M. Zablocka, B. Klajnert-Maculewicz, J. Cladera, D. Shcharbin & J.-P. Majoral (2017) Can dendrimer based nanoparticles fight neurodegenerative diseases? Current situation versus other established approaches. Progress in Polymer Science, 64, 23-51.
Mochalin, V. N., O. Shenderova, D. Ho & Y. Gogotsi (2011) The properties and applications of nanodiamonds. Nat Nanotechnol, 7, 11-23.
Montesano, R., M. S. Pepper, U. Möhle-Steinlein, W. Risau, E. F. Wagner & L. Orci (1990) Increased proteolytic activity is responsible for the aberrant morphogenetic behavior of endothelial cells expressing the middle T oncogene. Cell, 62, 435-45.
Moscariello, P., D. Y. W. Ng, M. Jansen, T. Weil, H. J. Luhmann & J. Hedrich Brain Delivery of Multifunctional Dendrimer Protein Bioconjugates. Advanced Science, 0, 1700897.
Nance, E., S. P. Kambhampati, E. S. Smith, Z. Zhang, F. Zhang, S. Singh, M. V. Johnston, K. Rangaramanujam, M. E. Blue & S. Kannan (2017) Dendrimer-mediated delivery of N-acetyl cysteine to microglia in a mouse model of Rett syndrome. J Neuroinflammation, 14, 252.
Nance, E., F. Zhang, M. K. Mishra, Z. Zhang, S. P. Kambhampati, R. M. Kannan & S. Kannan (2016) Nanoscale effects in dendrimer-mediated targeting of neuroinflammation. Biomaterials, 101, 96-107.
Ng, D. Y., J. Fahrer, Y. Wu, K. Eisele, S. L. Kuan, H. Barth & T. Weil (2013) Efficient delivery of p53 and cytochrome c by supramolecular assembly of a dendritic multi-domain delivery system. Adv Healthc Mater, 2, 1620-9.
Pardridge, W. M. (2005) The blood-brain barrier: bottleneck in brain drug development. NeuroRx, 2, 3-14.
--- (2007) Blood-brain barrier delivery. Drug Discov Today, 12, 54-61.
Patabendige, A., R. A. Skinner & N. J. Abbott (2013a) Establishment of a simplified in vitro porcine blood-brain barrier model with high transendothelial electrical resistance. Brain Res, 1521, 1-15.
Patabendige, A., R. A. Skinner, L. Morgan & N. J. Abbott (2013b) A detailed method for preparation of a functional and flexible blood-brain barrier model using porcine brain endothelial cells. Brain Res, 1521, 16-30.
Peelaerts, W. & V. Baekelandt (2016) α-synuclein folds: the cards are on the table. Nat Struct Mol Biol, 23, 359-60.
Poduri, A., G. D. Evrony, X. Cai & C. A. Walsh (2013) Somatic mutation, genomic variation, and neurological disease. Science, 341, 1237758.
Posadas, I., B. López-Hernández, M. I. Clemente, J. L. Jiménez, P. Ortega, J. de la Mata, R. Gómez, M. A. Muñoz-Fernández & V. Ceña (2009) Highly efficient transfection of rat cortical neurons using carbosilane dendrimers unveils a neuroprotective role for HIF-1alpha in early chemical hypoxia-mediated neurotoxicity. Pharm Res, 26, 1181-91.

Prades, R., S. Guerrero, E. Araya, C. Molina, E. Salas, E. Zurita, J. Selva, G. Egea, C. López-Iglesias, M. Teixidó, M. J. Kogan & E. Giralt (2012) Delivery of gold nanoparticles to the brain by conjugation with a peptide that recognizes the transferrin receptor. Biomaterials, 33, 7194-205.

Prusiner, S. B. (1998) Prions. Proc Natl Acad Sci U S A, 95, 13363-83.

Rai, M. & C. A. dos Santos. 2017. Nanotechnology Applied To Pharmaceutical Technology. Springer International Publishing.

Reiman, E. M. (2016) Alzheimer's disease: Attack on amyloid-β protein. Nature, 537, 36-7.

Rubin, L. L., D. E. Hall, S. Porter, K. Barbu, C. Cannon, H. C. Horner, M. Janatpour, C. W. Liaw, K. Manning & J. Morales (1991) A cell culture model of the blood-brain barrier. J Cell Biol, 115, 1725-35.

Ruck, T., S. Bittner & S. G. Meuth (2015) Blood-brain barrier modeling: challenges and perspectives. Neural Regen Res, 10, 889-91.

Ryu, T. K., S. W. Baek, R. H. Kang & S. W. Choi (2016) Selective Photothermal Tumor Therapy Using Nanodiamond-Based Nanoclusters with Folic Acid. Advanced Functional Materials, 26, 6428-6436.

Schubert, W., P. G. Frank, B. Razani, D. S. Park, C. W. Chow & M. P. Lisanti (2001) Caveolae-deficient endothelial cells show defects in the uptake and transport of albumin in vivo. J Biol Chem, 276, 48619-22.

Schwegler, J. S., B. Heppelmann, S. Mildenberger & S. Silbernagl (1991) Receptor-mediated endocytosis of albumin in cultured opossum kidney cells: a model for proximal tubular protein reabsorption. Pflugers Arch, 418, 383-92.

Sgarbossa, A. (2012) Natural biomolecules and protein aggregation: emerging strategies against amyloidogenesis. Int J Mol Sci, 13, 17121-37.

Simonato, M., J. Bennett, N. M. Boulis, M. G. Castro, D. J. Fink, W. F. Goins, S. J. Gray, P. R. Lowenstein, L. H. Vandenberghe, T. J. Wilson, J. H. Wolfe & J. C. Glorioso (2013) Progress in gene therapy for neurological disorders. Nat Rev Neurol, 9, 277-91.

Singh, R. & J. W. Lillard (2009) Nanoparticle-based targeted drug delivery. Exp Mol Pathol, 86, 215-23.

Sinn, H., H. H. Schrenk, E. A. Friedrich, U. Schilling & W. Maier-Borst (1990) Design of compounds having an enhanced tumour uptake, using serum albumin as a carrier. Part I. Int J Rad Appl Instrum B, 17, 819-27.

Srinageshwar, B., S. Peruzzaro, M. Andrews, K. Johnson, A. Hietpas, B. Clark, C. McGuire, E. Petersen, J. Kippe, A. Stewart, O. Lossia, A. Al-Gharaibeh, A. Antcliff, R. Culver, D. Swanson, G. Dunbar, A. Sharma & J. Rossignol (2017) PAMAM Dendrimers Cross the Blood-Brain Barrier When Administered through the Carotid Artery in C57BL/6J Mice. Int J Mol Sci, 18.

Sun, X., Y. Wang, J. Zhang, J. Tu, X. J. Wang, X. D. Su, L. Wang & Y. Zhang (2012) Tunneling-nanotube direction determination in neurons and astrocytes. Cell Death Dis, 3, e438.

Supattapone, S., H. O. Nguyen, F. E. Cohen, S. B. Prusiner & M. R. Scott (1999) Elimination of prions by branched polyamines and implications for therapeutics. Proc Natl Acad Sci U S A, 96, 14529-34.

Tanida, I., T. Ueno & E. Kominami (2008) LC3 and Autophagy. Methods Mol Biol, 445, 77-88.

Tardivel, M., S. Bégard, L. Bousset, S. Dujardin, A. Coens, R. Melki, L. Buée & M. Colin (2016) Tunneling nanotube (TNT)-mediated neuron-to neuron transfer of pathological Tau protein assemblies. Acta Neuropathol Commun, 4, 117.

Tyler, B. M., K. Jansen, D. J. McCormick, C. L. Douglas, M. Boules, J. A. Stewart, L. Zhao, B. Lacy, B. Cusack, A. Fauq & E. Richelson (1999) Peptide nucleic acids targeted to the neurotensin receptor and administered i.p. cross the blood-brain barrier and specifically reduce gene expression. Proc Natl Acad Sci U S A, 96, 7053-8.

Urayama, A. & W. A. Banks. 2005. Effects of Stress and Nutrition on Blood-Brain Barrier Functions. In Nutrients, Stress, and Medical Disorders, eds. S. Yehuda & D. I. Mostofsky, 83-95. Totowa, NJ: Humana Press.

Urbanek, T., W. Kuczmik, A. Basta-Kaim & B. Gabryel (2014) Rapamycin induces of protective autophagy in vascular endothelial cells exposed to oxygen-glucose deprivation. Brain Res, 1553, 1-11.

Vismara, E., C. Bongio, A. Coletti, R. Edelman, A. Serafini, M. Mauri, R. Simonutti, S. Bertini, E. Urso, Y. G. Assaraf & Y. D. Livney (2017) Albumin and Hyaluronic Acid-Coated Superparamagnetic Iron Oxide Nanoparticles Loaded with Paclitaxel for Biomedical Applications. Molecules, 22.

Voigt, J., J. Christensen & V. P. Shastri (2014) Differential uptake of nanoparticles by endothelial cells through polyelectrolytes with affinity for caveolae. Proc Natl Acad Sci U S A, 111, 2942-7.

Wang, G. & H. Uludag (2008) Recent developments in nanoparticle-based drug delivery and targeting systems with emphasis on protein-based nanoparticles. Expert Opin Drug Deliv, 5, 499-515.

Wanling, L. & L. J. KW. 2012. Endosomal Escape Pathways for Non-Viral Nucleic Acid Delivery Systems. Molecular Regulation of Endocytosis: Dr. Brian Ceresa (Ed.), InTech.

WHO, W. H. O. 2006. Neurological disorders : public health challenges. Geneva: World Health Organization.

Wilhelm, I. & I. A. Krizbai (2014) In vitro models of the blood-brain barrier for the study of drug delivery to the brain. Mol Pharm, 11, 1949-63.

Wu, Y., A. Ermakova, W. Liu, G. Pramanik, T. M. Vu, A. Kurz, L. McGuinness, B. Naydenov, S. Hafner, R. Reuter, J. Wrachtrup, J. Isoya, C. Förtsch, H. Barth, T. Simmet, F. Jelezko & T. Weil (2015) Programmable Biopolymers for Advancing Biomedical Applications of Fluorescent Nanodiamonds. Advanced Functional Materials, 25, 6576-6585.

Wu, Y., F. Jelezko, M. B. Plenio & T. Weil (2016) Diamond Quantum Devices in Biology. Angew Chem Int Ed Engl, 55, 6586-98.

Wunder, A., U. Müller-Ladner, E. H. Stelzer, J. Funk, E. Neumann, G. Stehle, T. Pap, H. Sinn, S. Gay & C. Fiehn (2003) Albumin-based drug delivery as novel therapeutic approach for rheumatoid arthritis. J Immunol, 170, 4793-801.

Yang, Y. P., L. F. Hu, H. F. Zheng, C. J. Mao, W. D. Hu, K. P. Xiong, F. Wang & C. F. Liu (2013) Application and interpretation of current autophagy inhibitors and activators. Acta Pharmacol Sin, 34, 625-35.

Yumoto, R., H. Nishikawa, M. Okamoto, H. Katayama, J. Nagai & M. Takano (2006) Clathrin-mediated endocytosis of FITC-albumin in alveolar type II epithelial cell line RLE-6TN. Am J Physiol Lung Cell Mol Physiol, 290, L946-55.

Zhang, F., J. Trent Magruder, Y. A. Lin, T. C. Crawford, J. C. Grimm, C. M. Sciortino, M. A. Wilson, M. E. Blue, S. Kannan, M. V. Johnston, W. A. Baumgartner & R. M. Kannan (2017) Generation-6 hydroxyl PAMAM dendrimers improve CNS penetration from intravenous administration in a large animal brain injury model. J Control Release, 249, 173-182.

Zhang, J., X. Zhang, G. Liu, D. Chang, X. Liang, X. Zhu, W. Tao & L. Mei (2016) Intracellular Trafficking Network of Protein Nanocapsules: Endocytosis, Exocytosis and Autophagy. Theranostics, 6, 2099-2113.

Zhou, J., J. Wu, N. Hafdi, J. P. Behr, P. Erbacher & L. Peng (2006) PAMAM dendrimers for efficient siRNA delivery and potent gene silencing. Chem Commun (Camb), 2362-4.

Zhou, L., L. Gan, H. Li & X. Yang (2007) Studies on the interactions between DNA and PAMAM with fluorescent probe [Ru(phen)2 dppz]2+. J Pharm Biomed Anal, 43, 330-4.

Zhu, Y., J. Li, W. Li, Y. Zhang, X. Yang, N. Chen, Y. Sun, Y. Zhao, C. Fan & Q. Huang (2012) The biocompatibility of nanodiamonds and their application in drug delivery systems. Theranostics, 2, 302-12.

List of publications

P. Moscariello, D. Y. W. Ng, M. Jansen, T. Weil, H. J. Luhmann, J. Hedrich, Brain delivery of multifunctional dendrimer protein bioconjugates, Adv. Sci. 2018, 1700897, https://doi.org/10.1002/advs.201700897

P. Moscariello, M. Raabe, W. Liu, S. Bernhardt, H. Qi, U. Kaiser, Y. Wu, T. Weil, H. J. Luhmann, J. Hedrich, Unraveling in vivo brain transport of protein-coated fluorescent nanodiamonds, Small 2019, 1902992, https://doi.org/10.1002/smll.201902992

Declarations

I hereby declare that I wrote the dissertation submitted without any unauthorized external assistance and used only sources acknowledged in the work. All textual passages which are appropriated verbatim or paraphrased from published and unpublished texts as well as all information obtained from oral sources are duly indicated and listed in accordance with bibliographical rules. In carrying out this research, I complied with the rules of standard scientific practice as formulated in the statutes of Johannes Gutenberg-University Mainz to insure standard scientific practice.

I further certify that the submitted scientific work has not been submitted to any other German or foreign university or comparable institution for the conferral of an academic degree and that I did not unsuccessfully end another doctoral or equivalent program in the subject area of the current doctorate.